Tracing Jets Across Redshifts:

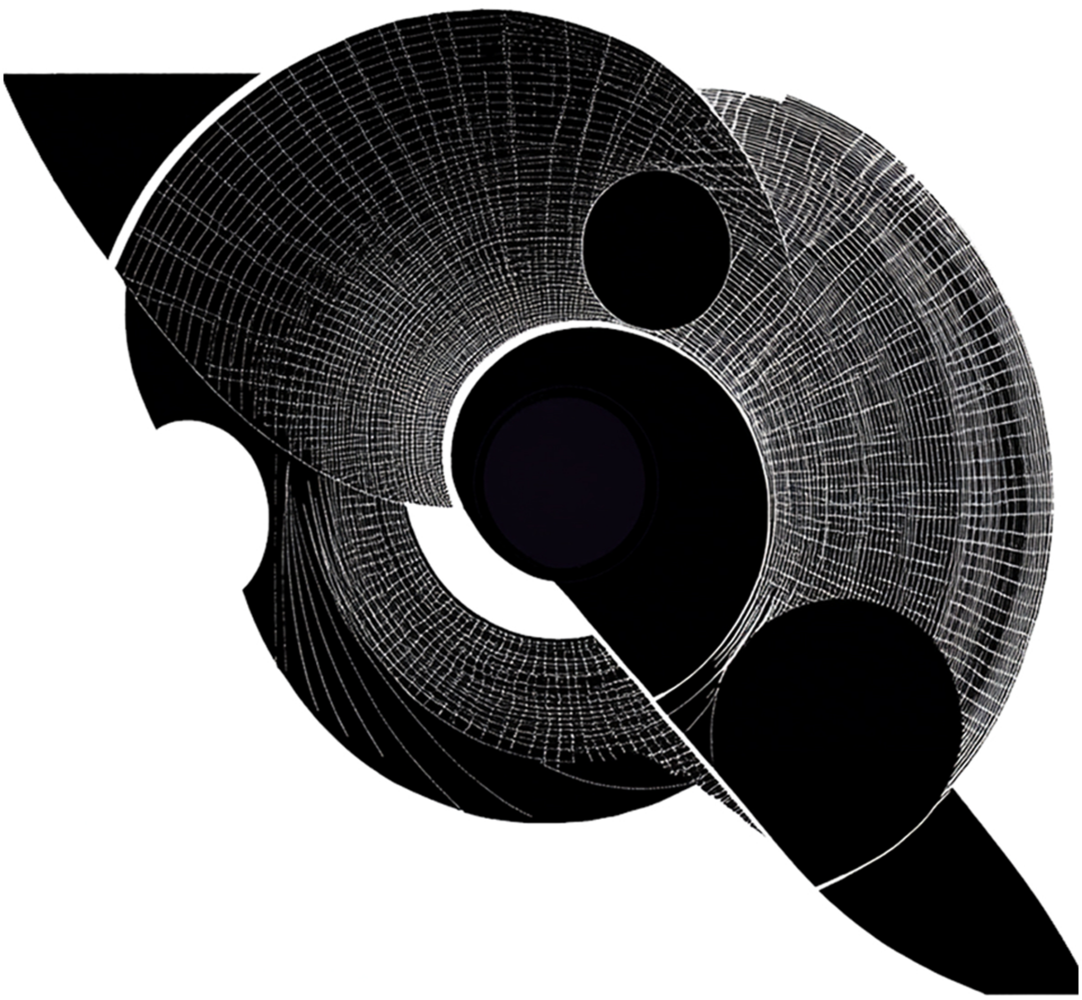

Blazars and the Impact of Jets in High-z Quasars

Zhang-Liang Xie

Dissertation
submitted to the
Combined Faculty of Mathematics, Engineering and Natural Sciences
of Heidelberg University, Germany
or the degree of
Doctor of Natural Sciences

Put forward by:
Zhang-Liang Xie
Born in: Guiyang, China

Tracing Jets Across Redshifts:
Blazars and the Impact of Jets in High-z Quasars

Submitted on: 25 November 2024
Oral examination on: 03 February 2025

Referees:
Priv.-Doz. Dr. Coryn Bailer-Jones
apl. Prof. Dr. Jochen Heidt

Abstract

Blazars, a subclass of radio-loud Active Galactic Nuclei (AGN) with jets aligned close to our line of sight, offer valuable insights into jet physics and demographics of jetted AGN. In this thesis, we present a new algorithm for distinguishing blazars from non-blazars by analyzing their radio morphology with data from the Very Large Array Sky Survey (VLASS). Applying this algorithm to existing catalogs, we reveal that over 12% of previously classified blazar candidates exhibit non-blazar-like morphology. Remarkably, we find that 3% of previously "confirmed" blazars are likely misclassified. A case study of J0643–3314, initially identified as a blazar candidate, was rejected as a blazar by our algorithm,which is supported by observational evidence. This demonstrates the reliability of our morphology-based approach.

Expanding our scope to high-redshift quasars, we present optical and near-infrared spectroscopy of four radio-bright quasars at $z = 5.7 - 7.0$. We estimate black hole mass, bolometric luminosity, and Eddington ratios of these $z > 5.7$ quasars. Although our initial sample is limited in size, these results suggest that high-z radio-loud quasars may not commonly tend to host super-Eddington accreting black holes compared to their high-z radio-quiet or low-z radio-loud quasar counterparts. This hypothesis will be tested further with an expanded sample of 22 additional known $z > 5$ radio-loud quasars. We present preliminary outlooks of their spectra obtained with the Large Binocular Telescope (LBT). These spectra provide us with a larger dataset to determine whether high-z radio-loud quasars are indeed accreting at a faster rate more conclusively.

Zusammenfassung

Blazare, eine Unterklasse der radio-lauten Aktiven Galaktischen Kerne (AGN) mit Jets, die nahe an unsere Sichtlinie ausgerichtet sind, bieten wertvolle Einblicke in die Jet-Physik und die Demografie gejetter AGN. In dieser Dissertation präsentieren wir einen neuen Algorithmus, der Blazare von Nicht-Blazaren anhand ihrer Radiomorphologie unterscheidet, basierend auf Daten des Very Large Array Sky Survey (VLASS). Die Anwendung dieses Algorithmus auf bereits existierende Kataloge zeigt, dass über 12 % der zuvor klassifizierten Blazarkandidaten eine nicht blazar-typische Morphologie aufweisen. Bemerkenswerterweise stellen wir fest, dass etwa 3 % der zuvor bestätigten Blazare wahrscheinlich falsch klassifiziert wurden. Eine Fallstudie zu J0643-3314, der zunächst als Blazarkandidat identifiziert wurde, wurde von unserem Algorithmus als Blazar ausgeschlossen, was durch Beobachtungsdaten gestützt wird. Dies zeigt die Zuverlässigkeit unseres morphologie-basierten Algorithmus.

Im Rahmen einer Erweiterung auf hoch rotverschobene Quasare präsentieren wir optische und nahinfrarote Spektroskopie von vier radio-hellen Quasaren bei $z = 5,7 - 7,0$. Wir schätzen die Massen der Schwarzen Löcher, die bolometrische Leuchtkraft, und die Eddington-Verhältnisse dieser $z > 5,7$-Quasare ab. Obwohl unsere Stichprobe zunächst begrenzt ist, deuten die Ergebnisse darauf hin, dass hoch rotverschobene radio-laute Quasare möglicherweise nicht häufig super-Eddington-akkretiende Schwarze Löcher beherbergen, im Vergleich zu ihren radio-leisen Gegenstücken mit hoher Rotverschiebung oder radio-lauten Quasaren mit niedriger Rotverschiebung. Diese Hypothese wird mit einer erweiterten Stichprobe von 22 weiteren bekannten $z > 5$-radio-lauten Quasaren weiter geprüft. Wir präsentieren vorläufige Ergebnisse der mit dem Large Binocular Telescope (LBT) aufgenommenen Spektren. Diese Spektren liefern uns einen größeren Datensatz, um schlüssiger zu bestimmen, ob hochrotverschobene radio-laute Quasare tatsächlich mit einer höheren Rate akkretiieren.

Acknowledgement

First, I want to thank my advisor, Eduardo Bañados, who has guided me in navigating the challenges of being an astronomer. His feedback has been insightful and consistently on point. I am grateful to Silvia Belladitta, Julien Wolf, Yanu Khusanova, and Laura Martínez, for the rapport in our group and valuable advice. I extend my thanks to Jan-Torge Schindler, who provided immense help with data analysis. I am thankful to Coryn Bailer-Jones and Dominika Wylezalek for serving on my thesis committee and providing great guidance. I thank Christian Fendt and Nina Zhao for their excellent management of the IMPRS program. I am grateful to my colleagues and officemates at MPIA for the exceptional collaboration and the 16th IMPRS generation for the good times we shared. Special thanks to Nils Hoyer for kindly proofreading my Zusammenfassung. I thank Coryn Bailer-Jones and Jochen Heidt for their willingness to evaluate this thesis and Eva Grebel and Matthias Bartelmann for serving as examiners in my defense.

I am grateful to my friends–May, Chuan-ming, Jia-wei, Will, Tom, Wang Zi, Cathy, Mimansa, Angela and Zak, who have made Heidelberg feel like home. To my friends overseas–Yuan-sheng, Gen, Cheng, Hong-xi, Yu-chi, Da-ming, Bo-yu and Flo, our visits have wonderfully punctuated my journey. To my friends in Guiyang, thank you for always taking me on our favorite activities when I return. I want to give special thanks to Zong-rui for designing the cover of this thesis.

I cannot thank my family enough for your unwavering support in everything I do and plan to do, especially my parents, whose love and encouragement have been constant throughout this journey. None of this would have been possible without you. I am happy that I made all my visits home and got to spend time with you. I always look forward to traveling with you, and I am happy to see myself becoming the one to take the wheel, sometimes literally as the driver. Thank you for always being proud of me.

Contents

Acknowledgement **v**

List of Figures **viii**

List of Tables **xi**

1 Background **1**
1.1 Galaxies and supermassive black holes . . . 1
1.2 Jets in AGN . . . 3
1.2.1 Observation of jets . . . 3
1.2.2 The formation and radiation of jets . . . 4
1.2.3 The impact of jets on their host galaxy . . . 5
1.2.4 The impact of jets on black hole growth . . . 5
1.3 A Special Class of Jetted AGNs: Blazars . . . 6
1.3.1 Observational features of blazars . . . 6
1.3.2 Morphological characteristics of blazars . . . 8
1.3.3 The blazar argument: implications for jetted AGN populations . . . 9
1.4 Black Hole Properties of Quasars . . . 9
1.4.1 Black Hole Mass . . . 9
1.4.2 Bolometric Luminosity . . . 10
1.4.3 Accretion Rate . . . 11
1.4.4 Eddington Luminosity . . . 11
1.5 Radio-loud quasars . . . 12
1.5.1 Radio-loudness in quasars . . . 12
1.5.2 Radio-loud fraction in quasars . . . 12
1.5.3 Black hole masses of Radio-loud quasars . . . 13
1.5.4 Radio sky surveys . . . 13
1.6 Quasars in the Early Universe . . . 14
1.6.1 Discovering Quasars in the Early Universe . . . 14
1.6.2 Origins of SMBH . . . 15
1.6.3 Radio-loud Quasars in the Early Universe . . . 17
1.6.4 21cm Forest Study . . . 18
1.7 This thesis . . . 19

I First part **21**

2 Blazar classification algorithm **23**
2.1 Background . . . 23
2.2 Data . . . 24
2.3 Method . . . 24
2.3.1 Automated algorithm of morphology recognition . . . 24
2.3.2 Classifications on morphologies . . . 25

2.3.3 Quality check . . . 28
2.4 Result . . . 29
2.5 Discussion . . . 36
2.5.1 Misidentifications on OFFSET sources . . . 36
2.5.2 Testing the algorithm on the MOJAVE blazars . . . 36

3 Application of the algorithm **39**
3.1 MOJAVE . . . 39
3.1.1 Morphology of MOJAVE Blazars . . . 39
3.2 A testing case . . . 39
3.2.1 Is J0643–3314 (likely) a blazar? . . . 39

II Second part **49**

4 Four radio-detected quasars at z>5.5 **51**
4.1 Background . . . 51
4.2 Data . . . 53
4.2.1 Photometric Data . . . 53
4.2.2 Spectroscopic Observations . . . 53
4.2.3 Fitting of the Spectroscopic Data . . . 55
4.3 Radio . . . 60
4.4 Result . . . 61
4.5 Comparison . . . 62
4.5.1 High-z radio-quiet quasars . . . 63
4.5.2 Low-z radio-quiet/radio-loud quasars . . . 63

III Summary and Outlook **69**

5 Summary & Outlook **71**
5.1 Summary . . . 71
5.2 Outlook . . . 72
5.2.1 Upcoming data . . . 72
5.2.2 Future study . . . 72

Data, Code and Software **77**

List of Figures

1.1 The relationship between dynamically measured black hole (BH) mass and velocity dispersion (σ_*) for galaxies with classical bulges. The letter N stands for NGC in names of galaxies. The solid straight line is the best fit for all data points, indicating the tight $M_{\rm BH} - \sigma_*$ relation. The data is sourced from the collection of Kormendy & Ho 2013. . . . 2

1.2 Artistic representation of the symmetrical lobes of high-energy plasma in milky way, referred to as 'eROSITA Bubbles' or 'Fermi Bubbles' (named after the X-ray and gamma-ray satellites that identify them). These 'bubbles' are believed to have originated from jet activity of the central supermassive black hole (SMBH) several million years ago. Image credits: EarthSky.org & CfA. . . . 3

1.3 An image of the M87 jet at different wavelengths. The top panel features an HST visible light image of M87, showcasing the relativistic jet extending from the bright point-like nucleus, classified as an AGN, located at the upper left. The bottom three panels show the jet in three different wavelengths. From left to right: a *Chandra* X-ray image, a VLA radio image, and an HST visible light image. In all these images, the nucleus is positioned at the lower left. Figure adapted from Maricoba College. . . . 4

1.4 An example of a typical SED of a blazar. It consists of three parts, from the low energy side to the high energy side: Synchrotron emission, Synchrotron-Self Compton (SSC) emission, and External Compton (EC) emission. These parts are distinguishable and form multiple peaks in a typical blazar's SED, where the EC and SSC components often overlap. . . . 7

1.5 Radio images of confirmed blazars from the Very Large Array Sky Survey (VLASS, Lacy et al. 2020; Gordon et al. 2021). These blazars were identified by observing their variability over an extended period by MOJAVE (Monitoring Of Jets in Active galactic nuclei with VLBA Experiments, Lister et al. 2018). The radio structures of these blazars appear either as compact point-like sources or exhibit one-sided extension. This implies that the jets are pointing toward us at a narrow-angle. Due to relativistic effects, the jet directed towards us is visible, while the counter jet, pointing the direction away from us, is not visible in the images. . . . 8

1.6 The black hole mass, bolometric luminosity, and accretion rate for quasars with z$>$ 5.3 are compared to those of low-redshift quasars (z$<$ 2.7). The contour represents low-redshift quasars from the Sloan Digital Sky Survey (SDSS). The physical properties of these low-redshift quasars in SDSS are derived from the SDSS DR16Q data by Wu & Shen 2022. . . 15

1.7 The growth models of early quasars with their potential seed scenarios, and evolutionary tracks characterized by different Eddington ratios λ_{Edd} and jet efficiencies ϵ_j. Jets enables a more efficient accretion phase, permitting scenarios with less massive black hole seeds. . 17

2.1 An illustration of the automated morphological classification algorithm applied to VLASS images (The beam size is denoted in the top left corner, is approximately $1.8'' \times 2.9''$). The algorithm processes each image, converting it into binary values (marked sections are depicted by black contour lines) based on their flux. Each of the 1D curve (blue line) represents the pixel count in a single scanning row in the selected direction, denoted by the white arrows in the image. Cross markers overlayed on the 1D curve indicate peak locations within the 1D curve, which are used to assign morphological classifications to the sources. A green line on the plot represents the peak width measured by each of their relative height. The value in number of pixels is shown, which also contributes to determining the morphological class of the sources (refer to Sec. 2.3.2 for details). 25
2.2 Morphological classification of VLASS images using our automated algorithm. The images are categorized into six distinct morphological classes, grouped into two sets. Blazar-like morphologies include *COMPACT*, *OFFSET*, *1-SIDE EXTENDED*, and *1-SIDE SEPARATED*; while non-blazar-like morphologies comprise *2-SIDE EXTENDED* and *2-SIDE SEPARATED*. In each morphological class, their corresponding 1D signals are shown in two directions, indicated by blue lines. Automatically identified peaks are marked by pink crosses, with morphological classification determined by the properties of peaks, including number, width and distance to the center position. Descriptions of each morphological class and their characteristics can be found in Sec. 2.3.2. 26
2.3 An illustration of two artifact types and a *NON-DETECTION* source in VLASS images. The algorithm identifies cross pattern and dark pixel artifacts, assigning appropriate quality flag values (1 for cross pattern presence, 2 for dark pixel presence, and 3 for both artifacts in the image). Sources with low signal-to-noise ratios that are difficult to discern by visual inspection are classified as *NON-DETECTION* sources. 26
2.4 *OFFSET* sources from Roma-BzCAT, four in total. These sources are classified based on the discrepancy between the catalog position and the position of the radio source. The green cross represents the source position recorded in Roma-BzCAT. The radio image (upper row) demonstrates that the radio-emitting source is not located at the catalog position but has an offset of more than $5''$. In the optical z-band image (lower row), a separate radio-silent source is found at the catalog position. This mismatch is a position error in Roma-BzCAT and we provide the accurate coordinates in our result. 37

3.1 All *2-SIDE SEPARATED* sources with their VLASS2 image in Roma-BzCAT. Each source has undergone visual inspection, and any discrepancies found during this process are indicated by a visual flag in the resulting table. For each of these sources, our revised visual classification is provided. These revised sources are marked with a white star on their image. 40
3.2 Continued for Fig. 3.1. 40
3.3 Same as Fig. 3.1 for *2-SIDE EXTENDED* sources in Roma-BzCAT. 41
3.4 Continued for Fig. 3.3. 42
3.5 Continued for Fig. 3.4. 43
3.6 Continued for Fig. 3.5. 44
3.7 VLASS2 images for 22 MOJAVE blazars classified as likely non-blazars. Each source has undergone visual inspection, and any discrepancies (are *COMPACT* instead of non-*COMPACT*) found during this process are indicated by a visual flag in the resulting table. For each of these sources, our revised visual classification is provided. These revised sources are marked with a white star on their image. 45
3.8 Radio images of sky surveys, from left to right: VLASS 3 GHz, NVSS 1.4 GHz, and TGSS 153 MHz, of the blazar candidate J0643–3314. The VLASS images makes it unlikely to be a blazar (see Xie et al. 2024 for details), since it shows a symmetrical morphological feature. 45
3.9 Radio spectrum of J0643–3314, flux densities collected from radio surveys. The unflat radio spectrum shown here rules out the FSRQ interpretation. 46
3.10 FORS2 1D spectrum of J0643–3314. The red solid line represents the continuum combined with the FeII continuum flux, the blue lines show the emission line models subtracted from the continuum. The presence of broad emission lines confirms that J0643–3314 is not a BL Lac object. 46

4.1 Panoramic spectra of the four quasars in our sample, all fully reduced and processed as described in Section 4.2. For P352–15, the MgII line lies within a strong atmospheric absorption region, thus its black hole properties are derived solely from the CIV line. For three quasars, both CIV and MgII emission lines are detected and used to calculate black hole properties, including black hole mass, bolometric luminosity and Eddington ratio. The detailed measurements of the emission lines and the derived black hole characteristics are summarized in Table 4.4 and Tab. 4.6. 57

4.2 The zoomed-in views of the CIV emission line regions for the four quasars. The black lines represent the spectroscopic data, while the red lines indicate the fitted model, including Gaussian components for the emission lines and the continuum model. The gray lines show the residuals (i.e., the difference between the data and the model). The cyan windows at the top of each panel mark the fitting regions used to construct the line models, and the transparent blue vertical line represents the expected position of the CIV line without any blueshift or redshift. 58

4.3 The same zoomed-in views of the MgII emission line regions for the four quasars in our sample as Fig. 4.2. For P352–15, the MgII line falls within a region of strong atmospheric absorption, making it inaccessible. 59

4.4 VLA 3 GHz radio images of P215–16. North is up, east is left. The beam size ($0.872'' \times 0.522''$) is shown in the bottom left corner. The flux density is extracted on this image to later calculate the radio-loudness. 61

4.5 The same as Fig. 4.4 for J2318-3113. The beam size ($4.676'' \times 1.61''$) is shown in the bottom left corner. 62

4.6 The comparison of radio-loud and radio-quiet quasars at high-z, on the plane of the black hole mass (x axis) and bolometric luminosity (y axis). The accretion rate and Eddington ratio are drawn on the plot as well as dashed lines, note that the leftmost dashed line represents the Eddington limit. The blue points show the 131 high-z quasars, which are all radio-quiet. The top and right panels show the distributions of these 131 quasars, in bins, shown as histograms. The red diamonds are the quasars in our sample. The four red dashed lines show the positions of the quasars in our sample, pinning down their position in the distribution of black hole mass or bolometric luminosity relative to the 131 high-z quasars. The blue contour represents the low-z quasars, which are mostly radio-quiet, as detailed in Sec. 4.5.2. 64

4.7 The comparison between the radio-loud quasars from SDSS DR16Q and the quasars in our sample, on the plane of the black hole mass (x axis) and bolometric luminosity (y axis). The accretion rate and Eddington ratio are drawn on the plot as well as a dashed line, note that the leftmost dashed line represents the Eddington limit. The blue contour represents the radio-quiet quasars in SDSS DR16Q, serving as the representatives of low-z radio-quiet quasars to be matched with the orange contour, the low-z radio-loud quasars. Our quasars in the sample are marked with diamonds, with color bars showing their radio-loudness. Since our quasars are all high-z, they are biased to be bright and massive, making them easier to observe. The comparison of low-z quasars is detailed in Sec. 4.5.2. 66

5.1 The wavelength span of the spectra of our targets (indicated by horizontal lines) on the configurations of the LBT instruments is presented. The two instruments on the LBT, MODS and LUCI, offer distinct wavelength coverage. Within the redshift range of most quasars in our sample, LUCI provides simultaneous coverage of the CIV and MgII emission lines. These spectra enable us to estimate black hole properties using single-epoch black hole mass estimation methods. For objects with an optical spectrum of poor quality, we request MODS observations. 73

5.2 The preliminary spectra of quasars in the upcoming enlarged radio-loud high-z sample, all obtained with the LBT. These spectra will include broad emission lines such as CIV and MgII (if not only CIV, due to contamination or lack of wavelength coverage), allowing for the measurement of black hole properties. This analysis will help determine whether radio-loud high-z quasars are distinctly accreting faster than other quasars. 74

5.3 Same as Fig. 5.2 for 4 more quasars in the upcoming englarged sample. 75

List of Tables

1.1 Sensitivity of detection, sky coverage (percentage of the entire sky), and typical resolution for selected radio surveys. Currently, many radio surveys are updating previous ones with unprecedented coverage and resolution at increasingly higher sensitivity, improving our ability to detect more radio-loud quasars and understand the early universe through radio observations. References: [1]: Shimwell et al. 2022; [2]: Hale et al. 2021; [3]: Gordon et al. 2021; [4]: Condon et al. 1998; [5]: Becker et al. 1995; [6]: Mauch et al. 2003 14

2.1 Sources from the Roma-BzCAT catalog processed and classified using our algorithm. Each source is analyzed based on available radio images from two VLASS epochs, with the algorithm assigning a final morphological classification. Each visually inspected source has a 'VFlag' of 1. If the visual classification ('VClass') does not match the algorithm classification ('Class'), we update 'VClass' to the correct classification. For sources labeled with *VISUAL NEEDED*, their class is determined visually and assigned to 'VClass'. We look into all non-blazar-like sources according to the algorithm in Roma-BzCAT to verify their morphology; more details are in the Appendix. The full table is available online. . . 31

2.2 Same as Tab. 2.1 for WIBRaLS. 32

2.3 Same as Tab. 2.1 for KDEBLLACS. 33

2.4 Statistics of different VLASS morphological classifications for all sources in Roma-BzCAT, WIBRaLS, and KDEBLLACS. We identify four classes as compatible with blazar-like morphologies and two classes as non-blazar morphology. The percentage of non-blazars in WIBRaLS (12%) is higher than in Roma-BzCAT (3%), which is expected given that WIBRaLS consists of candidates, while Roma-BzCAT is a curated catalog. In a test sample of 1000 sources from Roma-BzCAT, the accuracy of the classification is 90.6%. 35

2.5 Same as Tab. 2.1 for MOJAVE sources. 38

4.1 The positions and redshifts of the black holes for each quasar in our sample, along with redshift references, are provided in this table. Additional detailed data used in this work for measuring black hole properties and calculating radio-loudness are presented in Sec. 4.2. References: [1]: Li et al. 2024; [2]: Rojas-Ruiz et al. 2021; [3]: Decarli et al. 2018; [4]:Banados et al. 2024a 53

4.2 The date, instruments, and magnitudes in AB magnitudes for the photometric observations of the four radio-detected quasars in our sample. Photometric measurements are used to calibrate our spectroscopic data, ensuring that the flux density levels are accurately scaled. Details of the spectral data reduction are provided in Sec. 4.2. 55

4.3 The date, instruments, and exposure times (on-source time, no overheads included) for the spectroscopic observations of the four radio-detected quasars in our sample are summarized here. These observations were specifically designed to capture the broad emission lines of CIV and MgII, enabling the analysis of black hole properties. Details of the spectral data reduction are provided in Sec. 4.2. 56

4.4 The emission line profiles presented here are derived from Gaussian models fitted to the spectral data. The CIV line, known for its significant blueshift, is corrected to account for this effect in subsequent analyses. For the MgII line, measurements are conducted using two templates for the underlying iron pseudo-continuum models. The specific fitting procedures and corrections applied and the difference of two iron models are described in details in Sec. 4.2.3. The extracted line properties, including flux, FWHM, and line shifts, serve as inputs for calculating the black hole masses and related properties in Sec. 4.4. . . 60
4.5 Radio flux density measurements of quasars in our sample are presented. All flux measurements are reported as peak flux density values. We derive the radio flux density and luminosity at rest-frame 5 GHz under the assumption that the radio spectrum for each quasar follows a power-law model of $F_\nu \propto \nu^\alpha$. Based on the extrapolated radio flux density at rest-frame 5 GHz and the rest-frame optical (4400Å) and UV (2500Å) continuum flux density, we calculate the radio-loudness R of each quasar. References: [1]: Rojas-Ruiz et al. (2021); [2]: Hale et al. (2021); [3]: Condon et al. (1998); [4]: Momjian et al. (2018); [5]: P215-16: VLA/15A-145; P352-15: [1]; J2318-3113: VLA/16A-202 61
4.6 Black hole properties for each quasar in our sample. These properties are derived from the spectroscopic data reduced through the process described in Sec. 4.2.3, using the emission line profiles extracted from the fitting models. 63
4.7 The KS test of radio-loud quasars to the matched sample of radio-quiet quasars. We control one property and in the matched sample we study if there are any significant differences in the other black hole properties. We conclude that although there are differences in the other black hole properties, the accretion rate is similar between radio-loud and radio-quiet samples. 67

5.1 LBT observations in four semesters. All LBT observations were conducted to collect spectroscopic data for additional radio-loud quasars, aiming to determine their black hole properties through broad emission lines. The quasar sample was selected from known radio-loud quasars, with instruments chosen specifically to capture the broad emission lines (CIV and/or MgII) at the corresponding redshifts. 73

1

Chapter 1

1.1 Galaxies and supermassive black holes

It is now realized that the central supermassive black holes (SMBHs) significantly influence the evolution of their host galaxies. Firstly, there is a tight observational relationship between the mass of central SMBHs and the bulge stellar velocity dispersion in galaxies, the so-called $M_{\mathrm{BH}} - \sigma_*$ relation (see, e.g., Fig. 1.1 and Salviander & Shields 2013; Shen et al. 2015). Secondly, there is a noted correlation between the black hole's mass ratio and the host galaxy's total stellar mass (see, e.g., Magorrian et al. 1998; Häring & Rix 2004). However, understanding this secular process remains challenging as it extends an extended timescale, particularly at the heavy ends of SMBH masses, due to rather transient energy bursts such as rapid AGN accretion and supernova (SN) feedback that can regulate the star formation rate, which further complicates the process Habouzit et al., 2022.

The coevolution of SMBHs and their host galaxies progresses gradually, and the onset and precise mechanisms of this process are still under debate. Recent research on the coevolution of galaxies and AGNs indicates that different components of galaxies may each show unique correlations with AGNs. Graham & Driver (2007) proposed a strong connection between the mass of the SMBH and the galaxy's Sérsic profile, i.e., the variation in brightness with distance from the galactic center. This further complicates our understanding of the coevolution process.

Notably, a significant size difference exists between the accreting central SMBH, referred to as Active Galactic Nucleus (AGN), and its host galaxy. The size of an accreting SMBH is relatively small, with the broad line region (BLR), a clump of fast-moving gas near the SMBH, extending up to 1 parsec, in stark contrast to the bulge of a galaxy, which typically spans kiloparsecs (kpc). Despite the vast difference in physical scales between SMBHs and their host galaxies, their coevolution still holds. It is therefore proposed that these relationships are driven by crucial interactions between the SMBHs and their galaxies. These interactions occur during the active, growing phase of the SMBHs (the AGN phase) and are referred to as AGN feedback.

There are primarily two modes of AGN feedback: the radiative mode, also known as the quasar mode, which originates from radiation pressure emitted by a rapidly accreting AGN. Another is the kinetic mode, generated by powerful jets or outflows from the central AGN that can push the gas out of the galaxy to the megaparsec (Mpc) scales (Fabian, 2012). The evidence for these mechanisms is more direct and visible, as we can track these components directly. Radiation-driven AGN winds can be detected through a high-velocity gas component on a kpc scale (usually exceeding $1000\,\mathrm{km\,s^{-1}}$). Although it is sometimes challenging to distinguish this component from energetic starbursts such as supernovae (SN) feedback, it becomes more certain when the fast gas component appears symmetrically centered around the AGN (see, e.g. Rupke & Veilleux 2011). Furthermore, radio jets from the central AGN are believed to form plasma lobes (see Fig. 1.2), which are clearly visible in X-ray, gamma-ray and microwave images, appearing symmetrically on both sides of the AGN and extending over several kpc (Yang et al., 2022). More observational properties and effects of jets will be discussed in Sec. 1.2.

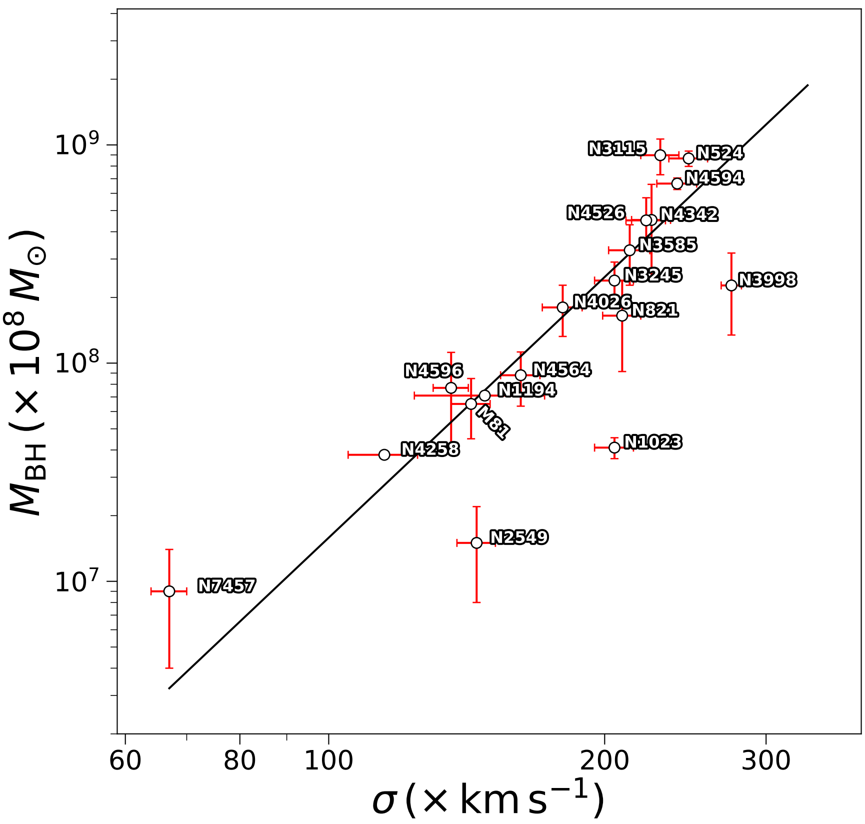

Figure 1.1. The relationship between dynamically measured black hole (BH) mass and velocity dispersion (σ_*) for galaxies with classical bulges. The letter N stands for NGC in names of galaxies. The solid straight line is the best fit for all data points, indicating the tight $M_{\rm BH}-\sigma_*$ relation. The data is sourced from the collection of Kormendy & Ho 2013.

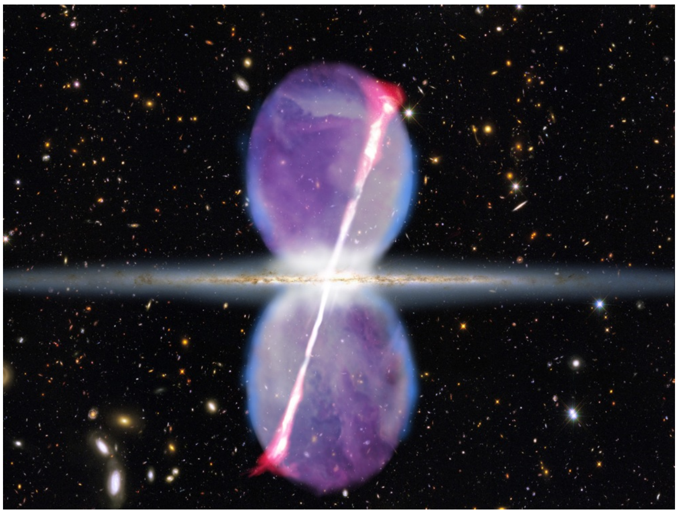

Figure 1.2. Artistic representation of the symmetrical lobes of high-energy plasma in milky way, referred to as 'eROSITA Bubbles' or 'Fermi Bubbles' (named after the X-ray and gamma-ray satellites that identify them). These 'bubbles' are believed to have originated from jet activity of the central supermassive black hole (SMBH) several million years ago. Image credits: EarthSky.org & CfA.

1.2 Jets in AGN

1.2.1 Observation of jets

The detection of the first extragalactic jet by Curtis 1918 in 1918 occurred before the identification of AGNs or any extragalactic objects. Curtis described this jet as "*A curious straight ray … apparently connected with the nucleus by a thin line of matter*" in M87 (also known as NGC4486). Even more than a century ago, this jet was already observable on photographic plates due to its elongated and bright features. Using M87 as a case study, its prominent jet has been resolved into three observational bands: X-ray, visible light, and radio, as shown in Fig. 1.3.

Jets can be observed in radio images on scales spanning from megaparsecs (Mpc) down to sub-parsec (sub-pc) distances (see, e.g., Momjian et al. 2008; Oei et al. 2022; Morabito et al. 2022). Moreover, for M87's jet, the most extensively studied AGN jet, it allows for kinematic analysis down to the gravitational radius, which is at the sub-milliparsec level Kovalev et al., 2007). The Event Horizon Telescope (EHT) further resolved the shadow of M87's supermassive black hole, providing unprecedented insights into the jet-launching region (Event Horizon Telescope Collaboration et al., 2019, 2021).

In particular, the lobes of AGN jets (large-scale, radio-emitting regions formed by the interaction of relativistic jets with the surrounding medium) can have emissions extending to $> 1\,\mathrm{Mpc}$, dependent on the properties of the surrounding circumgalactic medium (Blandford et al., 2019). High-energy observations of AGN jets, particularly in γ and X-rays, complement radio coverage as they probe different parts of AGN jets' Spectral Energy Distribution (SED). The deployment of γ-ray and X-ray satellites and their sky surveys has facilitated more detections of such jets in the high-energy domain. The Fermi satellite (Atwood et al., 2009) reports that jetted AGNs constitute the largest class of sources among their detections Abdollahi et al., 2022a,b. AGNs exhibit robust X-ray continuum emission associated with jets (see e.g., Worrall 2009). Additionally, the multi-epoch monitoring across the radio to γ-ray wavelengths has enabled studies of jetted AGNs with strong variability, particularly those whose jets are

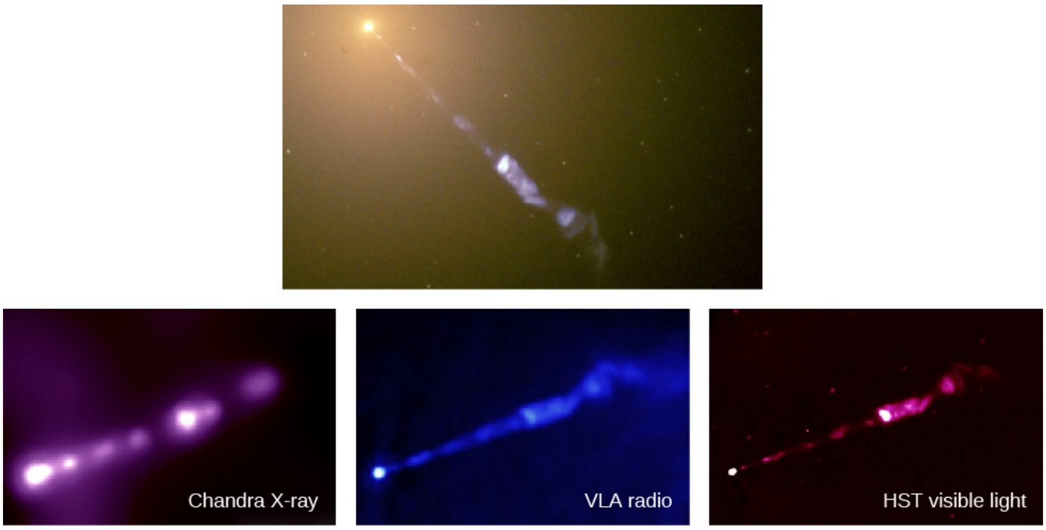

Figure 1.3. An image of the M87 jet at different wavelengths. The top panel features an HST visible light image of M87, showcasing the relativistic jet extending from the bright point-like nucleus, classified as an AGN, located at the upper left. The bottom three panels show the jet in three different wavelengths. From left to right: a *Chandra* X-ray image, a VLA radio image, and an HST visible light image. In all these images, the nucleus is positioned at the lower left. Figure adapted from Maricoba College.

directed at a very small angle relative to our line of sight. More details about this class of jetted AGNs will be discussed in Chapter 1.3.3.

1.2.2 The formation and radiation of jets

The formation of radio jets is closely tied to the accretion of material onto supermassive black holes from magnetized accretion disks. As gas and dust fall toward the black hole, they form an accretion disk, a rotating disk of hot, ionized material. This forms strong magnetic fields that can channel the accreting material into a narrow funnel that is ejected at relativistic speeds. The onset of the strong magnetic field from the SMBH can also be highly modulated by the spin of the black holes (e.g., Wilson & Colbert 1995; Tchekhovskoy et al. 2010). Numerical simulations show that accreting, spinning black holes can generate jets, with the strength of the jet being positively correlated with the spin of the supermassive black hole (e.g. Gammie et al. 2003; McKinney 2006).

Once launched, the principal non-thermal radiation mechanisms in jets are synchrotron radiation and Inverse Compton (IC) scattering. Synchrotron radiation arises when relativistic charged particles, primarily electrons, spiral around magnetic fields near an SMBH. As these particles accelerate along curved trajectories, they emit electromagnetic radiation across a wide range of wavelengths (refer to Chap. 6 in Rybicki & Lightman 1979). This emission is highly polarized, following the magnetic fields along the jets, and typically displays a power law spectrum in frequency. In jetted AGN, the synchrotron component generally dominates the energy spectrum spanning from radio to optical or X-ray frequencies (see, e.g., Attridge et al. 1999; Piner et al. 2010; Pushkarev et al. 2017).

High-resolution radio observations using techniques like Very Long Baseline Interferometry (VLBI) have revealed detailed polarization structures in many jets, which allow astronomers to map out the magnetic field and its interaction with the surrounding gas (see e.g., Park & Algaba 2022), while processes such as Inverse Compton (IC) scattering, where relativistic electrons transfer energy to low-frequency photons, contribute to the higher energy emissions from jets, often resulting in X-ray or gamma-ray radiation. The seed photons for IC scattering can originate from the jet itself or external sources such as photons from accretion disks or the AGN torus, and the cosmic microwave background (CMB). This mechanism is crucial for producing the high-energy X-ray and gamma-ray emissions observed in AGNs (see, e.g., Tavecchio et al. 2000; Potter & Cotter 2012). Further discussion on this will be provided in Sec. 1.3.3.

1.2.3 The impact of jets on their host galaxy

Radio jets can profoundly influence their host galaxies. As these jets traverse the interstellar medium, they can transport energy and momentum to the surrounding gas, causing it to heat up and prevent it from cooling and forming new stars. This phenomenon, referred to as AGN feedback (which also includes other AGN-related activities like winds), can regulate the rate of star formation and shape the overall galaxy morphology (see, e.g., Fabian 2012; Nyland et al. 2018). In some cases, jets can support the formation of stars by compressing gas clouds, which results in starbursts in localized regions of the galaxy (see, e.g., Capetti et al. 2022; Duncan et al. 2023).

On a larger scale, the energy released by the radio jets of AGN can impact the galaxy by expelling and heating the gas around the host galaxy. The circumgalactic medium eventually absorbs this jet energy, causing it to warm up Fabian, 2012. The large bubbles observed at X-ray energies support this effect. After the jet activity ceases and the jets begin to cool, the jet fronts may separate from the jet and form giant bubbles seen in X-ray and γ-ray satellite data (e.g., Yang et al. 2022). Jets also contribute to the most of the intergalactic magnetic field Blandford et al., 2019.

1.2.4 The impact of jets on black hole growth

Jets can also regulate the accretion process of the black hole. The incremental growth of the SMBH over time and its relation to the accretion rate can be represented by the equation:

$$\frac{dM_{BH}}{dt} = (1 - \epsilon_{tot})\dot{M} \tag{1.1}$$

where $\dot{M}$ is the accretion rate of the SMBH, M_{BH} is the mass of the black hole and ϵ_{tot} is the total accretion efficiency of the SMBH, that is made of $\epsilon_{tot} = \epsilon_{rad} + \epsilon_{jet}$, where ϵ_{rad} is the efficiency of converting accretion to radiation and ϵ_{jet} is the efficiency of converting accretion energy to jets.

The bolometric luminosity L_{bol} of the SMBH can be connected to the accretion rate as:

$$L_{bol} = \epsilon_{rad}\dot{M} \tag{1.2}$$

By substituting the $\dot{M}$ in Eq. 1.2 with ϵ_{rad} , the accretion rate in Eq. 1.1 becomes:

$$\frac{dM_{BH}}{dt} = \frac{(1 - \epsilon_{tot})L_{bol}}{\epsilon_{rad}} \tag{1.3}$$

Given a constant luminosity L_{bol} and a total accretion efficiency ϵ_{tot}, the presence of a non-zero jet efficiency ϵ_{jet} reduces the radiation efficiency ϵ_{rad}, thereby aiding in the accelerated growth of the black hole. Additionally, jets can enhance the accretion of SMBH by efficiently transporting angular momentum and increasing the accretion rate (Kuncic & Bicknell, 2004).

Thus, a jetted AGN will accrete more rapidly than its non-jetted counterpart when both have the same luminosity (Kuncic & Bicknell 2004, 2007a,b; Jolley & Kuncic 2008). Observational data also indicate that a jetted AGN exhibits rapid accretion (more observational evidence will be discussed in Sec. 1.4). The presence of jets accelerating black hole growth offers a compelling explanation or at least alleviates the challenges in understanding the rapid formation of SMBH in the early universe (discussed further in Sec. 1.4).

1.3 A Special Class of Jetted AGNs: Blazars

Blazars are a type of AGN whose relativistic jets are oriented at very narrow angles with respect our line of sight ($\theta < 20°$, Kollgaard et al. 1992; Urry & Padovani 1995). These narrow-angle relativistic jets produce intense γ-ray and radio emissions, making blazars among the universe's brightest objects at those wavelengths.

The Lorentz factor Γ measures the relativistic beaming observed in blazars. The Lorentz factor is defined as,

$$\Gamma = \frac{1}{\sqrt{1-\beta^2}} \tag{1.4}$$

where $\beta = \frac{v}{c}$, the jet velocity as a fraction of the speed of light.

When jets are moving at relativistic speed, the emitted radiation is significantly boosted in intensity due to the Doppler effect, leading to the observed brightness of blazars. High Lorentz factors, typically ranging from 10 to over 40, are inferred from observations of apparent jet speeds (see e.g., Hovatta et al. 2009; Savolainen et al. 2010; Saikia et al. 2016).

1.3.1 Observational features of blazars

All observational features that distinguish a blazar from other jetted AGN are attributed to their relativistic jet being directed towards us at a very narrow angle. In spite of being among the rarest sub-classes of AGN, they are the most frequently detected sources in the γ-ray sky (e.g., Hartman et al. 1999; Ajello et al. 2020). Blazars are known for their highly variable and polarized radio emissions. Moreover, they exhibit bright luminosity from radio waves to γ-rays (Blandford & Königl, 1979; Abdo et al., 2010). Observational signs of non-thermal radiation from jets can be found across nearly every range on the electromagnetic spectrum (see Blandford et al. 2019 for a review).

The typical SED exhibits a non-thermal continuum characterized by two peaks. The first peak spans from radio frequencies to ultraviolet/X-rays and displays polarization from synchrotron radiation. The second component ranges from low-energy X-rays to *gamma*-rays. The second peak of blazars SED is shaped by two key processes of IC scattering: Synchrotron-Self Compton (SSC) and External Compton (EC). Both mechanisms involve the photons being up-scattered to higher energy; they are different depending on the source of their photons. In the SSC mechanism, relativistic electrons in the jet itself emit synchrotron radiation, which then serves as seed photons for inverse Compton scattering (Jones et al., 1974; Ginzburg & Syrovatskii, 1969). SSC is crucial for modeling the SED, especially at high energy regimes such as in X-ray and *gamma*-ray (see, e.g., Maraschi et al. 1992; Potter & Cotter 2012). By contrast, the EC mechanism is the scattering of seed photons originating outside the jet, which can come from sources such as the accretion disk, broad-line region, or CMB photons. This process

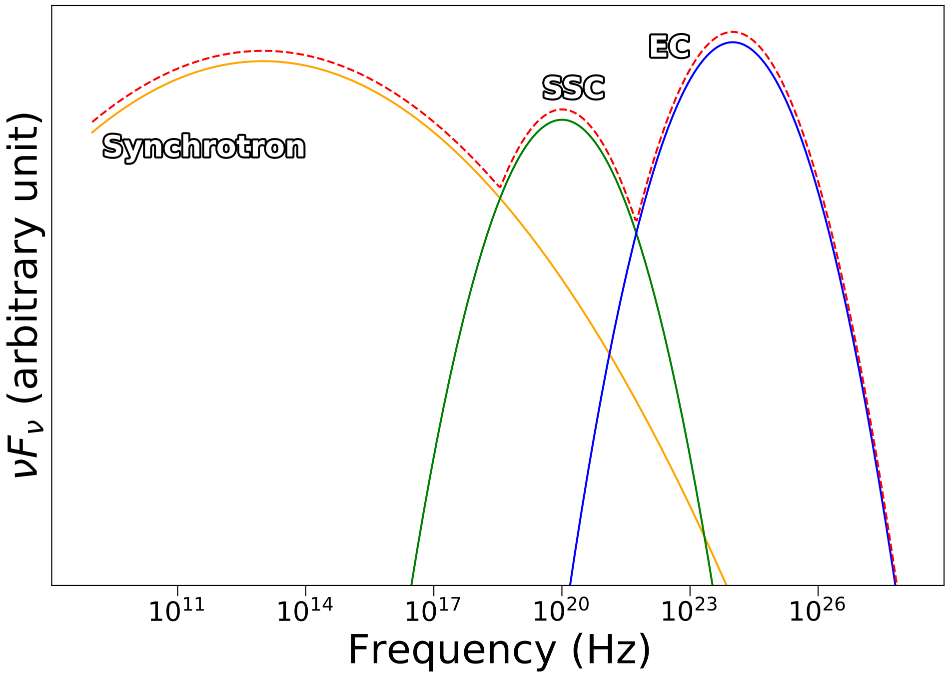

Figure 1.4. An example of a typical SED of a blazar. It consists of three parts, from the low energy side to the high energy side: Synchrotron emission, Synchrotron-Self Compton (SSC) emission, and External Compton (EC) emission. These parts are distinguishable and form multiple peaks in a typical blazar's SED, where the EC and SSC components often overlap.

can significantly enhance high-energy emissions, leading to a broader range of energy output than SSC (see e.g., Sikora et al. 1994). The contributions of SSC and EC vary among different blazar types and different environments, and both are likely at play simultaneously in most blazars, as neither alone suffices to explain the observed SED in certain sources (Arsioli & Chang, 2018).

The jet of the blazars often leaves distinct signatures on the rest-frame optical or infrared spectroscopy. In particular, Blazars can be classified into two sub-classes based on their optical/near-infrared emission lines: BL Lacertae objects (BL Lac), which have either no or very weak emission lines (with rest-frame equivalent width < 5Å; Stickel et al. 1991), and flat spectrum radio quasars (FSRQ), which have broad optical/near-infrared emission lines similar to those of Type-1 quasars and a flat radio spectrum (Sambruna et al., 1996).

Blazars can also be identified through their strong variability in, e.g., γ-ray and radio range, in which the jets emit very variable fluxes given their small angle, ranging from minutes to years (see, e.g., Mattox et al. 1997; Abdo et al. 2015; Raiteri et al. 2021; Banados et al. 2024b). The variability in brightness in blazars not only confirms the presence of blazars but also provides critical insights into the physical conditions of their jets. For instance, the blazar S5 0716+714 has been extensively studied for its short-term variability, with observations revealing significant flux changes in monitoring cadence as brief as minutes. This rapid variability suggests the presence of energetic processes within a rotating, helical jet, whose pitch angle changes over time (Raiteri et al., 2021). Such findings highlight the dynamic nature of blazar jets and the importance of multi-wavelength observations in understanding the mechanisms

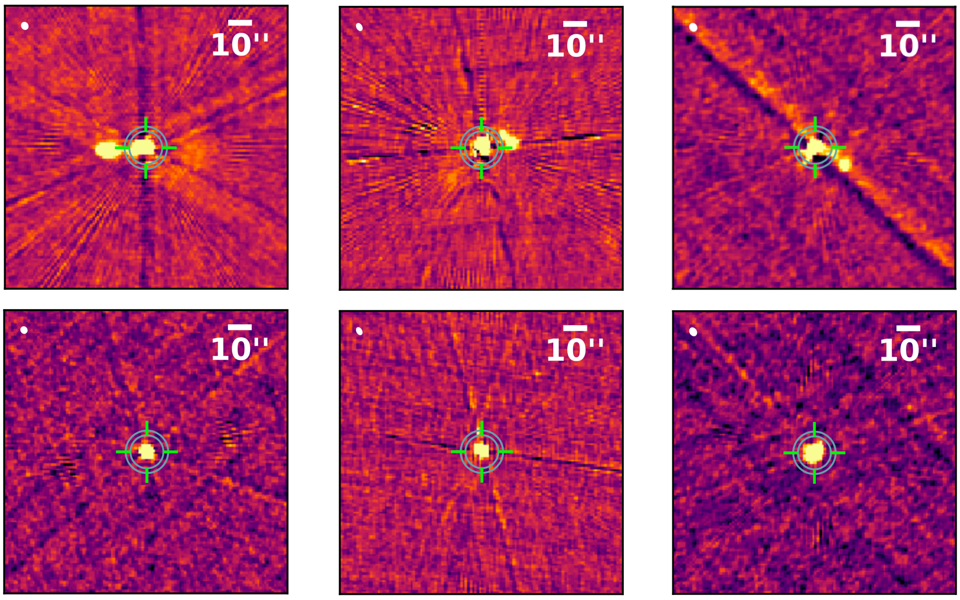

Figure 1.5. Radio images of confirmed blazars from the Very Large Array Sky Survey (VLASS, Lacy et al. 2020; Gordon et al. 2021). These blazars were identified by observing their variability over an extended period by MOJAVE (Monitoring Of Jets in Active galactic nuclei with VLBA Experiments, Lister et al. 2018). The radio structures of these blazars appear either as compact point-like sources or exhibit one-sided extension. This implies that the jets are pointing toward us at a narrow-angle. Due to relativistic effects, the jet directed towards us is visible, while the counter jet, pointing the direction away from us, is not visible in the images.

driving these variations.

Blazar candidates can also be identified through color selection techniques using mid-infrared data. The Wide-field Infrared Survey Explorer (WISE, Wright et al. 2010) has proven particularly useful for this purpose. Researchers have developed diagnostic tools based on WISE color-color diagrams to select blazar candidates. The WIBRaLS (WISE Blazar-like Radio-Loud Sources, D'Abrusco et al. 2014, 2019) catalog, for instance, uses this method to identify blazar candidates with WISE colors similar to confirmed gamma-ray emitting blazars. This approach has successfully identified new blazar candidates, with follow-up spectroscopic observations confirming these candidates as genuine blazars.

1.3.2 Morphological characteristics of blazars

Due to the jets of blazars being pointed at us at a very small angle, blazars are expected to exhibit a very compact morphology. This can be directly observed in radio images. At sub-arcsecond scales, blazars appear either point-like or with a single jet near their center (see Fig. 1.5 for an example of both cases). Observations indicate that this compact or one-sided radio image shows the optically thick radio core with the emitted jet, which can overlap with the core (Wilkinson et al., 1977; Blandford et al., 2019).

The morphological characteristics of a blazar provide a clear indication of the angle at which its jets are oriented, making it a key criterion for identifying whether a source is a blazar or not. Specifically, when the radio image of a jetted AGN presents two jets on either side of the blazar, rather than a compact or one-sided jet configuration, it is evident that this jetted AGN is not a blazar. This is because the counter jet of a blazar (the jet moving away from our line of sight) is moving away at relativistic speeds and is thus often invisible in radio images. This method is applied in the first part of this thesis to rule out non-blazar in blazar candidates selected by color-color technique, detailed in Chap. 2.

1.3.3 The blazar argument: implications for jetted AGN populations

Assuming that the orientation of jets in AGNs is random and uniformly distributed in all directions, the probability of observing a blazar is relatively low. If we further assume that jetted quasars in a given group of similar quasars (e.g., by SMBH masses and redshifts) are distributed sparsely across the universe, with their jets pointing randomly, then the occurrence of a blazar is a rare and lucky event related to our specific viewing angle. This relationship can be quantified using the formula for the total jetted population derived from the observed blazar population as,

$$N_{\text{jetted}} = \frac{1}{1-\cos(\frac{1}{\Gamma})} N_{\text{blazar};\,\theta\leq\frac{1}{\Gamma}}$$

where Γ is the bulk Lorentz factor of the pasma in relativistic jet (Banados et al., 2024b).

Given this premise, when we detect a blazar, we can infer that there are likely many more jetted quasars with their jets directed in other directions throughout the universe. This principle, often summarized as “find one, expect many,” underscores the significance of discovering blazars. This argument becomes particularly significant when applied to the high-redshift universe. Quasars identified in the early universe are rare, so discovering a blazar at high redshift implies that there are likely numerous other jetted quasars at that redshift, but whose jets are not aligned with our line of sight. For example, Banados et al. 2024b identified the most distant blazar known to date at a redshift close to 7. At such high redshifts, only a few quasars have been discovered. However, according to the blazar argument, tens to hundreds more jetted AGNs should be at similar redshifts, with their jets pointed in other directions.

1.4 Black Hole Properties of Quasars

This section will present the black hole properties relevant to the subsequent analysis in this thesis. I will discuss the techniques for measuring these properties, their importance, and the related biases, uncertainties, and limitations. I begin by examining several fundamental concepts and measurements. These concepts include the black hole mass, luminosity, and accretion rate–essential parameters that we estimate in early quasars.

1.4.1 Black Hole Mass

The mass of black holes in quasars can be estimated through the technique of reverberation mapping (RM, Peterson 2014), which studies the response of broad emission lines from the Broad Line Region (BLR). The BLR consists of gas rapidly orbiting the black hole (at a typical velocity of $\sim$5000 km/s for a $10^8 M_\odot$ SMBH). By measuring the time delay between variations in the continuum emission and the emission lines, the distance between the black hole and the BLR can be calculated (Kaspi et al., 2000, 2007). Subsequently, the black hole mass M_{BH} can be determined by combining this distance with the velocity dispersion of the gas, inferred from the emission line widths. Utilizing the virial theorem, which connects kinetic energy to gravitational potential energy in a stable system, the black hole mass is proportional to:

$$M_{BH} \propto R_{BLR} \Delta v^2 \tag{1.5}$$

Here, R_{BLR} represents the distance from the BLR to the central black hole, and Δv is the velocity dispersion of the gas, typically inferred from the Doppler-broadened emission lines.

RM requires continuous monitoring of an AGN's brightness over months or years to detect variability in the broad emission lines. This process is challenging due to the faintness of such a small region in AGNs and the necessity for sustained observations across usually multiple telescopes to capture the necessary data accurately (see e.g., Kaspi et al. 2000).

The single-epoch virial mass estimation technique is derived from the results of RM campaigns and relies on calibrations against these studies to estimate black hole masses from a single spectrum. In this method, the Doppler width of an emission line serves as a substitute for Δv in Eq. 1.5 (Peterson et al., 2004). The BLR size, R_{BLR}, is deduced from the well-established empirical relationship from RM between AGN luminosity and BLR size (Kaspi et al., 2000, 2007). This technique has yielded promising results, particularly with data from the Sloan Digital Sky Survey (SDSS), which produces hundreds of thousands of single-epoch spectra (Shen et al., 2011; Wu & Shen, 2022). However, it carries an intrinsic uncertainty of roughly 0.4 dex (1-2.5 times) compared to RM methods (Shen et al., 2011). The choice of parameters, such as FWHM versus velocity dispersion Δv, can introduce biases. While both are relatively straightforward to measure, FWHM is less sensitive to the line wings, which are often blended with other lines. On the other hand, velocity dispersion Δv depends more on good data quality (Dalla Bontà et al., 2020). Emission lines such as Hα λ6565 , Mg II λ2799, and CIV λ1549 are commonly used depending on the redshift (Greene & Ho, 2005; Shen et al., 2011; Vestergaard & Peterson, 2006). Nonetheless, certain lines also have their intrinsic biases, such as blueshifts in CIV, which can complicate the estimates (Coatman et al., 2017).

1.4.2 Bolometric Luminosity

Bolometric luminosity L_{bol} measures the total energy output of a quasar across all wavelengths, making it a crucial parameter as it indicates the overall power output from the SMBH accretion process. The most straightforward method to estimate bolometric luminosity is by integrating the quasar's SED across a wide wavelength range, from γ-rays to radio waves. However, obtaining comprehensive SED data is often difficult or impossible for some sources. Thus, bolometric corrections are commonly used to convert monochromatic luminosities at certain wavelengths (e.g., optical, UV, or X-ray) into an estimate of the total bolometric luminosity (**?**). These corrections vary based on the observed wavelength and can introduce systematic uncertainties, nevertheless they offer a practical solution for estimation L_{bol} when complete SED data is not available.

The bolometric luminosity, taking into account the bolometric correction, can be calculated by:

$$L_{\text{bol}} = \alpha \times L_{\lambda} \tag{1.6}$$

where L_{λ} represents the luminosity at a specific wavelength, and α is the coefficient used to convert the luminosity at this wavelength into the corrected bolometric luminosity.

Recent efforts to refine bolometric corrections for quasars have focused on enlarging the sample size, enhancing wavelength coverage, and considering different physical parameters that impact the SED of quasars. Runnoe et al. 2012 revised quasar bolometric corrections using detailed SEDs of 63 bright quasars, exploring various mathematical models and suggesting adjustments for viewing angle and anisotropic emission from accretion disks. Duras et al. 2020 conducted a comprehensive study on bolometric corrections spanning seven orders of magnitude in luminosity, offering universal corrections for both obscured and unobscured AGN. Their research highlighted the necessity of considering AGN luminosity when applying bolometric corrections.

1.4.3 Accretion Rate

The accretion rate, $\dot{M}$, is an essential parameter that indicates the rate at which a black hole accretes matter. This rate is crucial for the input and energy production of a quasar. The accretion rate can be indirectly deduced from the luminosity of the quasar using the following relationship:

$$\dot{M} = \frac{L_{\rm bol}}{\eta c^2} \tag{1.7}$$

where $L_{\rm bol}$ is the bolometric luminosity of the quasar, η is the efficiency of converting mass into energy, and c is the speed of light. The radiative efficiency η is typically assumed to be around 0.1 for quasars, based on models of accretion discs around black holes and observational data (see, e.g., Yu & Tremaine 2002; Shankar et al. 2009).

The accretion rate provides insight into how rapidly the black hole is growing. High accretion rates are typically associated with luminous quasars. Conversely, low accretion rates imply less luminous AGNs, possibly indicating that the growth of the black hole has slowed down, e.g., AGN cosmic downsizing indicates that as the universe evolves, the accretion rates onto SMBH decrease, leading to a shift from high-luminosity AGNs at earlier times to lower-luminosity AGNs in more recent epochs (Babić et al., 2007).

1.4.4 Eddington Luminosity

The Eddington luminosity $L_{\rm Edd}$, also known as the Eddington limit, represents a critical upper limit to the brightness that can be sustained by a black hole while maintaining a steady inflow of matter. It occurs when the outward pressure from radiation balances the inward pull of gravity on the inflowing gas. At this point, the radiation pressure halts further accretion unless the black hole can grow further and increase its gravitational pull. The Eddington luminosity is expressed as:

$$L_{\rm Edd} = \frac{4\pi G M_{BH} m_p c}{\sigma_T}, \tag{1.8}$$

where G is the gravitational constant, $M_{\rm BH}$ is the black hole mass, m_p is the proton mass, c is the speed of light, and σ_T is the Thomson scattering cross-section for electrons. This formula shows that $L_{\rm Edd}$ is directly proportional to the black hole mass. For a typical SMBH with a mass of $10^8 M_\odot$, the Eddington luminosity is approximately 1.3×10^{46} erg/s, about 10 trillion times greater than the energy output of our sun.

Understanding the Eddington limit is crucial for several reasons. It sets the maximum rate at which a black hole can grow through accretion. If a quasar is observed to have a luminosity near or above this limit, it suggests that the SMBH is accreting at a very high rate, potentially close to the Eddington limit. Furthermore, the Eddington ratio, defined as the ratio of the observed bolometric luminosity to the Eddington luminosity ($L_{\mathrm{bol}}/L_{\mathrm{Edd}}$), is a key parameter in studies of quasars. This ratio directly measures how efficiently the black hole is accreting matter. It is often used to characterize different types of AGNs, especially between lower-luminosity systems like Seyfert 1 or 2 galaxies and low-luminosity AGNs (LLAGN, see e.g., Ho 2008). Systems with Eddington ratios close to 1 are thought to be in a phase of rapid black hole growth (Kollmeier et al., 2006). The Eddington limit plays a crucial role in AGN feedback mechanisms, where powerful quasar winds, often triggered as accretion approaches the Eddington limit, are driven by radiation pressure. These winds can heat or expel gas from the host galaxy and regulate the star formation and the growth of black holes in the galactic center (Fabian, 2012).

1.5 Radio-loud quasars

In this section, I present a specific subset of quasars distinguished by their powerful jets. These quasars show notably strong radio emissions, which suggest the presence of a relativistic jet. Here, I define these quasars, discuss their prevalence within the quasar population, and describe the latest instruments used to detect them. In the next section, I will explain how this particular subgroup serves as a unique candidate for studying the early universe.

1.5.1 Radio-loudness in quasars

Radio-loudness is an observational quantity used to characterize how significant the radio emission is for a quasar compared to its optical or ultraviolet emission (Kellermann et al., 1989).

The radio-loudness parameter R is usually defined as the ratio of the flux density in the radio band to the flux density in the optical or other bands. It is expressed as:

$$R = \frac{F_{\mathrm{radio}}}{F_{\mathrm{optical/UV}}} \tag{1.9}$$

where F_{radio} is the flux density in the radio band (typically measured at rest-frame 5 GHz) and $F_{\mathrm{optical/UV}}$ is the flux density in the rest-frame optical or ultraviolet band (often measured in the B-band at 4400 Å).

Quasars are typically classified into two main categories based on their radio-loudness. Radio-loud (RL) quasars have $R \geq 10$, indicating strong radio emission relative to their optical/UV emission, while radio-quiet (RQ) quasars have $R < 10$, showing weaker radio emission compared to their optical/UV emissions.

1.5.2 Radio-loud fraction in quasars

The radio-loud fraction (RLF) in quasars refers to the percentage of RL quasars in the overall quasar population. This fraction is generally thought to be around 10−20% of the quasar population at low redshift (Kellermann et al., 1989; Ivezić et al., 2002). The distinction between RL and RQ quasars is significant for understanding the diversity of quasar behavior and the role that jets play in the evolution of quasars and their host galaxies. Studying the RLF at different redshifts helps us understand the formation and evolution of jets in quasars. At $z \sim 6$, RLFs have been reported to be $8.1^{+5.0}_{-3.2}\%$ (Bañados et al., 2015) and $3.8^{+6.2}_{-2.4}\%$ (Keller et al., 2024). This is slightly lower than estimates at lower redshifts but is still consistent with no redshift evolution of the RLF. The relative number of RL quasars has also been found to be a function of optical luminosity. Padovani 1993 reported that the fraction range from approximately 20−50% for relatively bright quasars of $M_B \lesssim -24.5$ to about 7−8% at fainter magnitudes. A deeper and wider radio survey of a large quasar sample is needed to detect radio continuum emission from quasars at $z > 6$, and to examine the RLF at higher redshifts.

1.5.3 Black hole masses of Radio-loud quasars

RL and RQ quasars exhibit differences in their black hole properties. Several studies have found that RL quasars tend to host more massive black holes compared to their RQ counterparts (Laor, 2000; McLure & Jarvis, 2004). For instance, Laor 2000 reported a clear distinction in black hole masses, with RL quasars predominantly having $M_{\rm BH} \gtrsim 10^9 M_\odot$, while RQ quasars span a wider range of masses. This mass difference has been attributed to the possibility that more massive black holes are required to launch and sustain powerful relativistic jets (Sikora et al., 2007).

Nevertheless, the relation between radio-loudness and black hole mass remains debated. Ho 2002 have found a more scattered relationship between the black hole mass and the radio-loudness, suggesting that factors beyond black hole mass may play a crucial role in determining radio-loudness. The Eddington ratio λ_{Edd} has also been investigated as a potential discriminator between RL and RQ quasars. Several studies have reported an anti-correlation between radio-loudness and λ_{Edd} (Ho, 2002; Sikora et al., 2007), implying that RL quasars may accrete less efficiently than their RQ counterparts. This finding has led to the hypothesis that the accretion mode (e.g., radiatively efficient vs. inefficient) might be a key factor in determining the radio properties of quasars (Best & Heckman, 2012). Despite these trends, recent works, such as Gürkan et al. (2019), have also challenged the notion of a clear dichotomy between RL and RQ quasars, suggesting a continuous distribution of radio properties across the quasar population, given that there are also jets detected in RQ quasars (Sbarrato et al., 2021).

1.5.4 Radio sky surveys

Recent advances in radio surveys have greatly enhanced the identification of quasars with strong radio emissions. Below, I highlight some important ones and list their features in Tab. 1.1.

The Very Large Array Sky Survey (VLASS, Lacy et al. 2020; Gordon et al. 2021) is a comprehensive radio survey that aims to map the entire sky north of −40° declination at a frequency of approximately 3 GHz. Initiated with its first epoch completed in 2019, VLASS produces high-resolution images with a median beam size of 2 ″, making it the smallest beam size among near-all-sky radio continuum surveys to date. The survey has generated Quick Look images covering around 34,000 square degrees, with a typical noise level of 120 μJy beam≏1. This capability allows for the identification of a vast number of radio sources, including resolving those with complex morphologies such as double radio sources (see, e.g., Gordon et al. 2023). The Rapid ASKAP Continuum Survey (RACS, Hale et al. 2021) utilizes the Australian Square Kilometre Array Pathfinder (ASKAP) to conduct a wide-field radio survey at 888 MHz. RACS aims to cover the entire southern sky, providing high-resolution images with a focus on detecting both faint and bright radio sources. The first data release of RACS has already contributed to various scientific investigations, including identifying new $z > 5$ radio-loud quasars (Ighina et al., 2024). LOFAR (Low-Frequency Array, Shimwell et al. 2022) is a radio telescope network designed to observe the universe at low frequencies (30 MHz to 240 MHz). It consists of multiple stations across Europe, enabling it to achieve high sensitivity and resolution. Its capabilities extend to imaging large areas of the sky and conducting deep surveys, enabling surveys like the LOFAR Two-metre Sky Survey (LoTSS) to be effective in identifying new $z > 5$ radio-loud quasars at low frequencies (Gloudemans et al., 2021;

Bañados et al., 2023).

The Square Kilometre Array (SKA) represents the next generation of radio telescopes. With construction underway in South Africa and Australia, the SKA will be the world's largest radio telescope when completed, offering unprecedented sensitivity and resolution across a wide range of frequencies. The SKA-Low, operating at 50−350 MHz, and SKA-Mid, covering 350 MHz to 15.3 GHz, will enable transformative science across a broad range of astrophysical topics in radio regime (Dewdney et al., 2009). For high-redshift quasar studies, the SKA's capabilities are particularly promising. Its high sensitivity is expected to detect many faint radio objects at $z > 6$, potentially uncovering a population of objects that current facilities cannot observe due to sensitivity and resolution (Afonso et al., 2015). The SKA will also revolutionize 21-cm forest studies (detailed in the next section), with the potential to detect and resolve individual absorption features in the spectra of bright radio sources at $z > 6$, providing unique insights into the epoch of reionization (EoR, typically at $6 \lesssim z \lesssim 30$) when the first stars and galaxies formed, ionizing the surrounding hydrogen gas to transform the universe from a dark period rich in neutral gas to transparent (Ciardi et al., 2015). Furthermore, the SKA's wide-field surveys will increase the number of known radio-loud quasars at high redshifts, enabling statistical studies of their evolution and their relationship to galaxy formation in the early universe (Jarvis et al., 2015). The combination of SKA's sensitivity, resolution, and survey efficiency will make it an unprecedented tool for studying the radio properties of high-redshift quasars and their environments. Further discussion of radio-loud quasars in the early universe will be detailed in the next section.

Survey	Frequency	Sensitivity	Coverage	Resolution	Ref.
LoTSS	150 MHz	100 μJy/beam	14%	$6''$	[1]
RACS	888 MHz	300 μJy/beam	82%	$15''$	[2]
VLASS	3 GHz	120 μJy/beam	82%	$2.5''$	[3]
NVSS	1.4 GHz	450 μJy/beam	82%	$45''$	[4]
FIRST	1.4 GHz	150 μJy/beam	25%	$5''$	[5]
SUMSS	843 MHz	1 mJy/beam	23%	$45''$	[6]

Table 1.1. Sensitivity of detection, sky coverage (percentage of the entire sky), and typical resolution for selected radio surveys. Currently, many radio surveys are updating previous ones with unprecedented coverage and resolution at increasingly higher sensitivity, improving our ability to detect more radio-loud quasars and understand the early universe through radio observations.
References: [1]: Shimwell et al. 2022; [2]: Hale et al. 2021; [3]: Gordon et al. 2021; [4]: Condon et al. 1998; [5]: Becker et al. 1995; [6]: Mauch et al. 2003

1.6 Quasars in the Early Universe

1.6.1 Discovering Quasars in the Early Universe

The identification of quasars at $z > 5$ is exceptionally difficult due to their immense distance and low brightness. High-redshift quasars often lie behind unnumerable intergalactic medium (IGM) layers that absorb light at specific wavelengths, particularly in the region bluewards to the Lyman-alpha line. Moreover, bright foreground stars, notably ultracool dwarfs that have very similar colors to high-redshift quasars but outnumber them by nearly a factor of $\sim 10^5$ (Bochanski et al., 2010), further complicating their discovery (see, e.g., Fan et al. 2006; Bañados et al. 2016; Yang et al. 2023 for recent discoveries on high-redshift quasars).

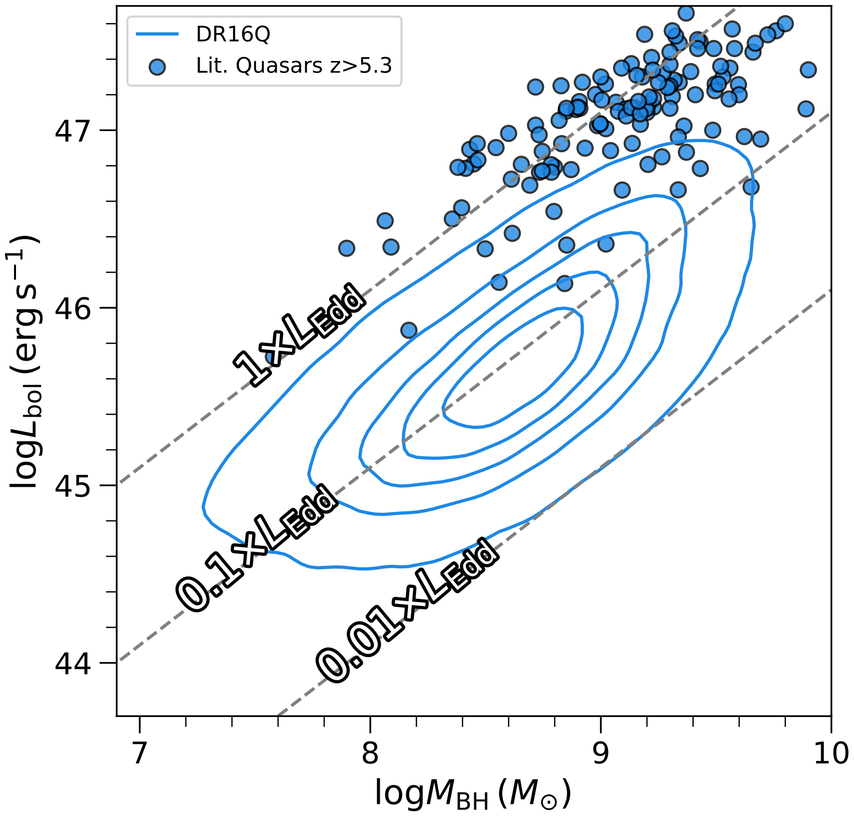

Figure 1.6. The black hole mass, bolometric luminosity, and accretion rate for quasars with z> 5.3 are compared to those of low-redshift quasars (z< 2.7). The contour represents low-redshift quasars from the Sloan Digital Sky Survey (SDSS). The physical properties of these low-redshift quasars in SDSS are derived from the SDSS DR16Q data by Wu & Shen 2022.

Radio observations provide essential tools for detecting high-redshift quasars, as radio emissions can help rule out contamination from foreground objects such as ultracool dwarfs as they tipically have no radio signal (Burningham et al., 2016; Gloudemans et al., 2021). Radio surveys provide a wide field of view, enabling efficient searches for targets. Despite the fraction of radio-loud quasars being small, deep radio surveys like LoTSS have identified radio counterparts for a much larger fraction of high-redshift quasars, up to 36% at $z > 5$ (Gloudemans et al., 2021; Bañados et al., 2023). Radio emissions are reliable indicators of quasar activity because they remain largely unaffected by IGM absorption. Incorporating radio data into quasar selection algorithms improves the detection of faint sources that optical and infrared surveys might overlook (Wagenveld et al., 2022). The forthcoming SKA will provide deeper radio observations across extensive sky areas, likely resulting in the discovery of many more radio-luminous quasars from the early universe (Dewdney et al., 2009; Koopmans et al., 2015).

1.6.2 Origins of SMBH

One of the most significant challenges in understanding early quasars lies in explaining the rapid growth of their central SMBH. Quasars with black hole masses greater than $10^9 M_\odot$ have been observed at

$z > 6$, merely a few hundred million years after the Big Bang (Wu et al., 2015). Traditional accretion models, which consider Eddington-limited growth rates, struggle to account for the formation of such massive black holes within this limited timeframe. Recent findings of high-redshift quasars impose more constraints on black hole growth models. Quasars discovered at $z > 7$ offer critical data for refining these models, particularly the mass of their seeds and accretion efficiency (Inayoshi et al., 2020).

One scenario suggests that these SMBH originated from the remnants of Population III stars (Pop III stars), representing the first generation of stars in the universe. It is thought that Pop III stars emerged in minihaloes with masses around $\sim 10^6 M_\odot$ at redshifts $z \gtrsim 20$ (Couchman & Rees, 1986; Bromm & Larson, 2004). Due to the early universe's lack of metals and inefficient cooling, these stars were likely very massive, typically between 100 and 1000 $M_\odot$ (Abel et al., 2002; Hirano et al., 2014). Upon their death, Pop III stars may have directly collapsed into black holes due to their masses, creating seeds for future SMBH growth (Madau & Rees, 2001). However, it remains challenging for these low-mass seeds to grow into SMBHs by $z \sim 7$, as this requires sustained super-Eddington accretion rates over extended periods (Pezzulli et al., 2016; Inayoshi et al., 2020). Recent research looks into several mechanisms to boost the growth of Pop III remnants, such as episodes of super-Eddington accretion (Pacucci et al., 2015) and the merger of multiple Pop III remnants in dense environments (Regan et al., 2020).

Another possibility is that dense star clusters might help the formation of intermediate-mass black holes (IMBHs), which can act as precursors to SMBH. In this context, dynamic mechanical interactions within young, massive star clusters result in stars undergoing runaway collisions. It involves accelerated and rapid mergers of massive stars, which aids the quick formation of a large object, potentially a massive star that subsequently collapses into an IMBH (Portegies Zwart et al., 2004; Lupi et al., 2014). These IMBHs can then grow through gas accretion and mergers, eventually becoming SMBHs. Recent simulations by Shi et al. 2024 show that black hole seeds captured by gas-rich young star clusters, typical of the high-redshift universe, can quickly grow to $\gtrsim 10^6 M_\odot$. The creation of IMBHs via this method has been widely studied, with various models examining the impact of stellar evolution and gas accretion on the growth of the central black holes (see, e.g., Giersz et al. 2015; Mapelli 2016). Additionally, recent LIGO/Virgo observations of gravitational waves from IMBH mergers provide observational evidence for IMBH existence (see, e.g., Abbott et al. 2020). On another note, Häberle et al. 2024 used Hubble Space Telescope (HST) observations of seven fast-moving stars in the central region of ω Centauri, a globular cluster, to identify velocities exceeding the clusters escape velocity, suggesting strong evidence for a $\sim 8200 M_\odot$ IMBH at its core.

A different scenario for forming massive black hole seeds is via direct collapse black holes (DCBHs), which could have initial masses up to $10^5 - 10^6 M_\odot$ (Volonteri & Bellovary, 2012; Woods et al., 2019). The DCBH model involves collapsing a substantial, nearly metal-free gas cloud within atomic-cooling haloes. These haloes grow massive enough for efficient gas cooling through atomic transitions rather than molecular hydrogen cooling, enabling a rapid collapse with less fragmentation. They have virial temperatures $T_{\rm vir} \gtrsim 10^4$ K, where the cooling effect of molecular hydrogen is suppressed by a significant Lyman-Werner radiation background that dissociates molecular hydrogen (Omukai & Palla, 2001; Bromm & Loeb, 2003). Under these conditions, the gas can collapse almost isothermally, preventing fragmentation and potentially leading to the formation of a supermassive star, which eventually collapses into a massive black hole seed (Latif et al., 2013; Chon et al., 2018). Although the DCBH model offers a plausible method for creating massive black hole seeds, the specific conditions needed, such as a metal-free gas cloud, a strong Lyman-Werner radiation background, or rich sustained gas inflows at the core, may have been uncommon in the early universe, thereby potentially limiting the number of SMBHs formed through

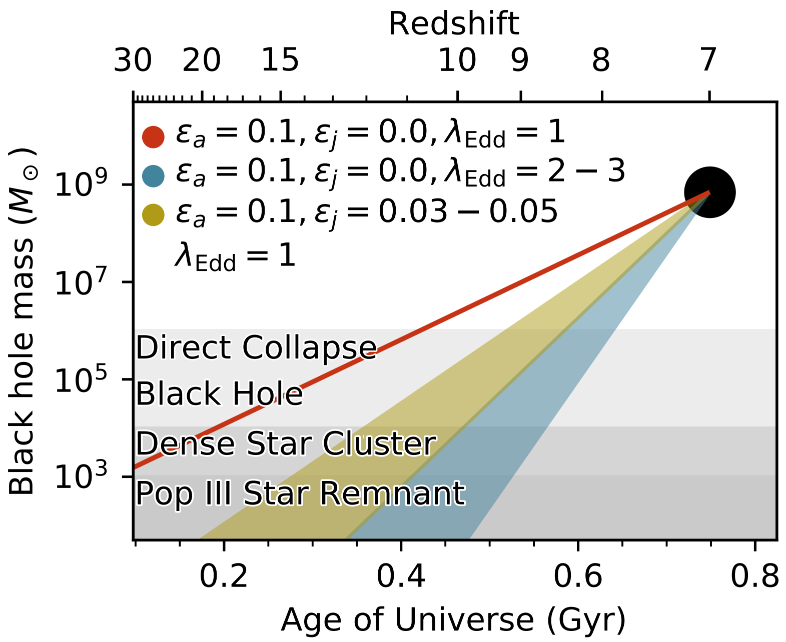

Figure 1.7. The growth models of early quasars with their potential seed scenarios, and evolutionary tracks characterized by different Eddington ratios λ_{Edd} and jet efficiencies ϵ_j. Jets enables a more efficient accretion phase, permitting scenarios with less massive black hole seeds.

this mechanism (Habouzit et al., 2016). With the discovery of more high-redshift quasars in upcoming and current surveys such as Euclid, we anticipate further advancements in constraining models of black hole formation and evolution during the early universe (Euclid Collaboration et al., 2019, 2022).

1.6.3 Radio-loud Quasars in the Early Universe

As discussed in an earlier chapter, jets can aid black hole growth, particularly by improving mass accretion efficiency. This is further explored through radiative efficiency trapping (Sadowski & Narayan, 2016). In this framework, the intense bipolar kinetic outflows or jets inject momentum and energy into the surrounding medium and prevent mass accretion onto the BH; thus, the radiative output from the accreting BH is “trapped” and reduced. Takeo et al. 2020 found that during this process, the mass inflows through the equatorial region are not affected and can still enable intense inflows of gas and hold the accretion rate BH accretion rate to as high as 10^3 of Eddington limit. Numerical models by Jiang et al. 2019 also reveal that the radiation pressure on the inflowing gas will be reduced by up to an order of magnitude and allow black holes to accrete above the Eddington limit, enabling rapid growth of SMBH in the early universe. Furthermore, interactions between jets and the surrounding gas may induce a maintained gas inflow, thus enhancing efficient black hole growth (Gaspari et al., 2013). Therefore, the detection of quasar jets in the early universe provides important evidence that supports the growth of massive quasars at high redshift.

The identification and further study of relativistic jets in high-redshift quasars are also essential for understanding the feedback mechanisms in the early universe. Jets from radio-loud quasars can deliver substantial energy to their environments, possibly expelling gas from the host galaxy and regulating star formation (Fabian, 2012; Harrison et al., 2018). Consequently, the existence or non-existence of jets in high-redshift quasars might significantly influence the development of the largest galaxies during the early stages of the universe. Prominent feedback observed in high-redshift quasars indicates that these processes are notably effective in shaping their host galaxies (Fabian, 2012). Radio observations also reveal that some early quasars are located in galaxies with abundant gas reserves and high star-formation rates (see, e.g., Venemans et al. 2016). More observational evidence is needed to understand the co-evolution of black holes and galaxies in the early universe, especially how quasar feedback eventually ceases black hole growth and star formation in lower redshift (Kormendy & Ho, 2013).

The relative rarity of radio-loud quasars at high redshifts also raises important questions about the conditions necessary for jet formation in the early universe. As in the previous section, investigating the radio-loud fraction of quasars as a function of redshift can provide insights into how the accretion state of SMBHs may have evolved over cosmic time (Volonteri et al., 2015). Additionally, studying the relationship between radio-loudness and other quasar properties, such as black hole mass or accretion rate, may shed light on the physical processes governing jet formation and the role of magnetic fields in the innermost regions of accretion disks around early SMBHs (Sikora et al., 2007).

1.6.4 21cm Forest Study

The 21 cm forest is a sequence of absorption lines detected in the spectra of distant, radio-emitting sources like quasars. These features are due to neutral hydrogen in both the IGM and galaxies along our line of sight (Carilli et al., 2002; Furlanetto & Loeb, 2002). It is similar to the Lyman-alpha forest absorption seen in the optical spectra of quasars, but it probes neutral hydrogen through its 21 cm hyperfine transition in radio wavelengths (Madau et al., 1997). The 21 cm forest holds significant value for cosmology for multiple reasons. It probes much smaller scales and lower density regions than the Lyman-alpha forest, potentially unveiling the structure of the cosmic web and properties of the early galaxies (Semelin, 2016). Also, observations of the 21 cm forest can help constrain cosmological parameters, the nature of dark matter, and the physics of galaxy formation in the early universe (see, e.g., Shimabukuro et al. 2014; Kadota et al. 2021).

The study of the 21 cm forest with radio telescopes is especially promising for exploring the EoR, when obscurations are too heavy for other wavelengths. The 21 cm emission is sensitive to the density and temperature of neutral hydrogen, enabling us to map the distribution of baryonic matter in the early universe using radio telescopes (see, e.g., Furlanetto et al. 2006; Ciardi et al. 2013). By studying the absorption characteristics, it is possible to deduce the neutral fraction, temperature, and density of the IGM along the line of sight to the background source (Mack & Wyithe, 2012). This information is vital for understanding the reionization process, including its timing, duration, and spatial inhomogeneity. Additionally, the 21 cm forest may unveil the existence of minihalos and other small-scale structures that are challenging to detect by other means, thus providing valuable information on the early phases of galaxy formation (Xu et al., 2021).

The SKA and other upcoming radio telescopes are anticipated to enhance the sensitivity and resolution of such observations, potentially enabling the detection of 21 cm signals from redshifts as high as $z > 7.5$ (see, e.g., Ciardi et al. 2015). Detecting more radio-loud quasars at high redshifts can also provide significant benefits for 21 cm forest studies. Firstly, radio-loud quasars act as luminous background sources, against which 21 cm absorption can be measured. The brighter the source, the higher the signal-to-noise ratio of the absorption features, resulting in more accurate measurements of the IGM properties (Semelin, 2016). Secondly, having a larger sample of radio-loud quasars across different redshifts would allow one to examine the IGM along multiple lines of sight, offering a more detailed three-dimensional view of the reionization process (Ewall-Wice et al., 2014). Lastly, the existence of radio-loud quasars at very high redshifts ($z > 8$) would help us understand the IGM during the initial stages of reionization, potentially uncovering the first sources of ionizing radiation and their impact on their environment (Ciardi et al., 2013).

1.7 This thesis

The detailed work in the thesis is divided into three segments.

The first part of this research focuses on blazars, a subgroup of quasars with radio jets directed at us at a narrow-angle. Chapter 2 introduces an analytical algorithm to identify the compact blazar morphology from radio images. The algorithm distinguishes blazars from non-blazars in a dataset composed of numerous blazar candidate catalogs.

To validate the algorithm, Chapter 3 discusses the study that focuses on an AGN in which the algorithm classified as a non-blazar despite being reported as a blazar candidate in previous work. The study includes follow-up observation using the Very Large Telescope (VLT), and by examining its optical spectra and radio characteristics, the blazar candidate is confirmed *not* to be a blazar, thereby demonstrating the algorithm's accuracy.

The second part shifts focus to the radio-loud quasars in the distant universe. This part employs numerous observational data from ground-based telescopes to investigate their black hole properties. It aims to answer critical questions: How do supermassive black holes grow so heavy in the early universe? Is there observational evidence that radio jets aid in the growth of their central black holes? What additional outflow characteristics could provide insight into the impacts of radio jets?

In Chapter 4, four quasars with prominent radio jets are analyzed. Each quasar has a redshift above 5.5, and observational data are collected and examined to determine their black hole properties using the broad lines of MgII and CIV. The chapter also compares these high-redshift jetted quasars with radio-quiet and radio-loud SDSS quasars and high-redshift radio-quiet quasars.

The final conclusion section summarizes the thesis and offers an outlook of future opportunities, a perspective on forthcoming data with Large Binocular Telescope (LBT), offering 22 more radio-loud quasars with redshifts greater than 5, and additional potential analyses.

I

First part

2

Chapter 2

2.1 Background

A large sample of blazars is necessary to study their radiation mechanism and relativistic jet beaming effects. However, confirming a large number of blazars is time and resource-consuming (e.g., Shaw et al. 2012). The Roma-BzCAT is currently the most comprehensive collection of confirmed blazars, containing $3,561$ sources that are classified as BL Lac or FSRQ (Massaro et al., 2015). All blazars in Roma-BzCAT must meet the criteria of having spectroscopic information showing characteristic features of their class, at least one radio detection exhibiting compact morphology or one-sided jet and an isotropic X-ray luminosity close to or higher than $10^{43}\,\mathrm{erg\,s^{-1}}$ (Massaro et al., 2009).

In an effort to expand the pool of identified blazars while minimizing the presence of potential contaminants, primarily other forms of AGN, D'Abrusco et al. (2012) studied the mid-infrared (MIR) colors of established blazars, employing the Wide-Field Infrared Survey Explorer (WISE, Wright et al. 2010) to uncover a distinctive color region in which blazars reside. D'Abrusco et al. (2014) assembled a catalog of blazar candidates (WIBRaLS) based on their WISE IR colors (W1-W2, W2-W3, W3-W4), while requiring the existence of a radio counterpart either in the NRAO VLA Sky Survey (NVSS, Condon et al. 1998) or the Sydney University Molonglo Sky Survey (SUMSS, Mauch et al. 2008). More recently, they used a larger sample of confirmed blazars and radio data from the Faint Images of the Radio Sky at Twenty-cm survey (FIRST, Becker et al. 1994) to recognize additional blazar candidates (WIBRaLS2; D'Abrusco et al. 2019). They also established a second catalog, KDEBLLACS, which employs only W1-W2 and W2-W3 colors (i.e., excluding a W4 requirement) to detect fainter candidates. KDEBLLACS sources also must have a radio counterpart. The total number of blazar candidates from WIBRaLS, WIBRaLS2, and KDEBLLACS is $17,996$. A recent study by de Menezes et al. (2019) analyzed the Sloan Digital Sky Survey spectra for available objects in the D'Abrusco et al. (2019) catalogs and estimated that $\gtrsim 40\%$ of them are contaminants, primarily quasars and galaxies. While spectroscopic follow-up is essential for determining the nature of blazar candidates, an approach for removing contaminants from a large pool of blazar candidates would greatly aid in more efficient follow-up investigations to determine their true nature. We notice that at the angular resolution of radio surveys used by D'Abrusco et al. 2014, 2019 ($\sim$45″ for both NVSS and SUMSS, $\sim$5″ for FIRST), the radio structure for most blazar candidates is not resolved, particularly for sources outside the FIRST footprint.

In this chapter, we take advantage of the radio images of Very Large Array Sky Survey (VLASS, Lacy et al. 2020; Gordon et al. 2021). At the time of this study, VLASS provides two-epoch[1] 3 GHz images for all the sky above Decl.> -40 deg at a higher angular resolution than previous large sky radio surveys ($\sim$2.5″). Since the blazar's jet is directed towards us at a small angle, the VLASS radio morphology is expected to be compact. We note that the actual morphology of blazars could be more complicated. For example, Kharb et al. (2010) showed that some of the blazars in the MOJAVE (Monitoring Of Jets in Active galactic nuclei with VLBA Experiments; Lister et al. 2021) sample exhibit both compact and

[1] In January 2023, VLASS started observing a third epoch of the sky. We only use the first two epochs in this study.

extended emission at 1.4 GHz. However, we will show that at the VLASS frequency, resolution, and sensitivity, most of the MOJAVE blazars are classified as compact objects. Thus, if the VLASS images resolve a clear two-sided jet pattern, we can conclude that the radio source is likely not a blazar.

The focus of the work in this chapter is the introduction of an automated algorithm that utilizes publicly available VLASS 3 GHz radio images to classify sources whose morphology are compatible or not with being blazars. Throughout this work, we adopt a flat ΛCDM cosmology with H_0=70 km s^{-1} Mpc^{-1}, Ω_M=0.3, and Ω_Λ=0.7, and all magnitudes are reported in the AB magnitude system.

2.2 Data

Our dataset comprises a combination of three catalogs: Roma-BzCAT (Massaro et al., 2015), WIBRaLS (D'Abrusco et al., 2014, 2019), and KDEBLLACS (D'Abrusco et al., 2019). WIBRaLS and KDEBLLACS contain blazar candidates, while Roma-BzCAT consists of confirmed blazars. We download all available epochs of the VLASS Quick Look Images for the sources in this dataset. VLASS1.1 corresponds to the first epoch of the first half of the sky, and VLASS1.2 is the first epoch of the second part of the sky. The first epoch is completed in 2019, while the second epoch, VLASS2.1 and VLASS2.2, is completed in June 2022. There are upgrades in the image processing pipeline between epochs 1 and 2, producing cleaner radio images for both faint and bright sources by fixed pipeline issues (for more details, refer to Lacy et al. 2022).

The blazar candidates in WIBRaLS/WIBRaLS2 (hereafter referred to as WIBRaLS) are selected based on two criteria that must be satisfied simultaneously: i) having similar WISE colors (W1−W2 and W2−W3, and W3−W4) as known blazars in Roma-BzCat, and ii) having a radio counterpart. Meanwhile, KDEBLLACS complements WIBRaLS by adding fainter candidates that were not detected in the W4 band.

Initially, our dataset includes a total of 12,416 blazar candidates from the WIBRaLS and WIBRaLS2 catalogs. We find that 9,821 candidates have VLASS Quick Look Image coverage, with 9,061 sources having two VLASS epochs and 220 sources having only one epoch. For KDEBLLACS, there are a total of 4,996 out of 5,580 sources with VLASS coverage, with 4,926 two-epoch sources and 70 one-epoch sources. Out of 3,561 blazars in Roma-BzCAT, 3,134 sources have VLASS images, with 3,078 sources having two epoch images and 56 sources having only one epoch. In this study, we do not differentiate between subclasses of blazars.

2.3 Method

2.3.1 Automated algorithm of morphology recognition

In VLASS images, jet patterns are easily recognizable by the human eye, and manual morphological classification can be achieved through visual inspection. However, our objective is to develop an automated algorithm that can mimic human visual classification in an objective and reproducible way. To achieve this, we download $2' \times 2'$ VLASS images centered on known blazar/candidates with catalog coordinates and utilize the *zscale* algorithm (Tody, 1986) to process the images into machine-readable masked values. The *zscale* algorithm is specifically designed to display images near their median in a computationally efficient way without the need to compute the entire pixel value distribution histogram. This algorithm is particularly useful in highlighting peaked patterns that are brighter than the background, making them

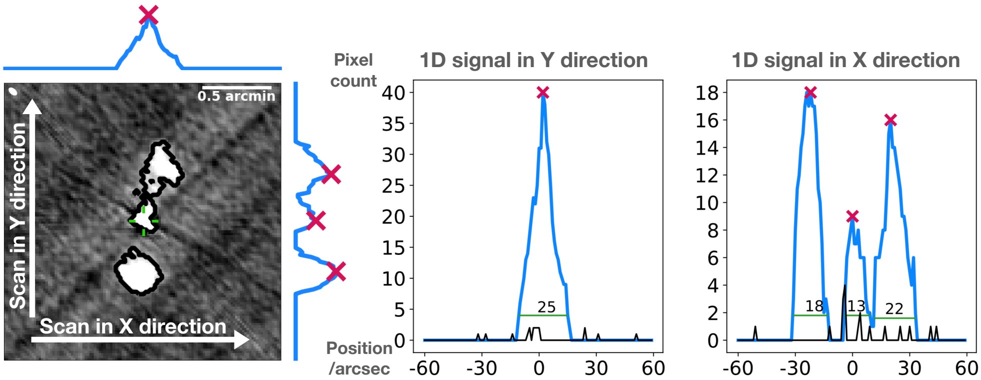

Figure 2.1. An illustration of the automated morphological classification algorithm applied to VLASS images (The beam size is denoted in the top left corner, is approximately $1.8'' \times 2.9''$). The algorithm processes each image, converting it into binary values (marked sections are depicted by black contour lines) based on their flux. Each of the 1D curve (blue line) represents the pixel count in a single scanning row in the selected direction, denoted by the white arrows in the image. Cross markers overlayed on the 1D curve indicate peak locations within the 1D curve, which are used to assign morphological classifications to the sources. A green line on the plot represents the peak width measured by each of their relative height. The value in number of pixels is shown, which also contributes to determining the morphological class of the sources (refer to Sec. 2.3.2 for details).

more discernible in astronomical images. The *zscale* algorithm returns two limits in pixel values denoted as zs_{up} and zs_{low}. Pixels whose values are above zs_{up} appear bright while those with values below zs_{low} appear dark.

Next, our algorithm focuses specifically on pixels with values $\geq zs_{up}$, as these pixels provide a good representation of the source's morphology of their radio emission. By only calculating the distribution of the brightest pixels, the algorithm can obtain a proxy of the source's morphology, as shown by the black contours in Fig. 2.1.

The next goal is to classify the morphology, estimated by the highlighted pixel in each image. Our algorithm transforms the shape of the source in the VLASS image onto two 1D lines, generated by stacking the pixel counts in the respective direction. The height and width of the single-/multi-peaked 1D curve in the resulting plots represent the morphological characteristics of the radio source (see Fig. 2.1 for an example).

2.3.2 Classifications on morphologies

Our algorithm provides a morphological classification for each image by analyzing the shape of the signals obtained from processing the VLASS images into 1D curves. The algorithm classification can then be split into two groups: those displaying blazar-like and non-blazar-like morphologies. Examples of all subclasses are shown in Fig. 2.2. Below, we explain how we identify each morphology classification from their 1D signal.

We categorize all sources with blazar-like morphologies into four subclasses: *COMPACT*, *OFFSET*, *1-SIDE SEPARATED* and *1-SIDE EXTENDED*. We list the details for each blazar-compatible subclass and their morphological features below:

COMPACT The VLASS image exhibits a compact unresolved source, indicating that the morphology is consistent with a jet directed towards us at a very small angle (see Fig. 2.2, top left). A *COMPACT*

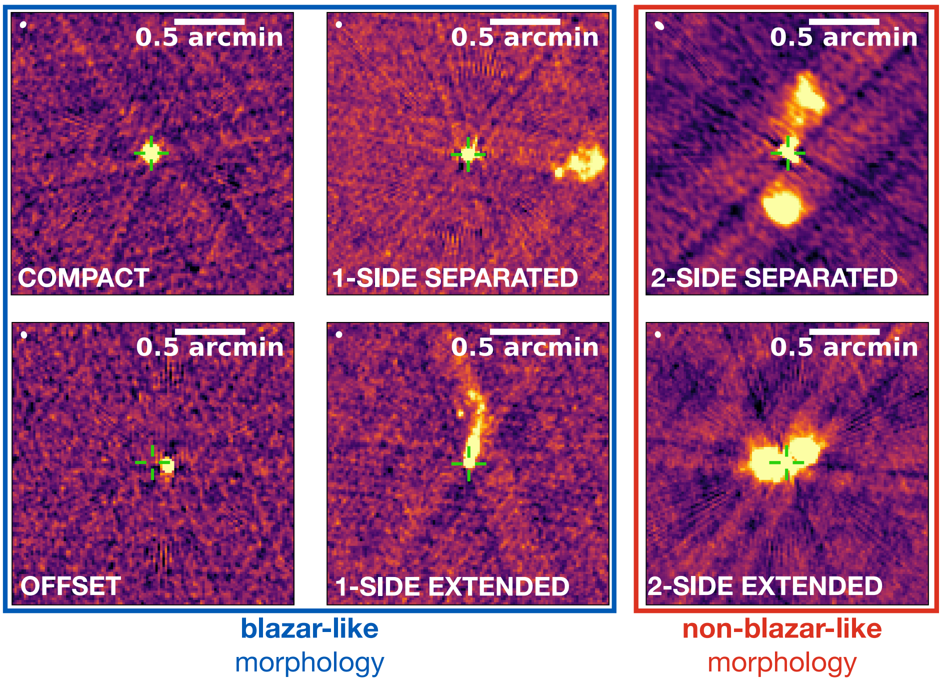

Figure 2.2. Morphological classification of VLASS images using our automated algorithm. The images are categorized into six distinct morphological classes, grouped into two sets. Blazar-like morphologies include *COMPACT*, *OFFSET*, *1-SIDE EXTENDED*, and *1-SIDE SEPARATED*; while non-blazar-like morphologies comprise *2-SIDE EXTENDED* and *2-SIDE SEPARATED*. In each morphological class, their corresponding 1D signals are shown in two directions, indicated by blue lines. Automatically identified peaks are marked by pink crosses, with morphological classification determined by the properties of peaks, including number, width and distance to the center position. Descriptions of each morphological class and their characteristics can be found in Sec. 2.3.2.

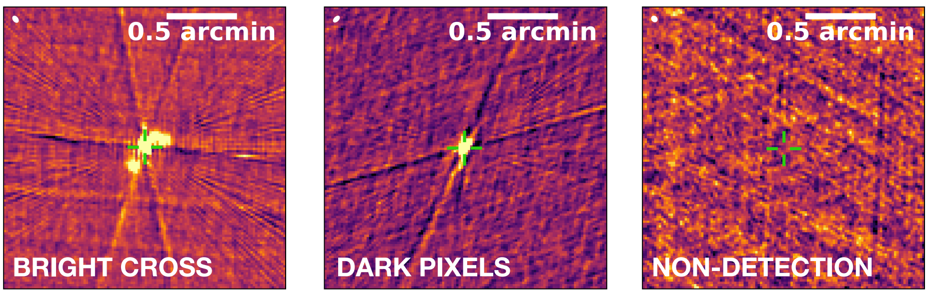

Figure 2.3. An illustration of two artifact types and a *NON-DETECTION* source in VLASS images. The algorithm identifies cross pattern and dark pixel artifacts, assigning appropriate quality flag values (1 for cross pattern presence, 2 for dark pixel presence, and 3 for both artifacts in the image). Sources with low signal-to-noise ratios that are difficult to discern by visual inspection are classified as *NON-DETECTION* sources.

source is identified as a single peak in both row and column 1D signal, representing a single bright pixel cluster located in the central region of the VLASS image.

OFFSET The radio image shows one source that resembles the *COMPACT* class, but whose optical/mid-infrared coordinates are offset from the compact radio source. To determine a source as *OFFSET*, we examine the positions of two peaks in the row and column signals and calculate the offset value by measuring the distance to the catalog position. We classify sources as *OFFSET* when their compact radio emission is at least $5''$ away from the position listed in the catalogs (see Fig. 2.2, bottom left as an example). This can happen when using lower-resolution radio surveys than VLASS and incorrectly associating the radio emission from another close source with its optical counterpart. A source is not classified as *OFFSET* if its offset surpasses $10''$, to avoid potential misidentification with an incorrect source deviating from the catalog position. For additional details, refer to Sec. **??**.

1-SIDE SEPARATED The radio image reveals two distinct radio sources, with one precisely at the location of a confirmed blazar or blazar candidate. Such a morphology is recognized as a typical blazar morphology in Roma-BzCAT (Fig. 2.2, top middle). For a *1-SIDE SEPARATED* source, the 1D signal displays exactly two peaks, either in row or column, or both, depending on the jet's orientation. If the jet aligns with the row or column direction, only a single peak will be observed in the corresponding direction.

1-SIDE EXTENDED The radio image exhibits a connected, extended structure with its core aligning with the catalog position of the blazar or blazar candidate. In this scenario, the jet extends to one side. Similar to the *1-SIDE SEPARATED* morphology, this configuration also represents a central source emitting a jet oriented towards us at a small angle, and it is thus considered to be compatible with a blazar morphology (Fig. 2.2, bottom middle). The 1D signal displays a single peak in both row and column, as the center is connected with the extended radio lobe, suggesting only one radio blob exists in the image. However, the peak should also have a width larger than $15''$. We choose this value to be greater than a circle centering at the source, where we estimate the dynamic range to identify potential artifacts. This area has the radius of $7''$ ($\sim$2-3 times of the beam size, see also Sec. 2.3.3 for details). Consequently, the peak position is not centrally located but shifted in the projected direction that the jet extends.

We identify sources that show 2-side symmetrical jets as likely non-blazars, implying their viewing angle is likely not close to our line of sight. The two subclasses of sources with non-blazar-like morphologies are described below (also refer to the right side of Fig. 2.2):

2-SIDE SEPARATED The radio image displays two symmetrical jets on either side of the central core. The observed comparable separations for both jets in *2-SIDE SEPARATED* sources suggest that the jets are nearly perpendicular to our line of sight, thereby excluding them as blazars. The 1D signal exhibits exactly three peaks in row and/or column. Similar to the *1-SIDE SEPARATED* morphology, the jet angle can influence the number of detected peaks. If the jets align with either row or column, fewer than three peaks will be displayed. However, the other direction will still identify three peaks, classifying the source as a *2-SIDE SEPARATED* morphology.

2-SIDE EXTENDED The radio image presents two symmetrical jets, similar to the *2-SIDE SEPARATED* objects. The distinguishing feature of *2-SIDE EXTENDED* sources is that the lobes and the core are interconnected at the resolution of our images, exhibiting similar extension sizes. Following the same logic as the *2-SIDE SEPARATED* case, these jets must be nearly perpendicular to our line of sight. In the 1D signal of a *2-SIDE EXTENDED* source, the peak is closer to the center than in *1-SIDE EXTENDED*, as the jets extending from the central source in both directions rather than just one. We determine that if the peak (center of the radio source) is within 10 $''$ ($\sim$3 times of the beam size, also being out of the 7$''$ circle where we assess the dynamical range) from the catalog position, it will be categorized as *2-SIDE EXTENDED*; otherwise, it will be regarded as *1-SIDE EXTENDED*.

In addition to blazar-like and non-blazar-like classifications, we observe sources that exhibit no visible radio emission in VLASS images. We categorize these sources as *NON-DETECTION*.

NON-DETECTION The radio image displays no visible features near the catalog position. We assess the signal-to-noise ratio (S/N) to determine if the source is detected. The S/N is computed as the peak flux density within a 10$''$ circle surrounding the source, divided by the noise. The noise for each image is the root-mean-square value of all pixels, following a 2.5σ clipping of the image. If a source's S/N is below 5.0, it will be classified as *NON-DETECTION*. The 1D signal reveals no significant peaks exceeding the noise level (for example, see the right panel in Fig. 2.3).

This classification approach effectively distinguishes morphologies within a vast amount of radio data. The conversion from 2D images to 1D curves is both straightforward and rapid. The algorithm reduces the data processing complexity from $O(n^2)$ (pixels in two dimensions) to $O(n)$ (pixels in one dimension). Additionally, our classification method requires no prior models, calibrators, or training sets.

2.3.3 Quality check

The majority of sources in all datasets are present in both VLASS epochs (VLASS 1.1/1.2 and VLASS 2.1/2.2, refer to Sec. 2.2). We independently apply the algorithm to these two epochs. We first assign quality flags to the image in each of the epoch. If both epochs result in the same morphological classification, it is considered final. However, in cases of discrepancy, the final classification will be determined by the image of superior quality. The process is as follows:

- We first define a quality flag with a value ranging from 0 (best quality) to 3 (worst quality). Further details are provided below. If one of the epochs has a superior quality flag compared to the other, the morphology from that epoch is considered the final classification. If the quality flags are identical, but the classifications from each epoch remain inconsistent, we proceed to the next step.
- The algorithm examines artifacts in the images, which may result from deficits in the clean algorithm and/or inadequate phase calibration during image production and that can affect the morphological classification (Lacy et al., 2022). We employ a quality flag to assess the impact of artifacts on the image. There are two types of artifacts we pay attention to and that we referred to as 'bright cross' and 'dark pixels':
    1. Bright cross (Fig. 2.3 left): This is a pattern of straight lines, composed of bright pixels (pixel value higher than zs_{up}) traversing the image. It is identified by detecting narrow, low peak signals extending across the image. In the 1D signal, the algorithm counts the number of all peaks with pixel count (height of the 1D signal) less than 2. If the image displays more than 10 low peaks in the row and column directions combined, the quality flag is incremented by 1.

2. Dark pixels (Fig. 2.3 middle): This pattern consists of dark pixels (pixel value lower than zs_{low}) primarily located adjacent to the central bright source. The algorithm detects all pixels with values below zs_{low} in the 1D signal. After visually inspecting several instances of this artifact, we establish that if the sum of all dark pixels exceeds 30% of the sum of all bright pixels, the quality flag is incremented by 2.

If one epoch has a lower-quality flag value, the morphology of that epoch is considered final. In cases where both images have the same quality flag, thus similarly affected by artifacts, we proceed to the following step.

- The algorithm calculates the ratio of the total sum of dark pixels to the total sum of bright pixels. The epoch with the smaller ratio prevails and is chosen as the final classification.

In addition to the aforementioned procedure, we implement an extra check for sources to be classified as *COMPACT* by assessing the dynamic range value. This is because artifacts can mislead the algorithm into incorrectly interpreting them as sidelobes. The dynamic range is a metric to discern the nature of a point source, mitigating the effects of artifact presence. To quantify the dynamic range, we employ the 'peak-to-ring' metric from Gordon et al. 2021 and Lacy et al. 2022. We first calculate the peak flux value within a 2arcsec circle centered on the catalog position of the source, and then measure another peak flux within a 1arcsec wide annulus, where its inner boundary is 7arcsec away from the center (approximately 2 times the beam size for VLASS). We apply this measure to distinguish a core-dominated source when the images are affected by artifacts (when the epoch with the smallest quality flag value is greater than 0). In this case, if in any epoch the 'peak-to-ring' ratio is larger than 2, the source will be classified as a *COMPACT* source. If none of the epochs (including the single-epoch sources) exceeds 2 in the 'peak-to-ring' ratio, the source will be assigned as *VISUAL NEEDED* for further check. The final classification of these sources will be determined and assigned manually by us, following a visual check.

We assign a special category *COMPACT_D* to sources that comply with all the following: (i) a 'peak-to-ring' dynamic range greater than two, (ii) the smallest quality flag between both epochs exceeds one, and (iii) the source was classified as non-*COMPACT* in both VLASS epochs. This implies that the artifacts probably cause the seemingly extended feature. For the sources with only one epoch image available, the source will first be checked if it is detected. It will be classified as a *NON-DETECTION* if its S/N value is below 5.0. The automated classification is final when the quality flag is not larger than one. If the quality flag of the image exceeds one, and the 'peak-to-ring' dynamic range is greater than two, the source will be assigned as *COMPACT_D*. Otherwise, the source will be classified as *VISUAL NEEDED* to be visually classified.

2.4 Result

We apply our morphological classification algorithm to a total of $9,821$ VLASS sources from the WIBRaLS catalog, $4,996$ sources from the KDEBLLACS catalog, and $3,134$ sources from the confirmed blazars in the Roma-BzCAT catalog. A portion of the results for the Roma-BzCAT catalog is presented in Table 2.1. This table includes the name generated by the algorithm in the form of Jhh:mm:ss.ss±dd:mm:ss.ss, coordinates, and the assigned morphological classification. Blazar-like morphologies consist of *COMPACT*, *1-SIDE SEPARATED*, and *1-SIDE EXTENDED* categories. Non-blazar-like morphologies are *2-SIDE SEPARATED* and *2-SIDE EXTENDED*.

In Roma-BzCAT, we conduct a visual inspection of all non-blazar-like sources. In cases where the visual classification differs from the algorithm-based classification, we assign the accurate classification to 'VClass.' We discuss and show VLASS 2 images of all non-blazar-like sources in the Appendix. The tables with the same entries have also been generated for the WIBRaLS and KDEBLLACS catalogs (refer to Table 2.2 for WIBRaLS and Table 2.3 for KDEBLLACS). We do not visually check all non-blazar-like sources in these two catalogs.

No.[a]	Name[b]	R.A.[c]	Decl.[d]	Class[e]	VFlag[f]	VClass[g]	SEpoch[h]
1	J000020.39-322101.00	0.08495833333	-32.35027778	COMPACT_D	0		
2	J000105.29-155106.98	0.2720416667	-15.85193889	COMPACT	0		
3	J000108.62+191434.18	0.2859166667	19.24282778	COMPACT	0		
156	J010838.76+013500.31	17.1615	1.583419444	COMPACT	0		EP02
1185	J100021.79+223318.61	150.0907917	22.55516944	2-SIDE EXTENDED	1		
2566	J174805.82+340401.20	267.02425	34.067	2-SIDE EXTENDED	1	COMPACT	
2677	J193109.60+093717.50	292.7882083*	9.6211944*	OFFSET	1		
2805	J211720.72+050257.58	319.3363333	5.049327778	VISUAL NEEDED	1	COMPACT	
3132	J235846.08+195520.31	359.692	19.92230833	COMPACT_D	0		
3133	J235859.86+392228.30	359.7494167	39.37452778	COMPACT_D	0		
3134	J235933.18+385042.28	359.88825	38.84507778	COMPACT	0		

[a]: Number in the result catalog; [b]: Name of the source; [c]: Right Ascension (J2000); [d]: Declination (J2000); [e]: Morphological classification decided by the algorithm; [f]: Visual Flag, 1 if the source is visually inspected, 0 if not; [g]: Visual classification, assigned by human eyes if the algorithm classification is wrong, this entry is left empty if the source is not visually inspected or the algorithm classification is correct when 'VFlag is 1; [h]: If the source has two epochs available, this column is left empty, otherwise it will denote which epoch of VLASS images is available for the source, EP01: VLASS 1, EP02: VLASS 2;

*: Corrected value by cross-matching with MilliQuas catalog, more details refer to Sec. 2.5.1.

Table 2.1. Sources from the Roma-BzCAT catalog processed and classified using our algorithm. Each source is analyzed based on available radio images from two VLASS epochs, with the algorithm assigning a final morphological classification. Each visually inspected source has a 'VFlag' of 1. If the visual classification ('VClass') does not match the algorithm classification ('Class'), we update 'VClass' to the correct classification. For sources labeled with *VISUAL NEEDED*, their class is determined visually and assigned to 'VClass'. We look into all non-blazar-like sources according to the algorithm in Roma-BzCAT to verify their morphology; more details are in the Appendix. The full table is available online.

No.	Name	R.A.	Decl.	Class	VFlag	VClass	SEpoch
1	J000020.40-322101.24	0.085	-32.35034444	COMPACT_D	0		
2	J000029.08-163620.24	0.1211666667	-16.60562222	COMPACT	0		
3	J000047.05+312028.21	0.1960416667	31.34116944	COMPACT	0		
4	J000101.05+240842.52	0.254375	24.14514444	COMPACT	0		
5	J000105.29-155107.21	0.2720416667	-15.85200278	COMPACT	0		
9817	J235919.53-204756.10	359.831375	-20.79891667	2-SIDE EXTENDED	0		
9818	J235931.80-063943.37	359.8825	-6.662047222	COMPACT	0		
9819	J235935.23+522236.85	359.8967917	52.37690278	COMPACT	0		
9820	J235941.29+392439.47	359.9220417	39.41096389	COMPACT	0		
9821	J235951.04+470709.41	359.9626667	47.11928056	COMPACT	0		

Table 2.2. Same as Tab. 2.1 for WIBRaLS.

No.	Name	R.A.	Decl.	Class	VFlag	VClass	SEpoch
1	J000007.63+420725.51	0.03179166667	42.12375278	NON-DETECTION	0		
2	J000010.29-363405.26	0.042875	-36.56812778	COMPACT	0		
3	J000056.23-082742.05	0.2342916667	-8.461680556	COMPACT	0		
4	J000116.38+293534.59	0.31825	29.59294167	COMPACT	0		
5	J000126.44+733042.60	0.3601666667	73.51183333	COMPACT	0		
4992	J235859.76+431617.64	359.749	43.27156667	COMPACT	0		
4993	J235901.15+171925.84	359.7547917	17.32384444	COMPACT	0		
4994	J235932.16-121022.56	359.884	-12.17293333	COMPACT	0		
4995	J235944.89+054431.34	359.9370417	5.742038889	COMPACT	0		
4996	J235955.31+314559.85	359.9804583	31.766625	COMPACT	0		

Table 2.3. Same as Tab. 2.1 for KDEBLLACS.

Table 2.4 provides a summary of our morphological classification of all sources from the Roma-BzCAT, WIBRaLS, and KDEBLLACS catalogs with corresponding VLASS images. Approximately 95% of sources in the Roma-BzCAT catalog exhibit morphologies consistent with blazars, while 86% of sources in the WIBRaLS catalog and 88% of sources in the KDEBLLACS catalog are similarly consistent with being blazars.

The lower "contamination" rate (i.e., sources unlikely to be blazars) within the Roma-BzCAT catalog is expected, as this curated catalog requires each source to have spectroscopic information to establish its blazar type (BL Lac or FSRQ). However, it is noteworthy that 4.5% of sources (141) are classified as non-blazar-like sources. We visually inspect each source and find that 106 sources indeed show morphologies that are likely not blazars. A closer examination of the multi-wavelength properties of these 106 Roma-BzCAT sources is required to ascertain their actual nature. All sources are shown in the Appendix.

		blazar morphology				non-blazar morphology		
Catalog	TOTAL	COMPACT	COMPACT OFFSET	1-SIDE SEP	1-SIDE EXT	2-SIDE SEP	2-SIDE EXT	NON-DET
Roma-BzCAT	3134	2883 (92.0%)	6 (<1%)	94 (3.0%)	18 (<1%)	26* (<1%)	70* (2.6%)	13 (<1%)
WIBRaLS	9821	7360 (74.9%)	63 (<1%)	930 (9.5%)	64 (<1%)	697 (7.1%)	477 (4.9%)	90 (<1%)
KDEBLLACS	4996	4073 (81.5%)	203 (4.1%)	76 (1.5%)	6 (<1%)	36 (<1%)	3 (<1%)	356 (7.1%)

*: We conduct a visual examination of every non-blazar in Roma-BzCat. The number reported here are the result after visual inspection, ruling out all false classifications. More details refer to Appendix A.

Table 2.4. Statistics of different VLASS morphological classifications for all sources in Roma-BzCAT, WIBRaLS, and KDEBLLACS. We identify four classes as compatible with blazar-like morphologies and two classes as non-blazar morphology. The percentage of non-blazars in WIBRaLS (12%) is higher than in Roma-BzCAT (3%), which is expected given that WIBRaLS consists of candidates, while Roma-BzCAT is a curated catalog. In a test sample of 1000 sources from Roma-BzCAT, the accuracy of the classification is 90.6%.

To evaluate the algorithm's accuracy, we randomly select 1000 sources from the Roma-BzCAT catalogs. We conduct a visual inspection of these 1000 sources and assign a visual morphology classification, following the same naming convention used by our algorithm. By considering the visual inspection classification as the ground truth, the accuracy of the classifier is at the percent of 90.6% for the 1000 sources sample. The classifier makes mistakes by confusing artifacts with actual features in the morphology. These artifacts, as shown in Fig. 2.3, have signals that resemble the real radio signals emitted by the source.

2.5 Discussion

2.5.1 Misidentifications on OFFSET sources

OFFSET sources are present in all three catalogs of our dataset. This class of sources is characterized by the absence of radio emission at the catalog position. Instead, radio emission is observed with an offset ($5 - 10$ arcsec) from the position registered in the catalog. For *OFFSET* sources in Roma-BzCAT, it is important to note that the spectroscopic information for the central source has already been obtained, allowing for the determination of a specific blazar type (Massaro et al., 2009).

For the six *OFFSET* sources in the Roma-BzCAT catalog, we examine their available archival data. Four of the six sources show real offset (shown in Fig. 2.4); the other two sources show no actual offset in their VLASS images and the optical counterpart is at the exact position of the radio source. Thus, they are classified as *COMPACT* sources instead. We perform crossmatching to the MilliQuas catalog (Flesch, 2021) within a range of 5–10$''$ and discover that all four sources were mispositioned in the Roma-BzCAT catalog; instead, all four sources have previous information on the precise position of their counterparts in X-ray or other wavelengths. The positions reported in the literature align with the actual VLASS radio source and there is no offset in their optical counterpart as well. Here, we provide information of the optical counterparts information for the four *OFFSET* sources:

J193109.60+093717.50: The optical position is provided in Motch et al. (1998). They carried out the observation at Observatoire de Haute-Provence, CNRS, France, to acquire the optical position and also identify a featureless spectrum to confirm its BL Lac nature.

J205243.03+081037.48: It is included in a spectroscopic compaign done by Piranomonte et al. (2007). They observe this source with the 3.6m Telescopio Nazionale Galileo (TNG). The optical position is determined and its spectrum also shows the absence of emission or absorption features, a BL Lac characteristic.

J230635.50-110349.28 and *J232352.50+421054.98*: Their positions are recorded in Bauer et al. (2000). They carry out cross-identifications to match NVSS sources to bright X–ray sources and provide the coordinates of the closest matches. *J232352.50+421054.98* was classified as a BL Lac object based on its archival spectrum.

We inspect all coordinates above and confirm that they are located on the center of radio sources in VLASS images. We have updated the positions of these mispositioned sources in the Roma-BzCAT catalog and included them in our output catalog for accurate reference (see Tab. 2.1 for an example).

2.5.2 Testing the algorithm on the MOJAVE blazars

The MOJAVE survey focuses on obtaining high-resolution images of AGN radio jets using VLBA observations, providing detailed images at the parsec level. We ran our VLASS classifier algorithm in 320

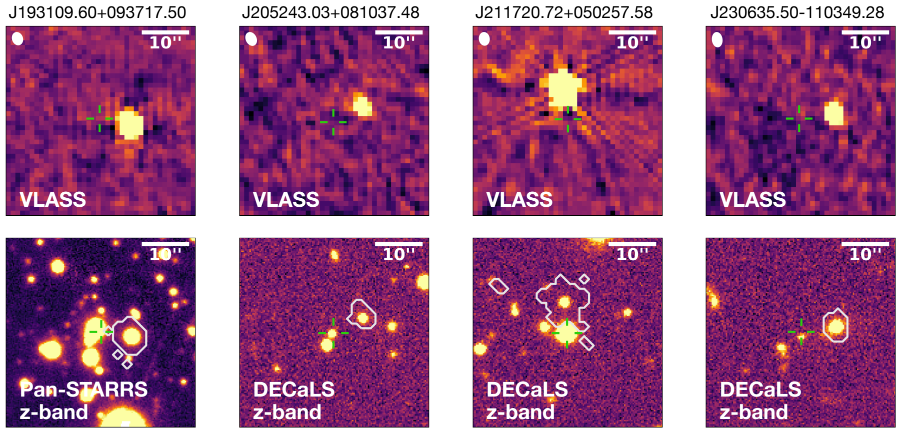

Figure 2.4. *OFFSET* sources from Roma-BzCAT, four in total. These sources are classified based on the discrepancy between the catalog position and the position of the radio source. The green cross represents the source position recorded in Roma-BzCAT. The radio image (upper row) demonstrates that the radio-emitting source is not located at the catalog position but has an offset of more than 5″. In the optical z-band image (lower row), a separate radio-silent source is found at the catalog position. This mismatch is a position error in Roma-BzCAT and we provide the accurate coordinates in our result.

MOJAVE sources that are identified as blazars (Lister et al., 2021). The result is that 298 are classified to have blazar-like morphology. The VLASS images of the 22 non-blaza-like sources (*2-SIDE EXTENDED* or *2-SIDE SEPARATED*)are shown in Fig. 3.7. Out of those, 11 are still consistent with being compact sources, according to our visual inspection, resulting in 11 MOJAVE blazars with extended VLASS morphology. Our full classification for all 320 MOJAVE blazars is presented in an accompanying on-line table.

There are a few cases in which the MOJAVE blazars are known to display extended emission surrounding their compact core. For example, TXS 0716+714 (Antonucci et al., 1986; Wagner et al., 1996), PKS 1045–18 and PKS 1036+054 (see Fig. 2 in Kharb et al. 2010). In these three examples, our algorithm classifies the sources as *COMPACT_D*. This means that some *COMPACT_D* sources might actually be extended (see Sec. 2.3.3), but still core-dominated.

We find that 15 out of 320 MOJAVE sources are classified under *COMPACT_D*, including the examples above. However, without the knowledge of additional radio images of higher resolution or at different frequencies, we can not differentiate if the extended morphology is real or introduced by artifacts.

In summary, MOJAVE blazars can display extended structures at both the submilliarcsecond-scale in VLBA images and the kiloparsec-scale in VLA 1.4 GHz images. However, in most cases, these extended features are not discernible in the frequency and sensitivity of VLASS 3 GHz images due to low resolution or sensitivity. As a result, most sources are categorized as *COMPACT* objects, in line with their blazar characteristics (but see the Appendix for discussion and images of MOJAVE sources classified as non-COMPACT).

No.	Name	R.A.	Decl.	Class	VFlag	VClass	SEpoch
1	S4 0003+38	1.48823	38.33754	COMPACT	0		
2	NRAO 005	1.55789	-6.39315	COMPACT	0		
3	CRATES J0009+0628	2.26638	6.47257	COMPACT	0		
4	III Zw 2	2.62919	10.97486	COMPACT	0		
5	4C +40.01	3.37971	40.86032	2-SIDE EXTENDED	1		
405	1ES 2344+514	356.77015	51.70497	COMPACT	0		
406	PKS 2345-16	357.01087	-16.52001	COMPACT_D	0		
407	4C +45.51	358.59033	45.88451	COMPACT	0		
408	S5 2353+81	359.09497	81.88118	COMPACT	0		
409	PKS 2356+196	359.69202	19.92231	COMPACT	0		

Table 2.5. Same as Tab. 2.1 for MOJAVE sources.

3

Chapter 3

3.1 MOJAVE

3.1.1 Morphology of MOJAVE Blazars

In this section, we present VLASS2 images of all Roma-BzCAT sources that our algorithm classified as *2-SIDE SEPARATED* or *2-SIDE EXTENDED*, classifications which suggest these sources may not be typical blazars.

The classifications include 36 sources labeled as *2-SIDE SEPARATED* and 105 sources labeled as *2-SIDE EXTENDED*. Each of these sources underwent visual inspection. For any source where visual inspection led to a reclassification, we marked it with a visual flag value of 1 and updated its classification in the online results table. In Figs. 3.1-3.6, we mark sources with revised classifications (indicated by VClass in the results table) with a star on their respective images.

In Fig. 3.7, we show the 22 VLASS2 images of MOJAVE sources (see Section 2.5.2) that our algorithm classified as having non-blazar-like morphology. Of these, 11 are consistent with a *COMPACT* morphology upon visual inspection (these are marked with stars in Fig. 3.7).

The remaining 11 sources still exhibit non-blazar-like morphology, yet are likely true blazars. This assessment is based on their documented apparent superluminal motions in the MOJAVE database (Lister et al., 2019), suggesting jet orientation at a small inclination relative to the line of sight. This finding highlights that while extended morphology may raise questions about the blazar classification, it is not conclusive. Other blazar characteristics must also be considered for a comprehensive classification.

3.2 A testing case

3.2.1 Is J0643–3314 (likely) a blazar?

Identifying a large sample of blazars are critical to understand their relativistic jets. D'Abrusco et al. 2019 produced a catalog of nearly 18,000 blazar candidates based on their infrared colors from Wide-Field Infrared Survey Explorer (WISE, Wright et al. 2010) that are similar to already identified blazars. In an effort to scrutinize their nature, we design an automatic algorithm to reclassify blazar candidates into likely blazars or likely non-blazars based on their radio morphology provided by VLASS (Lacy et al., 2020; Gordon et al., 2021), which provides $2.5''$ angular resolution images at 3 GHz (details refer to Xie et al. 2024). To validate our evaluation, we study one blazar candidate J0643–3314 from the catalogue of D'Abrusco et al. 2014. It is classified as a likely non-blazar according to Xie et al. 2024, and we conduct follow-up spectroscopy to understand its nature.

Radio detections

The VLASS radio image displays clear symmetric two-sided radio jets and is thus classified as a likely non-blazar (see Fig. 3.8). To be included in D'Abrusco et al. 2014, J0643–3314 has been inspected for

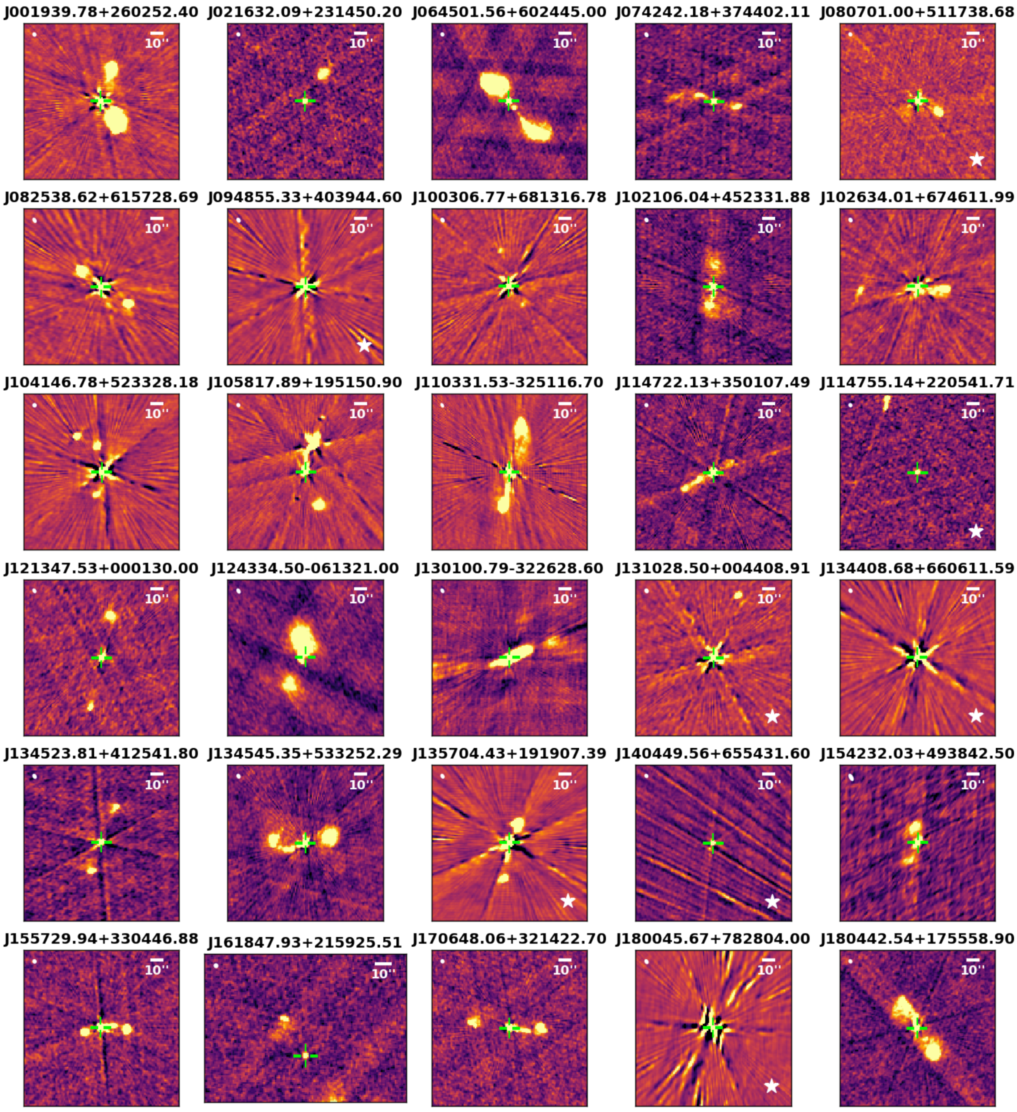

Figure 3.1. All *2-SIDE SEPARATED* sources with their VLASS2 image in Roma-BzCAT. Each source has undergone visual inspection, and any discrepancies found during this process are indicated by a visual flag in the resulting table. For each of these sources, our revised visual classification is provided. These revised sources are marked with a white star on their image.

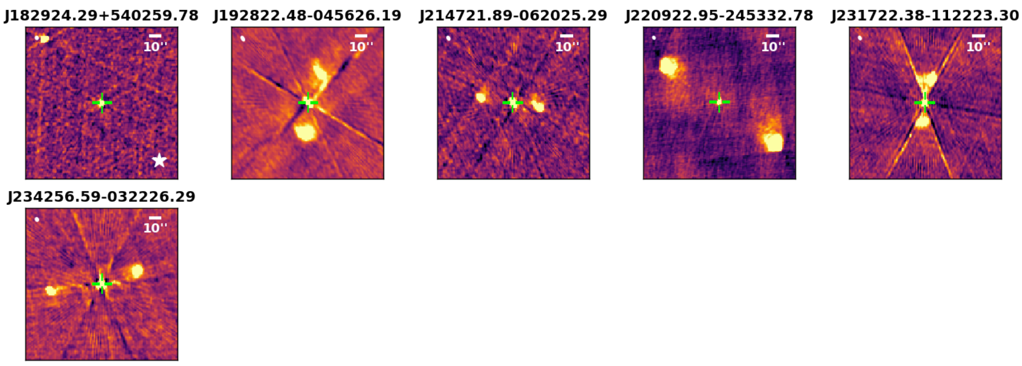

Figure 3.2. Continued for Fig. 3.1.

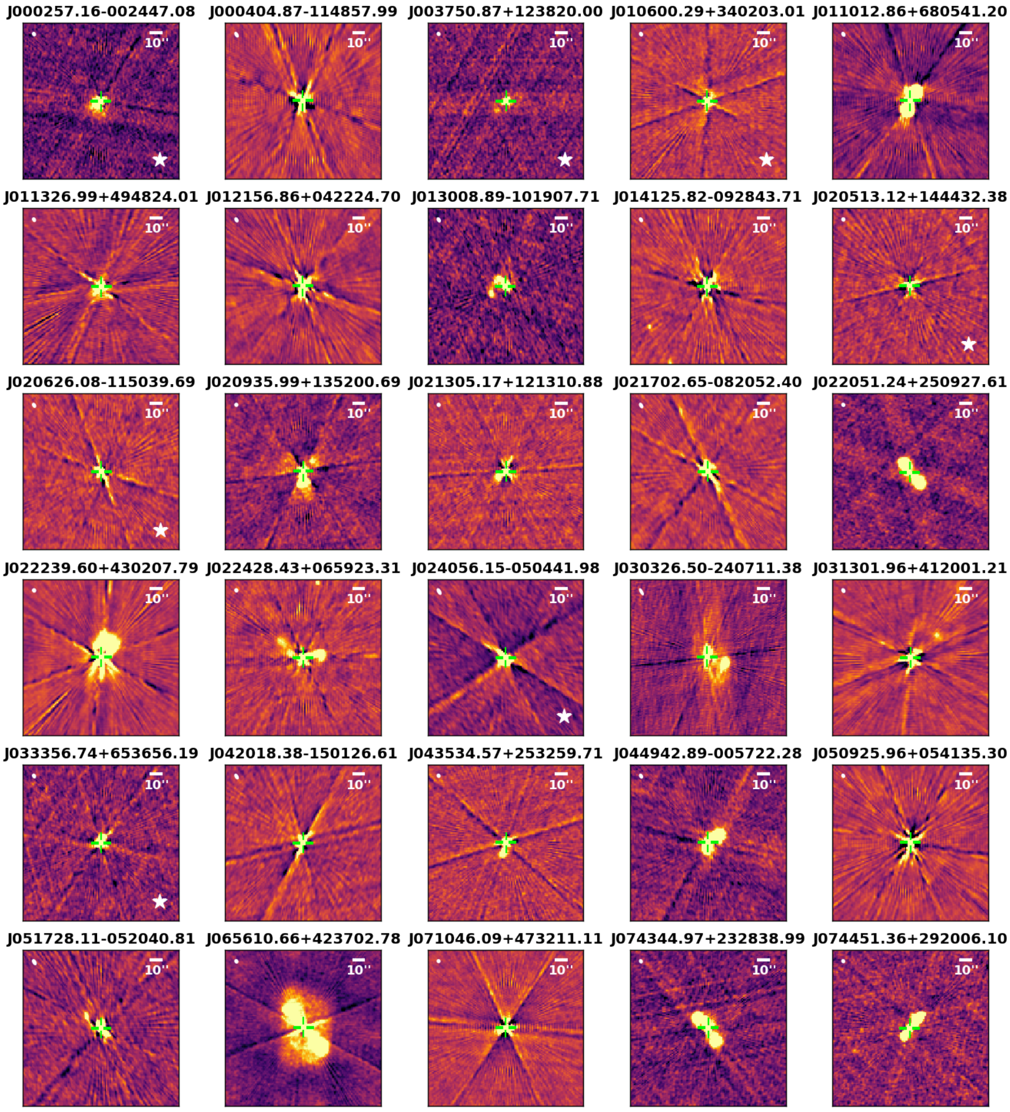

Figure 3.3. Same as Fig. 3.1 for *2-SIDE EXTENDED* sources in Roma-BzCAT.

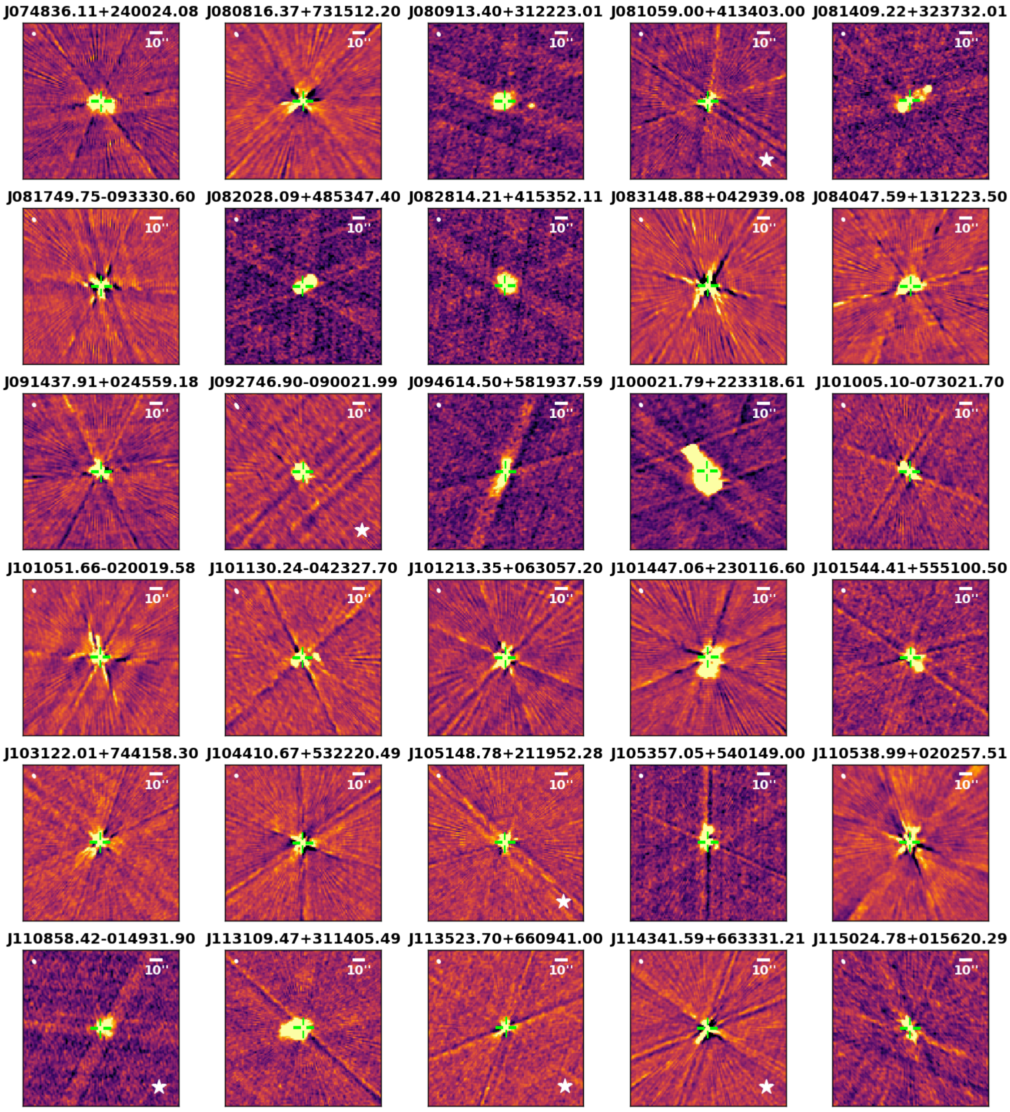

Figure 3.4. Continued for Fig. 3.3.

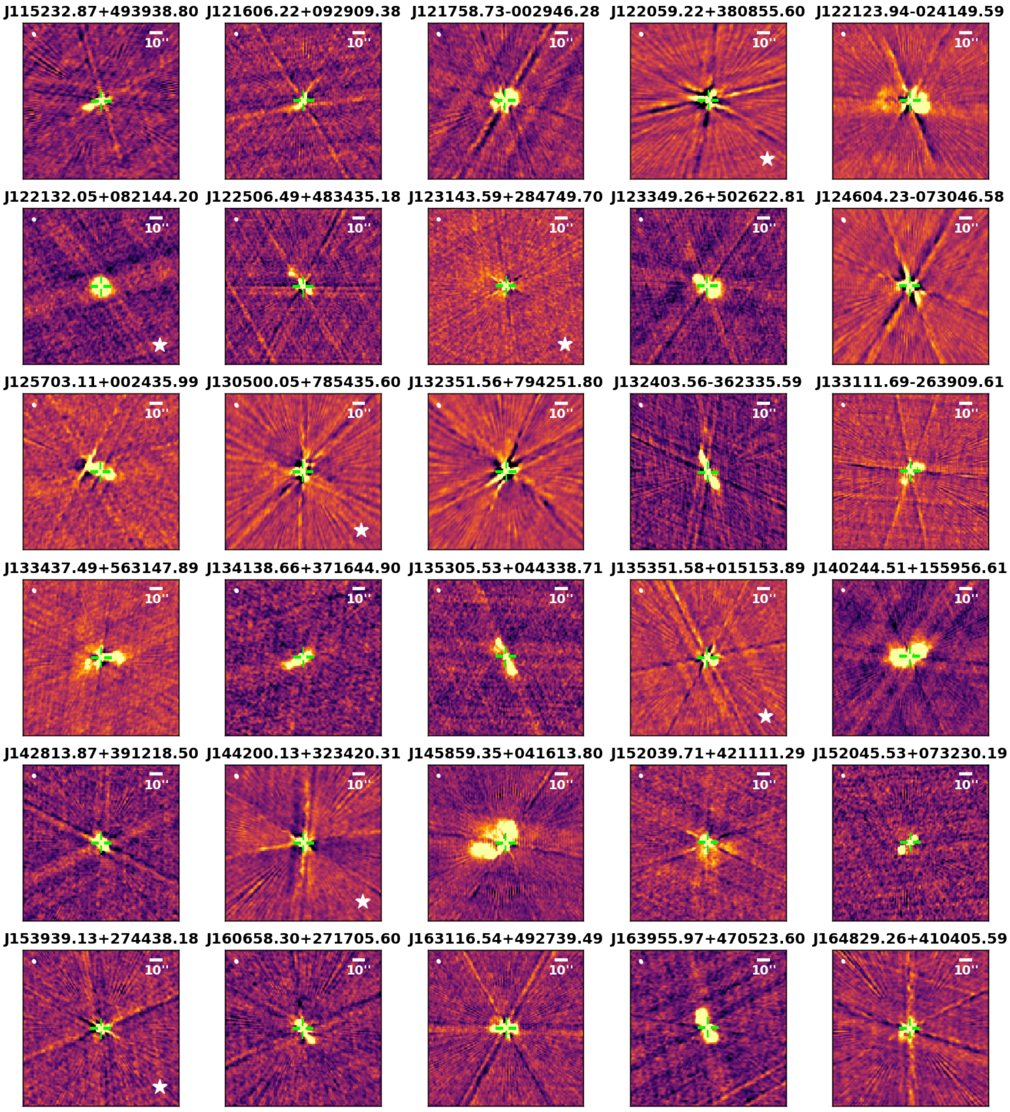

Figure 3.5. Continued for Fig. 3.4.

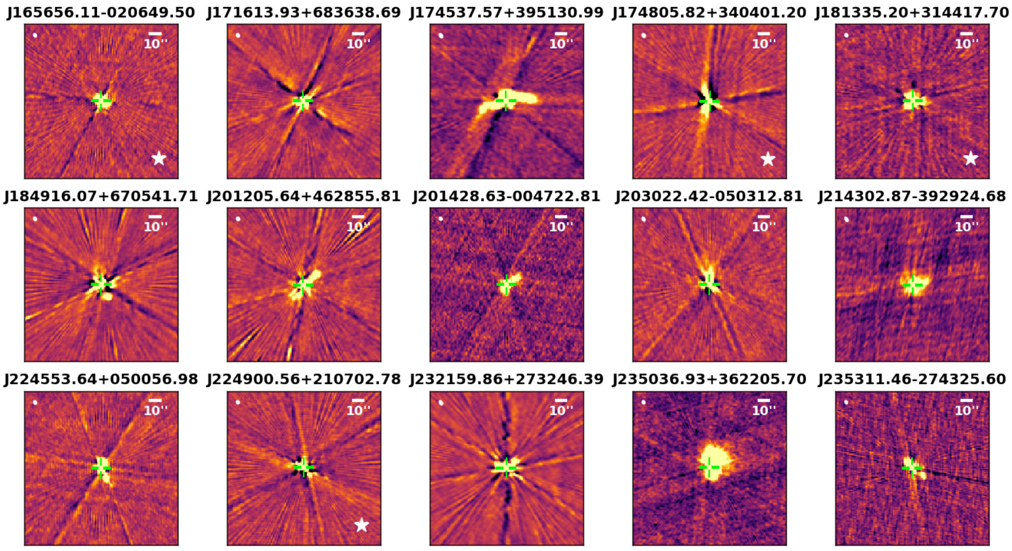

Figure 3.6. Continued for Fig. 3.5.

radio images in NRAO VLA 70 Sky Survey (NVSS, Condon et al. 1998) and Sydney University Molonglo Sky Survey (SUMSS, Mauch et al. 2008). At the resolution of both radio surveys (45″ for NVSS and SUMSS), the radio structure of J0643–3314 remains unresolved, exhibiting a compact morphology.

We first determine whether J0643–3314 is consistent with a flat spectrum radio quasar (FSRQ). Combining the data from The Australia Telescope 20 GHz Survey (AT20G, Murphy et al. 2010) and TIFR GMRT Sky Survey (TGSS, Intema et al. 2017), the radio spectrum of J0643–3314 is not flat, as illustrated in Fig. 3.9, which rules out the possibility of it being a FSRQ.

Spectroscopy and black hole properties

Another possibility for this source to still be considered a blazar is if the optical spectrum displays no prominent broad lines, i.e., a BL Lac object, as some BL Lacs show non-flat radio spectrum (see e.g., Cavallotti et al. 2004). We conduct spectroscopic follow-up of J0643–3314 using the FOcal Reducer/low dispersion Spectrograph 2 (FORS2, Appenzeller et al. 1998) at the Very Large Telescope (VLT). We reduce 1D spectrum using `PypeIt` (Prochaska et al., 2020). The FORS2 spectrum is displayed in Fig. 3.10. The prominent broad emission lines, in combination with the radio spectrum and the two-sided jets in the VLASS image, provide strong evidence against J0643–3314 being a BL Lac object, thus not a blazar.

We use the FORS2 spectrum to determine the black hole properties of J0643–3314. The spectrum is analyzed using `Sculptor` (Schindler, 2022). The resulting FWHM of the broad component is 4897±7 km s^{-1} for Hα and 5577±142 km s^{-1} for Hβ. We estimate the systemic redshift of J0643–3314 to be $z = 0.3004 \pm 0.0001$, derived from the narrow components of the Hβ and [OIII]. At this redshift, the physical size of the jet in the VLASS image is 100.4 kpc (Fig. 3.8), adopting the cosmology of H_0=70 km s^{-1} Mpc^{-1}, Ω_M=0.3, and Ω_Λ=0.7.

To estimate the black hole mass, we adopt the relationship outlined in Vestergaard & Peterson (2006) for Hβ as follows:

$$\log M_{\rm BH}({\rm H}\beta) = \log \left[\left(\frac{{\rm FWHM(H}\beta)}{1000\,{\rm km\,s^{-1}}} \right)^2 \left(\frac{\lambda L_\lambda(5100{\rm \AA})}{10^{44}\,{\rm erg\,s^{-1}}} \right)^{0.50} \right] + K \tag{3.1}$$

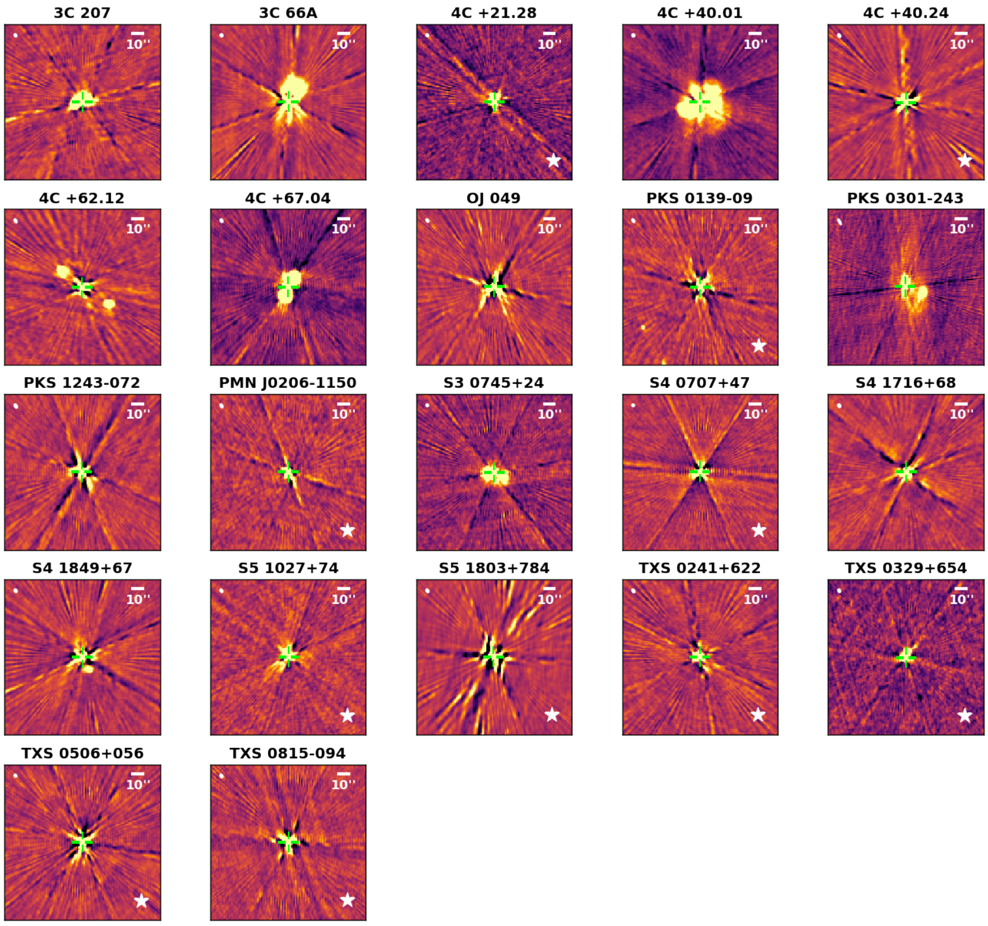

Figure 3.7. VLASS2 images for 22 MOJAVE blazars classified as likely non-blazars. Each source has undergone visual inspection, and any discrepancies (are *COMPACT* instead of non-*COMPACT*) found during this process are indicated by a visual flag in the resulting table. For each of these sources, our revised visual classification is provided. These revised sources are marked with a white star on their image.

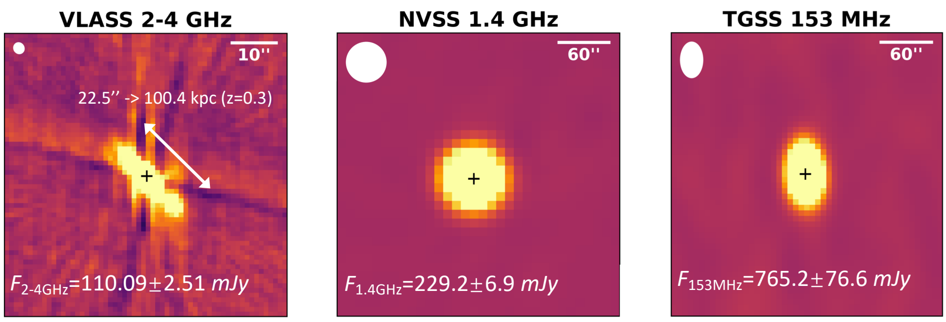

Figure 3.8. Radio images of sky surveys, from left to right: VLASS 3 GHz, NVSS 1.4 GHz, and TGSS 153 MHz, of the blazar candidate J0643–3314. The VLASS images makes it unlikely to be a blazar (see Xie et al. 2024 for details), since it shows a symmetrical morphological feature.

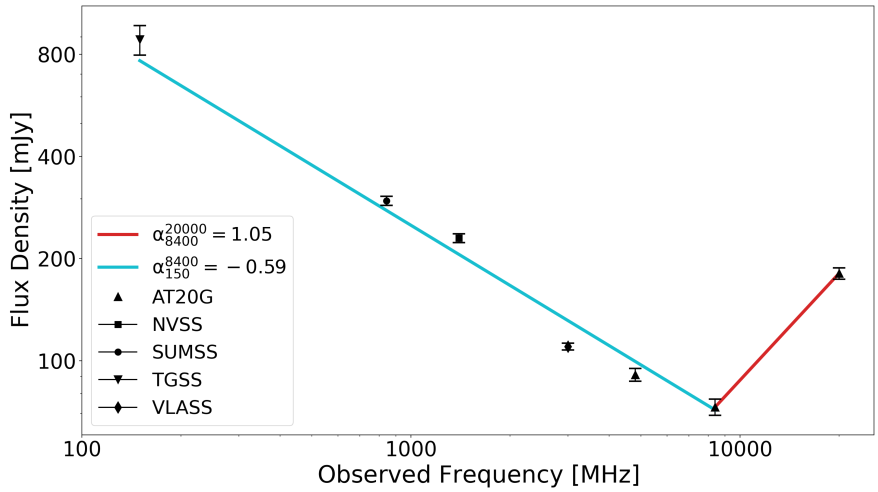

Figure 3.9. Radio spectrum of J0643–3314, flux densities collected from radio surveys. The unflat radio spectrum shown here rules out the FSRQ interpretation.

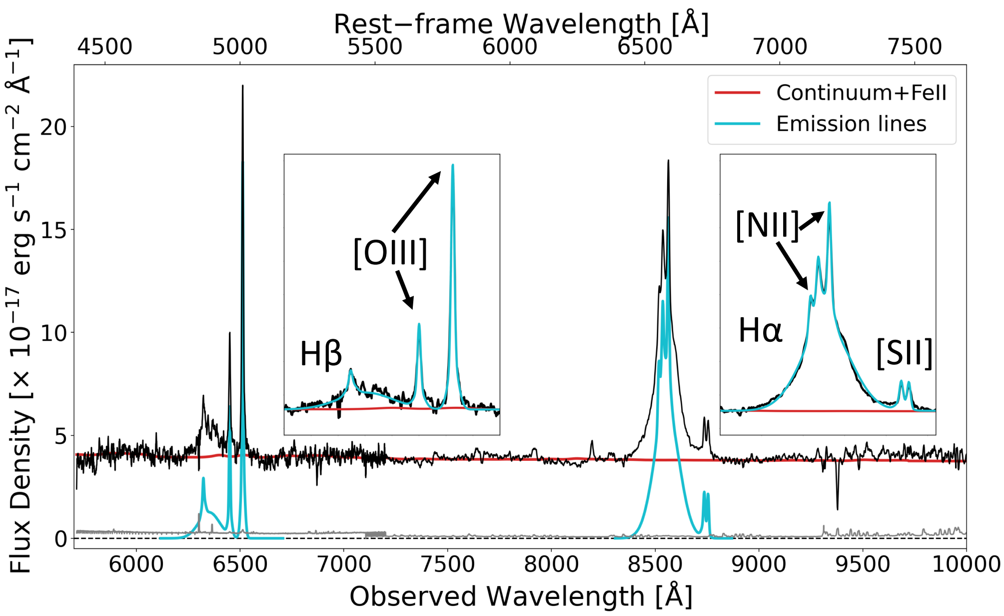

Figure 3.10. FORS2 1D spectrum of J0643–3314. The red solid line represents the continuum combined with the FeII continuum flux, the blue lines show the emission line models subtracted from the continuum. The presence of broad emission lines confirms that J0643–3314 is not a BL Lac object.

where L_λ is the optical luminosity at 5100Å, estimated as $1.45 \pm 0.13 \times 10^{40}\,\mathrm{erg\,s^{-1}\,Å^{-1}}$ the constant K is 6.91 ± 0.02.

Hβ is on average broader than Hα reported by Greene & Ho (2005), following this relation:

$$\mathrm{FWHM_{H\beta}} = (1.07 \pm 0.07) \times 10^3 \left(\frac{\mathrm{FWHM_{H\alpha}}}{10^3\mathrm{km\,s^{-1}}} \right)^{(1.03\pm0.03)} \mathrm{km\,s^{-1}} \tag{3.2}$$

We measure the black hole mass with the FWHM of Hβ and Hα using the relation reported in Eq. 3.1 and substituting Eq. 3.2 into Eq. 3.1, we derive the following values for the black hole masses: 2.17±0.09 $\times\,10^8\,\mathrm{M_\odot}$ (Hβ), 2.36±0.10 $\times\,10^8\,\mathrm{M_\odot}$ (Hα). The bolometric luminosity is estimated using the equation from Runnoe et al. (2012):

$$\log L_{bol} = (1.02 \pm 0.001)\log(\lambda L_{5100\text{Å}}) - (0.09 \pm 0.03) s_{\lambda,opt} \tag{3.3}$$

where $L_{5100\text{Å}}$ is the monochromatic luminosity at rest-frame wavelength 5100 Å, and $s_{\lambda,opt}$ is the slope of the power law model, where in our spectrum $s = 0.08 \pm 0.05$. The calculated bolometric luminosity of J0643–3314 is 5.57±0.03 $\times\,10^{44}\,\mathrm{erg\,s^{-1}}$.

The Eddington luminosity for pure ionized hydrogen is $L_{\mathrm{Edd}} = 1.3 \times 10^{38}\,\frac{M_{BH}}{M_\odot}\,\mathrm{erg\,s^{-1}}$. The Eddington ratio is $\lambda_{Edd} = \frac{L_{\mathrm{bol}}}{L_{\mathrm{Edd}}}$ = 0.02±0.01 (for both Hα and Hβ).

II

Second part

4

Chapter 4

4.1 Background

Quasars in the early universe are found to be unusually massive given the short time available for black hole growth after the Big Bang. While several scenarios have been proposed to explain the origins of these supermassive black holes (SMBHs), these theories require either initial black holes more massive than current predictions, or accretion at sustained rates close to, or even exceeding, the Eddington limit.

Quasars with black hole masses over $10^9 M_\odot$ have been observed at $z > 6$, just a few hundred million years after the Big Bang (see e.g., Wu et al., 2015; Bañados et al., 2018b; Yang et al., 2020). Traditional Eddington-limited accretion models struggle to explain such massive black holes in this short period. High-redshift quasars impose further constraints on growth models, with those at $z > 7$ providing key insights into seed mass and accretion efficiency (Inayoshi et al., 2020).

To identify fast-accreting quasars, we will focus on the most distant radio-loud quasars. The presence of jets in radio-loud quasars is expected to aid their accretion, as jets can enhance SMBH growth by efficiently transporting angular momentum and increasing the accretion rate (Kuncic & Bicknell, 2004). A jetted AGN will accrete more rapidly than its non-jetted counterpart at the same luminosity (Kuncic & Bicknell 2004, 2007a,b; Jolley & Kuncic 2008). Moreover, radio-loud quasars have been observed accreting near the Eddington limit even up to $z \sim 7$ (see e.g., Bañados et al., 2021).

However, radio-loud quasars are rare at this early epoch. The radio-loud quasars fraction (RLF) is typically around 10-20% at low redshifts (Kellermann et al., 1989; Ivezić et al., 2002), but this fraction may decrease at higher redshifts. For example, Bañados et al. 2015 measured the RLF at $z > 5$ to be $8.1^{+5.0}_{-3.2}\%$, while Keller et al. 2024 estimated it at $3.8^{+6.2}_{-2.4}\%$ for $z > 6$. With the discovery of more high-redshift quasars from upcoming surveys such as Euclid, we expect further advances in constraining black hole formation and growth models in the early universe (Euclid Collaboration et al., 2019, 2022, 2024).

Radio-loud (RL) and radio-quiet (RQ) quasars exhibit notable differences in their black hole properties, as discussed in Sec. 1.5.3. A key area of debate is the relationship between radio-loudness and black hole mass. Several studies suggest that RL quasars are associated with more massive black holes than their RQ counterparts. For example, Laor (2000) found that RL quasars predominantly host black holes with $M_{\mathrm{BH}} \gtrsim 10^9 M_\odot$, whereas RQ quasars exhibit a broader mass range. This disparity has been interpreted as evidence that more massive black holes may be necessary to sustain powerful relativistic jets (Sikora et al., 2007).

Contrasting this, Ho (2002) observed a more scattered relationship, indicating that factors other than black hole mass may influence radio-loudness. One such factor is the Eddington ratio, λ_{Edd}. Studies have reported an anti-correlation between radio-loudness and λ_{Edd}, suggesting that RL quasars might accrete less efficiently than RQ quasars (Ho, 2002; Sikora et al., 2007). This supports the hypothesis that the accretion mode, whether radiatively efficient or inefficientplays a crucial role in shaping a quasar's radio properties (Best & Heckman, 2012).

Further complicating the RL–RQ distinction, Gürkan et al. (2019) proposed that quasar radio properties form a continuum rather than a strict dichotomy, noting that some RQ quasars can also host jets (see, e.g., Sbarrato et al. 2021). Jets themselves may enhance accretion efficiency through mechanisms such as radiative efficiency trapping (Sadowski & Narayan, 2016). In this process, intense outflows or jets suppress central accretion while facilitating significant inflows in outer regions. This phenomenon could contribute to the rapid growth of supermassive black holes (SMBHs) in the early universe (Takeo et al., 2020).

The identification and study of AGN jets in high-redshift quasars are essential for understanding feedback mechanisms in the early universe. Jets can expel gas from host galaxies and regulate star formation (Fabian, 2012; Harrison et al., 2018). Observations of extended radio structures around high-redshift quasars suggest their potential impact on galaxy evolution during this formative period (Momjian et al., 2018). In this context, we aim to expand our understanding by investigating four specific $z > 5.5$ quasars with detected radio emissions. Our spectroscopic data allow for a detailed analysis of their black hole properties, contributing to the broader effort of measuring black hole masses in this rare population. In the following paragraphs, we introduce their discoveries and published properties. We summarize the quasars in our sample and their key characteristics in Tab. 4.1, with further details about the data discussed in Sec. 4.2.

P215-16 was first discovered as the earliest high-z quasar identified with PS1 by Morganson et al. 2012, where the discovery spectrum was also presented. The location of the target was later refined using improved stacked photometric data in Bañados et al. 2014. The redshift of $z = 5.783$ was accurately measured using the CO(9–8) line, as reported by Li et al. 2024, observed with the Northern Extended Millimetre Array (NOEMA). The CO(9–8) and [CII] emission lines are particularly reliable for determining the redshifts of high-redshift quasars, as they are bright, detectable in the radio/submillimeter regime once redshifted, and originate in the interstellar medium of the host galaxy. These lines provide an unbiased cosmological redshift unaffected by quasar outflows. Our work provides the first radio information for P215-16, establishing its radio-loud nature. Additionally, the rest-frame UV spectrum, covering the broad emission lines, is presented here for the first time.

P352-15 was initially discovered by Bañados et al. 2018a through the PS1 survey. It was identified as the most extreme radio-loud quasar with $R > 1000$, based on VLA 3 GHz data reported in the same study. The discovery spectrum, taken with the Low-Dispersion Survey Spectrograph (LDSS3) at the Magellan Clay telescope in Las Campanas Observatory, was also included in their work. The redshift was initially determined to be $z = 5.84$ using a template fit to the Ly-α emission. Later, the Very Long Baseline Array (VLBA) at 1.54 GHz resolved the source into a compact/one-sided morphology (Momjian et al., 2018). The redshift was refined to $z = 5.832$ using the [CII] line, as reported by Rojas-Ruiz et al. 2021, who also recalculated the radio-loudness to $R \sim 1000$. Our work presents, for the first time, the NIR spectrum of this quasar, covering the CIV line, to measure its black hole properties and refine the radio-loudness R using a broader set of archival radio survey data.

J2318-3113 was discovered through the VISTA Kilo-degree Infrared Galaxy Survey (VIKING, Edge et al. 2013). Its redshift was calculated to be $z = 6.442$ using the [CII] line observed with ALMA (Decarli et al., 2018). Ighina et al. 2021 established the radio-loud nature of this source, calculating its radio-loudness to be $R \sim 70$ using data from several radio surveys. For the first time, we present the black hole properties of this quasar, derived from its rest-frame UV spectrum, and update its radio-loudness R using follow-up VLA 3 GHz observations.

J0410-0139 was reported by Banados et al. 2024b as the most distant radio-loud quasar currently known, at $z = 6.996$. It is also identified as a blazar. The redshift was measured from follow-up

	P215–16	P352–15	J2318–3113	J0410–0139
R.A.	$14^{\mathrm{h}}20^{\mathrm{m}}36\overset{\mathrm{s}}{.}98$	$23^{\mathrm{h}}29^{\mathrm{m}}36\overset{\mathrm{s}}{.}84$	$23^{\mathrm{h}}18^{\mathrm{m}}18\overset{\mathrm{s}}{.}35$	$04^{\mathrm{h}}10^{\mathrm{m}}09\overset{\mathrm{s}}{.}05$
Dec.	$-16°02'30\overset{''}{.}25$	$-15°20'14\overset{''}{.}46$	$-31°13'46\overset{''}{.}34$	$-01°39'19\overset{''}{.}88$
Redshift	5.783 (CO)	5.832 ([CII])	6.442 ([CII])	6.996 ([CII])
Redshift Ref.	[1]	[2]	[3]	[4]

Table 4.1. The positions and redshifts of the black holes for each quasar in our sample, along with redshift references, are provided in this table. Additional detailed data used in this work for measuring black hole properties and calculating radio-loudness are presented in Sec. 4.2.
References: [1]: Li et al. 2024; [2]: Rojas-Ruiz et al. 2021; [3]: Decarli et al. 2018; [4]:Banados et al. 2024a

observations, where the [CII] line measurement was reported (Banados et al., 2024a). The same study also presented the rest-frame UV spectrum. Comprehensive radio survey data, including VLA follow-up observations, were used to confirm its radio-loud nature, with a calculated radio-loudness of $R \sim 100$. This work presents the rest-frame UV and black hole properties on this source.

4.2 Data

In this section, we present the photometric and spectroscopic data for four selected radio-detected quasars. To investigate the physical properties of the black holes, we include new spectroscopic data in the rest-frame UV, allowing us to analyze the black hole properties through the broad emission lines of MgII and CIV and photometric data to calibrate the flux density in the spectra.

4.2.1 Photometric Data

We acquire photometric data to calibrate the spectra of the selected quasars, ensuring accurate flux density calibrations for the subsequent spectroscopic analysis. The photometric measurements are sourced from various surveys, including data from Ross & Cross 2020, which utilized the Wide Field Camera (WFCAM) on the United Kingdom Infrared Telescope (UKIRT, Casali et al. 2007) and the VISTA Infrared Camera (VIRCAM) on the Visible and Infrared Survey Telescope for Astronomy (VISTA, Sutherland et al. 2015). Additionally, new photometric measurements were obtained from New Technology Telescope (NTT, Dhillon et al. 2007) as part of this study. Detailed photometric measurements for each source are provided in Tab. 4.2.

4.2.2 Spectroscopic Observations

We gather spectroscopic data from multiple observatories, utilizing different instruments for each quasar. The spectroscopic observations are conducted using the following telescopes and instruments:

- VLT/X-Shooter (Vernet et al., 2011), covering 0.3–2.5 μm at $R_{\rm spec} \sim 5600-8800$ for high-resolution NIR observations and slightly lower resolution in visible range.
- Gemini/Gemini Near-Infrared Spectrograph (GNIRS, Elias et al. 1998), covering 0.9–2.5 μm at $R_{\rm spec} \sim 1000$.
- Magellan/Folded-port Infrared Echellete (FIRE, Simcoe et al. 2013), covering covering 0.8–2.5 μm at $R_{\rm spec} \sim 6000$.

- Keck/NIRES (Wilson et al., 2004), covering 0.8–2.4 μm at $R_{\rm spec} \sim 2700$.
- LBT/LUCI (Buschkamp et al., 2012), covering 0.8–2.4 μm at $R_{\rm spec} \sim 2000$.

The exposure details of these observations are summarized in Tab. 4.3.

All spectroscopic data in this work are reduced using the Python Spectroscopic Data Reduction Pipeline (`PypeIt`, Prochaska et al. 2020). The general data reduction process for each near-infrared (NIR) spectrum is summarized as follows:

1. **Sky Background Subtraction:** The sky background is subtracted from the 2D spectra by taking the difference between ABBA dithered exposures, effectively removing sky emission lines and other background signals.
2. **Calibration:** Calibration steps, including wavelength calibration, flat-fielding, and slit corrections, are applied to all exposures to ensure accurate spectral measurements.
3. **Object Extraction:** The objects, appearing as positive traces in the 2D spectra, are identified and extracted into 1D spectra using optimal extraction techniques to maximize signal-to-noise (S/R) ratio.
4. **Flux Calibration:** Flux calibration is performed for each object using standard stars observed under the same conditions. This step ensures that the spectra accurately represent the flux densities of the targets.
5. **Stacking:** The 1D spectra of the target objects are stacked to improve the S/R ratio. The stacking process also corrects for shifts in wavelength calibration and ensures alignment across exposures.
6. **Telluric Correction:** A telluric model is fitted to the spectrum to correct for variations in NIR sensitivity due to atmospheric absorption, particularly in regions affected by water vapor and other atmospheric constituents.

This reduction process ensures the highest quality spectra for subsequent analyses.

For sources with VLT/X-Shooter data, we processed the X-Shooter data separately for its visual (VIS) and near-infrared (NIR) arms. These are merged as follows:

1. Overlapping regions are combined using the data from the arm with the lower noise to optimize the S/N ratio.
2. Regions with excessive noise (signal exceeded by noise) were masked out.
3. In non-overlapping areas, the respective data from each arm were retained and merged. The merging process included: (i) fitting a power law to each spectrum (NIR and VIS) individually, (ii) fixing the power law slope from the NIR spectrum, (iii) refitting the VIS spectrum with this fixed slope of NIR to extract the power law amplitude at 2500Å, and (iv) applying a scaling factor to match the VIS spectrum to the NIR spectrum.
4. The final combined spectrum was renormalized using photometric measurements to ensure consistency across the full wavelength range.

When data from multiple instruments are available, we combine the spectra to enhance the overall S/R ratio. The steps for combination are as follows:

Object	Date	Telescope/Instrument	Magnitudes(AB)
P215–16		UKIRT/WFCAM	$J_{\rm SOFI}$=18.82±0.03
		UKIRT/WFCAM	$H_{\rm SOFI}$=18.68±0.04
		UKIRT/WFCAM	$Ks_{\rm SOFI}$=18.63±0.06
P352–15	2017 September 25	Magellan/FourStar	$J_{\rm FourStar}$=21.14±0.14
	2021 July 28	NTT/SOFI	$J_{\rm SOFI}$=21.14±0.14
	2021 July 28	NTT/SOFI	$Ks_{\rm SOFI}$=20.60±0.12
J2318–3113	2021 July 27	NTT/SOFI	$J_{\rm SOFI}$=20.66±0.04
	2021 July 27	NTT/SOFI	$H_{\rm SOFI}$=20.44±0.07
	2021 July 27	NTT/SOFI	$Ks_{\rm SOFI}$=20.47±0.11
J0410–0139	2020 November 20	NTT/SOFI	$J_{\rm SOFI}$=20.75±0.07
	2021 July 26	NTT/SOFI	$J_{\rm SOFI}$=20.97±0.12
	2023 January 04	NTT/SOFI	$J_{\rm SOFI}$=20.77±0.07
	2020 November 20	NTT/SOFI	$H_{\rm SOFI}$=20.85±0.13
	2023 January 04	NTT/SOFI	$H_{\rm SOFI}$=20.88±0.07
	2020 November 20	NTT/SOFI	$Ks_{\rm SOFI}$=20.30±0.08
	2023 January 04	NTT/SOFI	$Ks_{\rm SOFI}$=20.38±0.10

Table 4.2. The date, instruments, and magnitudes in AB magnitudes for the photometric observations of the four radio-detected quasars in our sample. Photometric measurements are used to calibrate our spectroscopic data, ensuring that the flux density levels are accurately scaled. Details of the spectral data reduction are provided in Sec. 4.2.

1. Resample all spectra to a uniform resolution of 50 km s^{-1}, interpolating the flux density of spectrum to this resolution.

2. Calculate the weight for each spectrum as $w_i = \frac{1}{\sigma_i^2}$, where σ_i is the uncertainty for each spectrum.

3. Compute the combined flux density $f_{\rm comb}$ as a weighted average:

$$f_{\rm comb} = \frac{w_1 f_1 + w_2 f_2}{w_1 + w_2}.$$

4. Compute the combined uncertainty $\sigma_{\rm comb}$ as:

$$\sigma^2_{\rm comb} = \frac{1}{\frac{1}{\sigma_1^2} + \frac{1}{\sigma_2^2}}.$$

This approach ensures that noisier parts of the spectra contribute less to the final result while still improving the overall S/R ratio through their inclusion to the overall data.

4.2.3 Fitting of the Spectroscopic Data

The emission line features are extracted, and the spectrum is analyzed using the `Sculptor`[1] (Schindler, 2022) software, specifically designed for fitting and analyzing quasar spectra. The fitting process is summarized as follows:

1. **Masking Atmospheric Absorption:** Regions of the spectrum affected by strong atmospheric absorption are masked to avoid contamination.

[1] https://sculptor.readthedocs.io

Object	Date	Telescope/Instrument	Exposure(minutes)
P215–16	2011 August 19	VLT/X-Shooter	80
P352–15	2019 January 3	Gemini/GNIRS	40
	2018 October 11	VLT/X-Shooter	120
J2318–3113	2013 September 30	Gemini/GNIRS	65
	2016 August 5	VLT/X-Shooter	160
		Magellan/FIRE	175
J0410–0139	2020 November 7	VLT/FORS2	30
	2020 December 26	Keck/NIRES	72
	2021 Sepemter 23/	Magellan/FIRE	
	2021 October 15		360(in total)
	2021 October 23	LBT/LUCI-zJ	300
	2021 November 12	LBT/LUCI-HK	210

Table 4.3. The date, instruments, and exposure times (on-source time, no overheads included) for the spectroscopic observations of the four radio-detected quasars in our sample are summarized here. These observations were specifically designed to capture the broad emission lines of CIV and MgII, enabling the analysis of black hole properties. Details of the spectral data reduction are provided in Sec. 4.2.

2. **Continuum Fitting:** The continuum is modeled using a power law of the form $F_\lambda \propto \lambda^s$, where s represents the slope. The wavelength windows for fitting the continuum and the iron pseudo-continuum are selected following Shen & Liu (2012).

3. **Iron Pseudo-Continuum Modeling:** The iron pseudo-continuum near the MgII region is fitted using the iron templates from Tsuzuki et al. (2006) (T06) and Vestergaard & Wilkes (2001) (VW01), their difference discussed later in this section.

4. **Emission Line Fitting:** Prominent emission lines are fitted to extract their flux, full width at half maximum (FWHM), and redshift. These results are summarized in Table 4.4.

For the CIV emission line, we use two Gaussian components to account for the observed asymmetry. If no significant asymmetry is detected, a single Gaussian model is applied. The CIV line typically exhibits a blueshift relative to the quasar's systemic redshift. For our sample, the CIV blueshift ranges from $56\,\mathrm{km}\,s^{-1}$ to $1372\,\mathrm{km}\,s^{-1}$. The combined CIV profile's redshift is determined from the peak of the Gaussian profile, while the FWHM is calculated considering both Gaussian components. The line shift is derived from the Gaussian profile with the highest peak, and flux measurement includes contributions from both components.

The CIV emission line is known to exhibit significant blueshifts relative to the MgII line, attributed to quasar-driven outflows. This phenomenon often results in an overestimation of single-epoch virial black hole masses when calculated using CIV velocity widths (Coatman et al., 2017). To mitigate this issue, we apply a blueshift correction as prescribed by Coatman et al. (2017). The corrected FWHM of the CIV emission line is computed using the relation:

$$\mathrm{FWHM}_{\mathrm{CIV,corrected}} = \frac{\mathrm{FWHM}_{\mathrm{CIV,measured}}}{0.36 \times \frac{\mathrm{CIV\ Blueshift}}{10^3\,\mathrm{km\,s^{-1}}} + 0.61}.$$

FeII emission lines in the rest-frame UV quasar spectrum, especially those surrounding and overlapping with the MgII line, create prominent features that are crucial in shaping the overall spectral profile. Accurately modeling these FeII emissions is important especially for reliable fitting of the Mg II line. The T06 and VW01 templates are commonly employed for this purpose, we discuss their difference here:

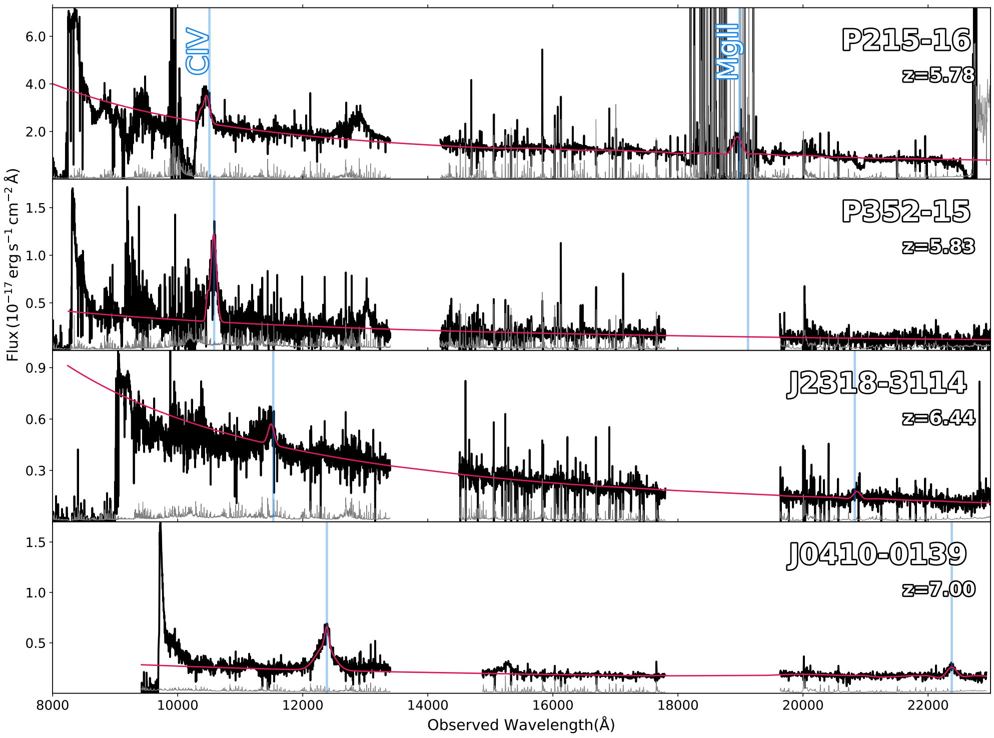

Figure 4.1. Panoramic spectra of the four quasars in our sample, all fully reduced and processed as described in Section 4.2. For P352–15, the MgII line lies within a strong atmospheric absorption region, thus its black hole properties are derived solely from the CIV line. For three quasars, both CIV and MgII emission lines are detected and used to calculate black hole properties, including black hole mass, bolometric luminosity and Eddington ratio. The detailed measurements of the emission lines and the derived black hole characteristics are summarized in Table 4.4 and Tab. 4.6.

- **T06 Template:** Derived from high-resolution spectra of Seyfert 1 galaxies, T06 provides detailed fitting of FeII emission in the rest-frame UV range (2200–3090 Å), making it suitable for high-resolution data.

- **VW01 Template:** While the VW01 template offers broader wavelength coverage (1070–3090 Å), it has lower resolution and does not capture FeII emission as precisely, especially near the MgII region.

We adopt the VW01 model for black hole property measurements due to its consistency across a broader wavelength range. Additionally, the black hole property measurement relations for MgII, as discussed in Sec. 4.4, are based on this template. The MgII emission line profiles fitted using both the VW01 and T06 templates are summarized in Tab. 4.4.

We show the spectra of quasars in our sample and their fitted models of continuum with emission lines in Fig. 4.1. With the zoomed-in figures of CIV and MgII lines in Fig. 4.2 and Fig. 4.2.

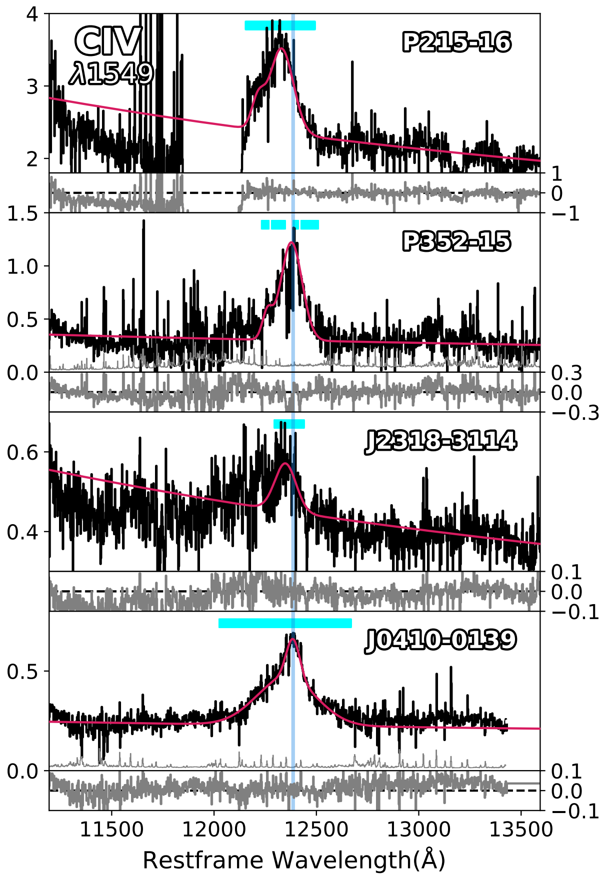

Figure 4.2. The zoomed-in views of the CIV emission line regions for the four quasars. The black lines represent the spectroscopic data, while the red lines indicate the fitted model, including Gaussian components for the emission lines and the continuum model. The gray lines show the residuals (i.e., the difference between the data and the model). The cyan windows at the top of each panel mark the fitting regions used to construct the line models, and the transparent blue vertical line represents the expected position of the CIV line without any blueshift or redshift.

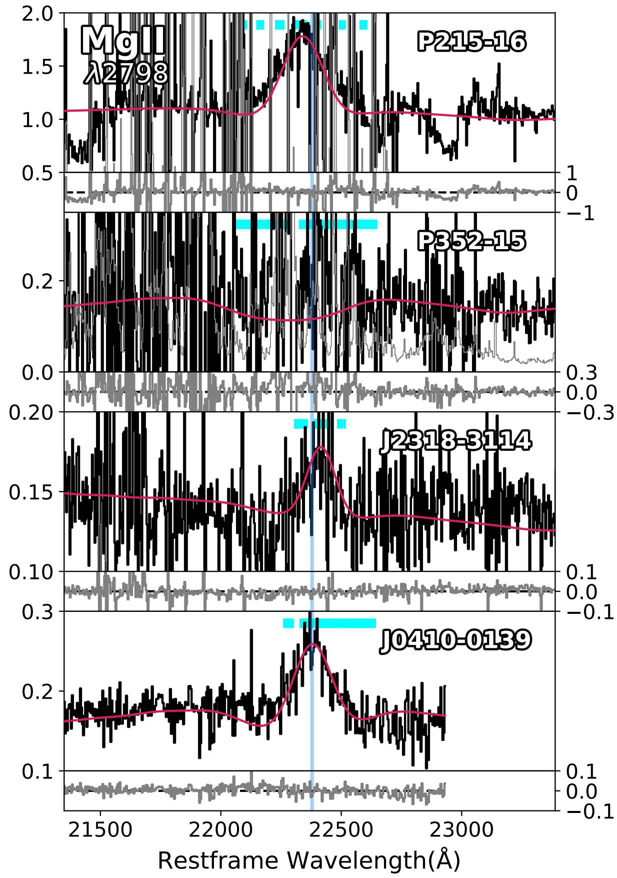

Figure 4.3. The same zoomed-in views of the MgII emission line regions for the four quasars in our sample as Fig. 4.2. For P352–15, the MgII line falls within a region of strong atmospheric absorption, making it inaccessible.

	C IV	C IV, corrected	Mg II(VW01)	Mg II(T06)
P215–16				
Redshift				
FWHM (km s^{-1})	4235±166	3836^{+184}_{-181}	2673±111	2510±117
$\Delta\nu$ (Line-CO, km s^{-1})	–1372±26	N/A	–524±45	–474±53
Flux (10^{-17} erg cm^{-2} s^{-1})	169±5	N/A	143±5	126±6
P352–15				
FWHM (km s^{-1})	2994±370	4331^{+2530}_{-1675}	2897±368	2526±409
$\Delta\nu$ (Line-[CII], km s^{-1})	–191±383	N/A	–939±154	–690±226
Flux (10^{-17} erg cm^{-2} s^{-1})	127±17	N/A	29±4	20±4
J2318–3113				
FWHM (km s^{-1})	2958±440	3149^{+687}_{-613}	1840±266	1711±260
$\Delta\nu$ (Line-[CII], km s^{-1})	–915±149	N/A	485±101	535±121
Flux (10^{-17} erg cm^{-2} s^{-1})	15±2	N/A	6±1	5±1
J0410–0139				
FWHM (km s^{-1})	4047±183	6422^{+570}_{-526}	2575±124	2223±122
$\Delta\nu$ (Line-MgII, km s^{-1})	–56±70	N/A	57±49	168±52
Flux (10^{-17} erg cm^{-2} s^{-1})	104±3	N/A	23±1	18±1

Table 4.4. The emission line profiles presented here are derived from Gaussian models fitted to the spectral data. The CIV line, known for its significant blueshift, is corrected to account for this effect in subsequent analyses. For the MgII line, measurements are conducted using two templates for the underlying iron pseudo-continuum models. The specific fitting procedures and corrections applied and the difference of two iron models are described in details in Sec. 4.2.3. The extracted line properties, including flux, FWHM, and line shifts, serve as inputs for calculating the black hole masses and related properties in Sec. 4.4.

4.3 Radio

To assess the radio-loudness of our quasar sample, we conducted radio observations using the VLA at a frequency of 3 GHz. The VLA images of P215-16 (Program ID: VLA/15A-145) and J2318-3113 (Program ID: VLA/16A-202) are shown in Fig. 4.4 and Fig. 4.5. The data editing, calibration, imaging, and flux density extractions were performed using the Common Astronomy Software Applications (CASA; McMullin et al. 2007).

The radio-loudness R of a quasar is defined as the ratio of the flux density between the radio and rest-frame optical bands:

$$R = \frac{f_{\nu,5\,\mathrm{GHz}}}{f_{\nu,4400\text{Å}}},$$

where $f_{\nu,5\,\mathrm{GHz}}$ is the rest-frame 5 GHz flux density, and $f_{\nu,4400\text{Å}}$ is the rest-frame optical flux density at 4400Å. A quasar is considered radio-loud if $R > 10$.

To calculate the 5 GHz radio-loudness, we started with the 3 GHz VLA data point (VLA S-band) and fitted a power-law model:

$$f = \nu^{\alpha},$$

where f is the radio flux density in Jy, and ν is the observed frequency. Assuming a spectral index of $\alpha = -0.67$, as reported by Bañados et al. (2021), we extrapolated the 5 GHz flux density for each source. Additionally, we incorporated data from other radio surveys, if available, to achieve a more reliable extrapolation.

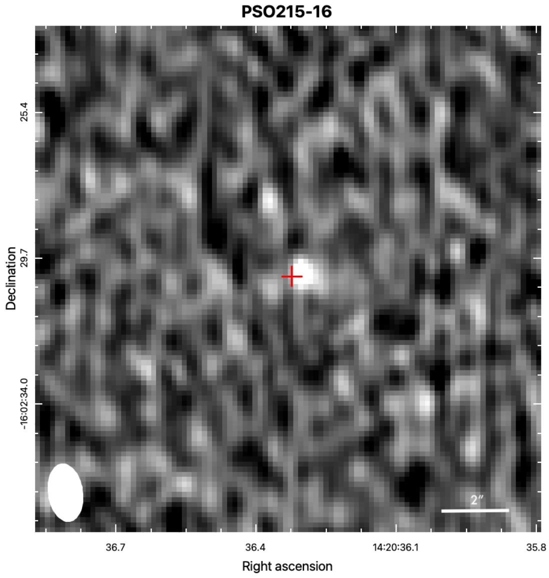

Figure 4.4. VLA 3 GHz radio images of P215–16. North is up, east is left. The beam size ($0.872'' \times 0.522''$) is shown in the bottom left corner. The flux density is extracted on this image to later calculate the radio-loudness.

The results of the radio observations and radio-loudness evaluations are summarized in Tab. 4.5.

4.4 Result

In this section, we measure the black hole properties using the emission line profiles. The black hole masses are calculated using the following relations for MgII and CIV:

$$M_{\mathrm{BH,MgII}} = 10^{6.86} \left(\frac{\mathrm{FWHM_{MgII}}}{1000\,\mathrm{km\,s^{-1}}} \right)^2 \left(\frac{\lambda L_\lambda(3000\text{Å})}{10^{44}\,\mathrm{erg\,s^{-1}}} \right)^{0.5}$$

and

	P215–16	P352–15	J2318–3113	J0410–0139	Instrument	Reference
$F_{0.215\,GHz}$ (mJy)		88±7			GMRT	[1]
$F_{0.888\,GHz}$ (mJy)		24.98±0.07	1.47±0.05	5.59±0.36	RACS	[2]
$F_{1.4\,GHz}$ (mJy)		14.9±0.7		4.3±0.4	NVSS	[3]
$F_{1.5\,GHz}$ (mJy)		14.9±0.7			VLBA	[4]
$F_{3\,GHz}$ (μJy)	77.7±9.96	8200±250	315.7±9.60		VLA	[5]
$R_{4400\text{Å}}$	2.7±0.5	1100±280	121±14	74±5		

Table 4.5. Radio flux density measurements of quasars in our sample are presented. All flux measurements are reported as peak flux density values. We derive the radio flux density and luminosity at rest-frame 5 GHz under the assumption that the radio spectrum for each quasar follows a power-law model of $F_\nu \propto \nu^\alpha$. Based on the extrapolated radio flux density at rest-frame 5 GHz and the rest-frame optical (4400Å) and UV (2500Å) continuum flux density, we calculate the radio-loudness R of each quasar.
References: [1]: Rojas-Ruiz et al. (2021); [2]: Hale et al. (2021); [3]: Condon et al. (1998); [4]: Momjian et al. (2018); [5]: P215-16: VLA/15A-145; P352-15: [1]; J2318-3113: VLA/16A-202

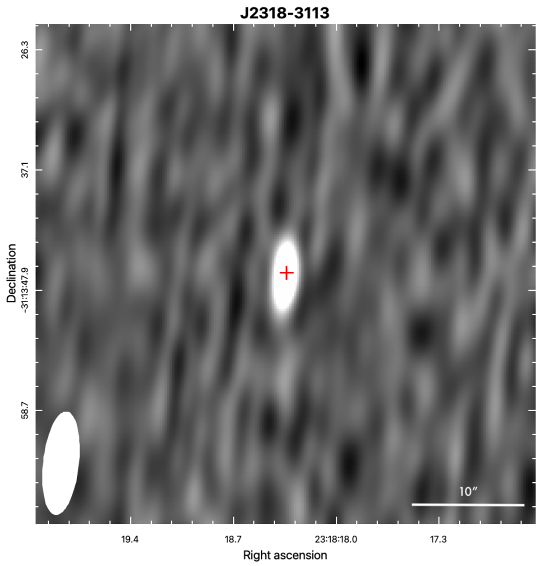

Figure 4.5. The same as Fig. 4.4 for J2318-3113. The beam size (4.676" × 1.61") is shown in the bottom left corner.

$$M_{\mathrm{BH}} = 10^{6.66} \left(\frac{\mathrm{FWHM}_{\mathrm{CIV,corrected}}}{1000\,\mathrm{km\,s^{-1}}} \right)^2 \left(\frac{\lambda L_\lambda(1350\text{Å})}{10^{44}\,\mathrm{erg\,s^{-1}}} \right)^{0.53},$$

where $\lambda L_\lambda(3000, 1350\text{Å})$ is the monochromatic luminosity at the rest-frame wavelengths of 3000 and 1350Å respectively. This quantity is derived from the best-fit continuum model for each quasar in our sample.

The bolometric luminosity is estimated using the relation from Richards et al. (2006):

$$L_{\mathrm{bol}} = 5.15 \times \lambda L_\lambda(3000\text{Å}),$$

and the Eddington luminosity is calculated using the equation from Eddington (1926):

$$L_{\mathrm{Edd}} = 1.26 \times 10^{38}\,\mathrm{erg\,s^{-1}} \left(\frac{M_{\mathrm{BH}}}{M_\odot} \right).$$

The black hole properties derived from these calculations are summarized in Tab. 4.6. We note that for J0410–0139, the MgII-based black hole mass was reported by Banados et al. 2024b as $6.9^{+0.5}_{-0.4} \times 10^8\, M_\odot$. Our analysis yields a mass of $1.2 \times 10^9\, M_\odot$. This discrepancy, by a factor of ~ 1.7, can be attributed to systematic differences in the empirical relations used for black hole mass estimation.

4.5 Comparison

We compare our sample of $z > 5.3$ (high-z) quasars, primarily radio-loud, to samples of lower-redshift (low-z) quasars, including both radio-quiet and radio-loud counterparts, as well as to high-z radio-quiet quasars, which represent the majority of high-redshift quasars observed to date. The goal is to investigate potential differences in black hole properties across these groups, focusing on black hole mass, accretion rate, and bolometric luminosity. These properties provide insights into the accretion characteristics of

	P215–16	P352–15	J2318–3113	J0410–0139
R.A.	$14^h20^m36^s\!.98$	$23^h29^m36^s\!.84$	$23^h18^m18^s\!.35$	$04^h10^m09^s\!.05$
Dec.	$-16°02'30''\!.25$	$-15°20'14''\!.46$	$-31°13'46''\!.34$	$-01°39'19''\!.88$
Redshift	5.783 (CO)	5.832 ([CII])	6.442 ([CII])	6.996 ([CII])
m_{1450} (AB Mag)	19.07	21.30	20.65	21.33
M_{1450} (AB Mag)	–27.56	–25.34	–26.16	–25.61
$\log \lambda L_{1350\text{Å}}$ (erg s^{-1})	$47.01^{+0.00}_{-0.00}$	$46.11^{+0.00}_{-0.00}$	$46.45^{+0.01}_{-0.01}$	$46.19^{+0.01}_{-0.00}$
$\log \lambda L_{2500\text{Å}}$ (erg s^{-1})	$46.84^{+0.01}_{-0.01}$	$45.93^{+0.01}_{-0.01}$	$46.17^{+0.01}_{-0.01}$	$46.25^{+0.03}_{-0.04}$
$\log \lambda L_{3000\text{Å}}$ (erg s^{-1})	$46.83^{+0.01}_{-0.01}$	$45.88^{+0.01}_{-0.01}$	$46.09^{+0.02}_{-0.02}$	$46.27^{+0.05}_{-0.05}$
$\log \lambda L_{4400\text{Å}}$ (erg s^{-1})	$46.44^{+0.02}_{-0.02}$	$45.77^{+0.02}_{-0.02}$	$45.87^{+0.03}_{-0.03}$	$46.27^{+0.08}_{-0.08}$
$\log M_{\rm BH,CIV}$ ($M_\odot$)	$9.42^{+0.04}_{-0.04}$	$9.05^{+0.40}_{-0.42}$	$8.95^{+0.18}_{-0.19}$	$9.44^{+0.08}_{-0.07}$
$\log M_{\rm BH,MgII}$ ($M_\odot$)	$9.13^{+0.04}_{-0.04}$	$8.72^{+0.11}_{-0.12}$	$8.43^{+0.13}_{-0.15}$	$8.82^{+0.07}_{-0.07}$
$\log L_{\rm bol}$ (erg s^{-1})	$47.54^{+0.01}_{-0.01}$	$46.59^{+0.01}_{-0.01}$	$46.80^{+0.02}_{-0.02}$	$46.98^{+0.05}_{-0.05}$
$\lambda_{\rm Edd,CIV}$	$1.04^{+0.13}_{-0.12}$	$0.28^{+0.47}_{-0.17}$	$0.56^{+0.35}_{-0.20}$	$0.28^{+0.09}_{-0.07}$
$\lambda_{\rm Edd,MgII}$	$2.05^{+0.26}_{-0.22}$	$0.59^{+0.21}_{-0.14}$	$1.85^{+0.86}_{-0.53}$	$1.16^{+0.36}_{-0.27}$

Table 4.6. Black hole properties for each quasar in our sample. These properties are derived from the spectroscopic data reduced through the process described in Sec. 4.2.3, using the emission line profiles extracted from the fitting models.

quasars across redshifts and between radio-loud and radio-quiet populations.

The central question is whether high-z, radio-loud quasars form a distinct population due to their combination of high redshift and radio-loudness. To address this, we define two distinct comparison groups. First, we compare our sample to high-z quasars (also at $z > 5.3$), predominantly radio-quiet. Second, we analyze low-z radio-quiet and radio-loud quasars. In the following sections, we detail the methodology used to assemble these comparison groups and present the results of our analyses.

4.5.1 High-z radio-quiet quasars

We constructed the high-z sample by first utilizing the complementary catalog provided by Fan et al. 2023. In addition, we incorporated black hole property measurements from the recent study by Mazzucchelli et al. 2023, which includes 41 quasars at $z \gtrsim 6$. By incorporating this dataset with additional high-redshift quasar measurements from the literature (for $z > 5.3$), and considering that black hole mass estimates can vary depending on the emission line used, we rely on the MgII line for mass estimation due to its less susceptibility to outflows compared to the CIV line. We retain only those quasars with valid MgII-based black hole mass and bolometric luminosity measurements, resulting in a high-z sample of 131 quasars. The comparison between our high-z sample and low-z quasars is presented in Fig. 4.6.

We find that our sample of four quasars falls within the range typically occupied by most high-z quasars in terms of black hole mass and bolometric luminosity. There is no significant evidence suggesting that the black hole properties of our sample are outstanding. However, due to the small size of our sample of only four sources, this observation remains limited, and further insights would require a larger dataset.

4.5.2 Low-z radio-quiet/radio-loud quasars

To compare black hole properties between our high-z sample and low-z quasars, we use the SDSS DR16Q catalog (Wu & Shen, 2022), which provides black hole mass measurements at lower redshifts (redshift range determined below) acquired from SDSS spectra, also using the broad emission lines such as CIV and MgII.

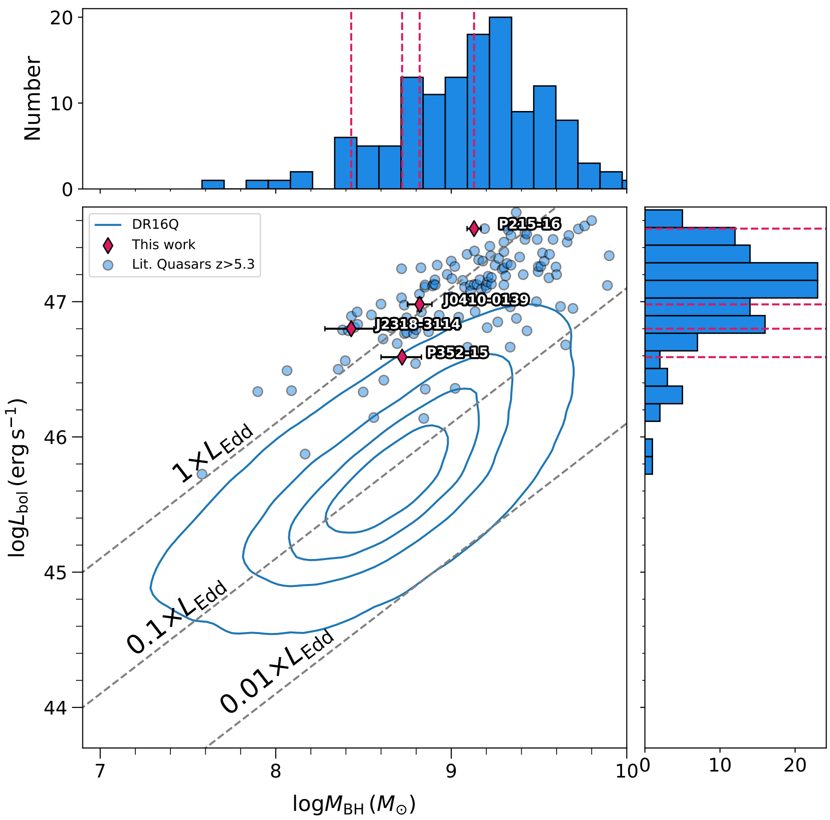

Figure 4.6. The comparison of radio-loud and radio-quiet quasars at high-z, on the plane of the black hole mass (x axis) and bolometric luminosity (y axis). The accretion rate and Eddington ratio are drawn on the plot as well as dashed lines, note that the leftmost dashed line represents the Eddington limit. The blue points show the 131 high-z quasars, which are all radio-quiet. The top and right panels show the distributions of these 131 quasars, in bins, shown as histograms. The red diamonds are the quasars in our sample. The four red dashed lines show the positions of the quasars in our sample, pinning down their position in the distribution of black hole mass or bolometric luminosity relative to the 131 high-z quasars. The blue contour represents the low-z quasars, which are mostly radio-quiet, as detailed in Sec. 4.5.2.

We select SDSS DR16Q quasars with valid MgII-based single-epoch black hole mass measurements, applying the following selection criteria to minimize bias of accessing only the most faintest or the brightest quasars and ensure high S/N ratios. The criteria are also recommended by Wu & Shen 2022. We summarize them here. For each quasar selected, the following rules are met:

1. $F_{\mathrm{MgII}}/\mathrm{Err\_}F_{\mathrm{MgII}} > 2$
2. $38 < \log \lambda L_{\mathrm{MgII}}/\mathrm{erg\,s^{-1}} < 48$
3. A valid UV continuum luminosity at rest-frame 2500 Å
4. A valid black hole mass measurement using the MgII line

Using these criteria, we obtain a sample of 461,459 quasars within the redshift range $0.27 < z < 2.73$, all ensuring reliable black hole mass measurements from the MgII line.

In the next step, we build our own radio-loud sample with the low-z SDSS quasars. We incorporate additional radio surveys to calculate radio-loudness for the SDSS DR16Q quasars. We use measurements from LOFAR (150 MHz; LoTSS DR2), ASKAP (888 MHz; RACS-low1 DR1), and the Very Large Array Sky Survey (3 GHz; VLASS epoch 2 data) to estimate the rest-frame 5 GHz flux density as they are currently the most extensive radio surveys in sky coverage. By fitting a power-law model to each quasar's radio spectrum, we derive the rest-frame 5 GHz flux density and compute radio-loudness as $R_{2500\text{Å}} = F_{5,\mathrm{GHz}}/F_{2500\text{Å}}$. We retain only quasars with best-fitted radio spectra (Coefficient of Determination $R^2 > 0.95$), resulting in a sample of 500 radio-detected SDSS DR16Q quasars. The comparison of this low-z sample with our high-z quasars is shown in Fig. 4.7.

Now we have both radio-quiet and radio-loud populations in low-z. As a primer study, we can use them to leverage the problem of the lack of sources in high-z (131 radio-quiet vs. 4 radio-detected). In this case, in the low-z sample, we have 500 radio-loud quasars to compare with more than 400 thousand radio-quiet quasars.

To better qualitify the comparison, we apply the Kolmogorov-Smirnov (KS) test, a non-parametric statistical test that assesses whether two samples are drawn from the same underlying probability distribution. The p-value in a KS test tells us how likely it is that the differences between the two distributions happened by chance. A p-value close to zero means the distributions are likely different, while a p-value close to 1 means there is nearly no difference between the distributions. We used the KS test to compare the low-z radio-quiet and radio-loud samples. The comparison is designed as follows:

1. We first match for one black hole property only, the to-be-matched distribution is determined with the radio-loud sample.
2. In the radio-quiet sample, we draw the distribution of the selected black hole property and create a random sample such that the distribution of the black hole property is the same as the radio-loud ones (the p-value between two samples is 1).
3. We check the other black hole properties in the newly generated sample, compared with radio-loud quasars.

The comparison results are presented in Tab. 4.7.

We can conclude from the test that when matched in black hole mass, the matched sample of radio-quiet quasars has slightly smaller bolometric luminosity, which leads to a slightly smaller accretion rate.

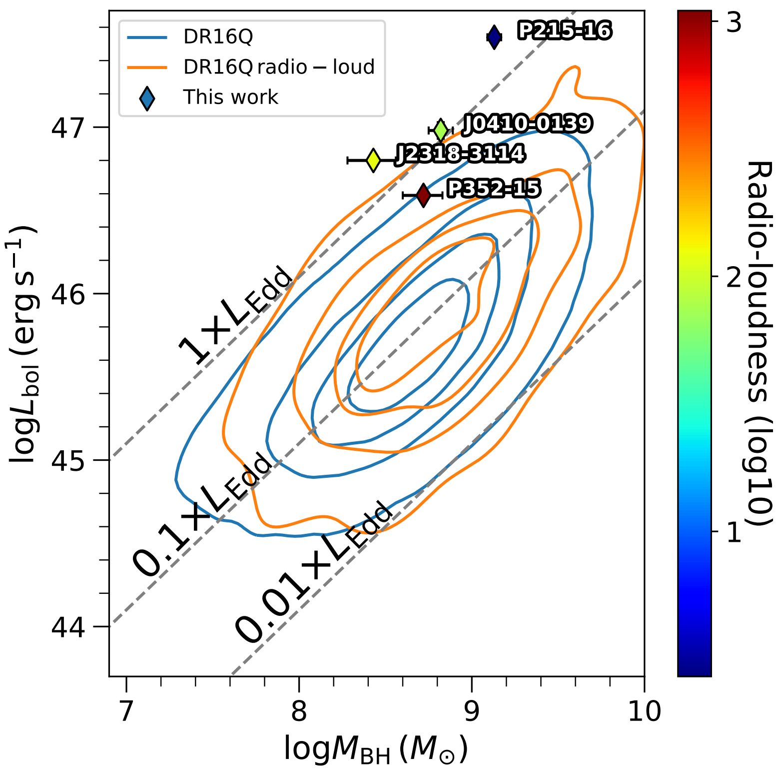

Figure 4.7. The comparison between the radio-loud quasars from SDSS DR16Q and the quasars in our sample, on the plane of the black hole mass (x axis) and bolometric luminosity (y axis). The accretion rate and Eddington ratio are drawn on the plot as well as a dashed line, note that the leftmost dashed line represents the Eddington limit. The blue contour represents the radio-quiet quasars in SDSS DR16Q, serving as the representatives of low-z radio-quiet quasars to be matched with the orange contour, the low-z radio-loud quasars. Our quasars in the sample are marked with diamonds, with color bars showing their radio-loudness. Since our quasars are all high-z, they are biased to be bright and massive, making them easier to observe. The comparison of low-z quasars is detailed in Sec. 4.5.2.

	SDSS RL sample			SDSS RQ sample			
	Mean	Median	Std. Dev.	Mean	Median	Std. Dev.	P-value
Matched $M_{\mathrm{BH,MgII}}$							
log $M_{\mathrm{BH,MgII}}$ ($M_\odot$)	8.80	8.80	0.49	matched	matched	matched	1.0×10^{0}
log L_{bol} (erg s^{-1})	45.85	45.85	0.50	45.79	45.77	0.51	9.3×10^{-5}
$\lambda_{\mathrm{Edd,MgII}}$	0.15	0.09	0.17	0.11	0.08	0.11	2.5×10^{-9}
Matched L_{bol}							
log $M_{\mathrm{BH,MgII}}$ ($M_\odot$)	8.80	8.80	0.49	8.74	8.76	0.47	4.1×10^{-4}
log L_{bol} (erg s^{-1})	45.85	45.85	0.50	matched	matched	matched	1.0×10^{0}
$\lambda_{\mathrm{Edd,MgII}}$	0.15	0.09	0.17	0.15	0.11	0.14	1.0×10^{-10}

Table 4.7. The KS test of radio-loud quasars to the matched sample of radio-quiet quasars. We control one property and in the matched sample we study if there are any significant differences in the other black hole properties. We conclude that although there are differences in the other black hole properties, the accretion rate is similar between radio-loud and radio-quiet samples.

However, when matched in bolometric luminosity, the black hole masses of the radio-quiet quasars are smaller, resulting in higher accretion rates. In both cases, the median of the accretion rates does not show a significant difference between radio-loud and radio-quiet quasars. It is still unclear whether radio-loud quasars are accreting faster than radio-quiet quasars in this case.

III

Summary and Outlook

5

Chapter 5

5.1 Summary

This thesis presents a comprehensive investigation into radio-loud quasars, applying multiple methodologies, including radio imaging and optical/near-infrared spectroscopy. The primary focus of the study is on radio observations and spectroscopy, beginning with a detailed examination of blazarsa class of quasars with jets oriented nearly toward Earth. By analyzing their morphology, the thesis facilitates improved identification of blazars. In the subsequent part, the thesis addresses whether radio-loud quasars exhibit unique black hole properties distinct from those of radio-quiet quasars, particularly due to their prominent radio jets.

Chapter 1 provides the theoretical context, establishing the cosmological framework and foundational models of AGN. This chapter also introduces the main physical properties of AGN pertinent to this research, including black hole mass and accretion rates. The chapter then describes the core subject of the thesis, radio-loud AGNs, focusing on their radio jets, blazar classification, and the defining characteristics of radio-loud quasars.

The research in this thesis unfolds in two main parts:

The first part centers on identifying compact blazar morphology within radio images. An analytical algorithm developed in Chapter 2 distinguishes blazars from non-blazars in a dataset of blazar candidates. We then apply this algorithm to the existing catalogues of both known blazars and blazar candidates, discovering that our algorithm updates some of the results, highlighting differences from previously reported findings. Chapter 3 presents a validation study for this algorithm, where an AGN initially misclassified as a blazar candidate was re-evaluated through follow-up observations with the Very Large Telescope (VLT), confirming it to be a non-blazar. This validation underscores the algorithms accuracy and reliability in identifying true blazars.

The second segment explores the black hole properties of radio-loud quasars in the distant universe. Using observational data from ground-based telescopes, this section wants to address key questions about the growth of supermassive black holes in the early universe, particularly investigating whether radio jets contribute to this growth. Chapter 4 focuses on four quasars with redshifts greater than 5.5, employing MgII and CIV broad lines to analyze their black hole properties. A comparative analysis is conducted with both radio-quiet and radio-loud SDSS quasars, as well as other high-redshift radio-quiet quasars. However, despite this comparison, we are unable to determine if the presence of jets plays a crucial role in distinguishing them as a unique population when compared to high-z radio-quiet quasars, where jets might influence accretion, or low-z radio-loud populations. This uncertainty is primarily due to the limited sample size of four quasars.

5.2 Outlook

5.2.1 Upcoming data

We aim to include a larger sample to expand our study of comparing the black hole properties of radio-loud quasars to those of other quasars. As discussed in Sec. 4.5, the size of the radio-loud quasar sample at high-z is critical for establishing a robust comparison to their counterparts: high-z radio-quiet quasars and radio-loud quasars at lower redshifts (e.g., SDSS quasars). The work presented in Chapter 4 serves as an initial investigation and pilot study to measure the black hole properties for four quasars in our sample. In an effort to increase the sample size, we have been collecting additional black hole properties of high-z radio-loud quasars, aiming to construct an enlarged sample that can provide more robust insights into the comparison of black hole properties.

The enlarged sample of high-z radio-loud quasars was entirely observed with the LBT/LUCI. To maximize wavelength coverage, we used the binocular mode setup, where both telescopes operate simultaneously: one equipped with LUCI1 to cover the wavelength range of the CIV line (zJspec), and the other with LUCI2, configured to cover the MgII line (HKspec) for most quasars in our sample. For quasars with poor-quality optical spectra, we also requested observations with MODS using the red grating configuration to cover the Ly-α. Fig. 5.1 summarizes our observational setup and how the spectra are distributed across the instrument configurations.

For target acquisition, we used a nearby offset star to position the slit before tilting it to cover the target. In most cases, the targets were visible in the acquisition image, ensuring proper alignment within the slit. For very faint targets, we employed a blind offset method, where the slit was first aligned with a bright star offset from the target and then shifted to the target based on its known coordinates. All exposures followed an ABBA dithering pattern, and a telluric standard star was observed before or after each science observation.

Over five semesters between 2021 and 2023 (see Tab. 5.1), we obtained spectroscopic observations of 22 $z > 5$ quasars with the LBT. These spectra cover key broad emission lines, enabling measurements of the central black hole properties of these quasars.

The data reduction process for the entire sample is ongoing and will be published soon in a separate journal article. The process will follow the methodology described in Chapter 4. This dataset will provide the first comprehensive sample of radio-loud quasars with measured black hole properties. It will also enable comparisons to high-z radio-quiet quasars, which have dominated past research, and to low-z radio-loud quasars, shedding light on potential evolutionary trends within the jetted population. Here, we present preliminary spectra of eight targets from our enlarged sample in Fig. 5.2 and Fig. 5.3. These spectra prominently feature broad emission lines of CIV and/or MgII, offering promising prospects for reliable black hole property measurements.

5.2.2 Future study

Beyond measuring the black hole properties in the upcoming LBT sample, additional analyses of our dataset can provide deeper insights into quasar properties and the nature of radio-loud quasars in the early universe. For example, refining the continuum analysis by incorporating dust reddening corrections can yield a more accurate de-reddened continuum fit. This refinement would improve the characterization of the CIV emission line, reducing uncertainties caused by dust reddening. For instance, one quasar in our sample, J2318-3113, exhibits disturbed radio morphology in ALMA [CII] images, which suggests the

Semester	Time awarded	PI
2021B	14 hours	Bañados
2022A	22 hours	Xie
2022B	25 hours	Xie
2023A	20 hours	Xie

Table 5.1. LBT observations in four semesters. All LBT observations were conducted to collect spectroscopic data for additional radio-loud quasars, aiming to determine their black hole properties through broad emission lines. The quasar sample was selected from known radio-loud quasars, with instruments chosen specifically to capture the broad emission lines (CIV and/or MgII) at the corresponding redshifts.

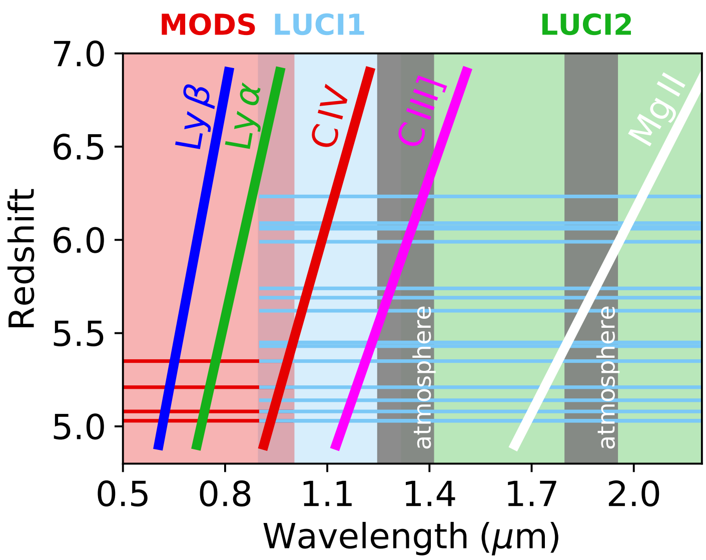

Figure 5.1. The wavelength span of the spectra of our targets (indicated by horizontal lines) on the configurations of the LBT instruments is presented. The two instruments on the LBT, MODS and LUCI, offer distinct wavelength coverage. Within the redshift range of most quasars in our sample, LUCI provides simultaneous coverage of the CIV and MgII emission lines. These spectra enable us to estimate black hole properties using single-epoch black hole mass estimation methods. For objects with an optical spectrum of poor quality, we request MODS observations.

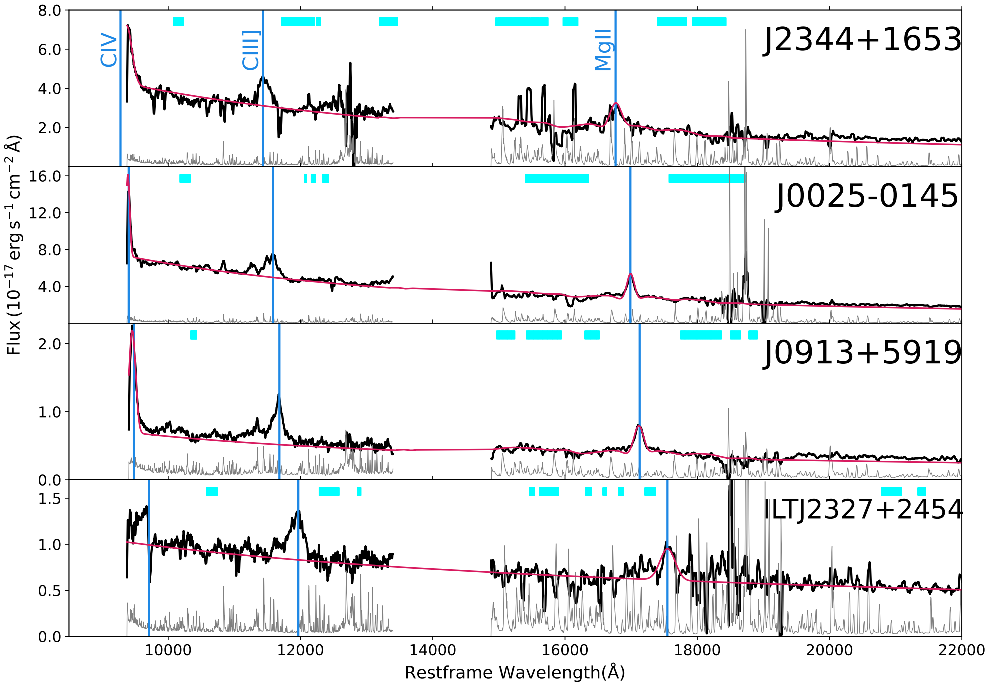

Figure 5.2. The preliminary spectra of quasars in the upcoming enlarged radio-loud high-z sample, all obtained with the LBT. These spectra will include broad emission lines such as CIV and MgII (if not only CIV, due to contamination or lack of wavelength coverage), allowing for the measurement of black hole properties. This analysis will help determine whether radio-loud high-z quasars are distinctly accreting faster than other quasars.

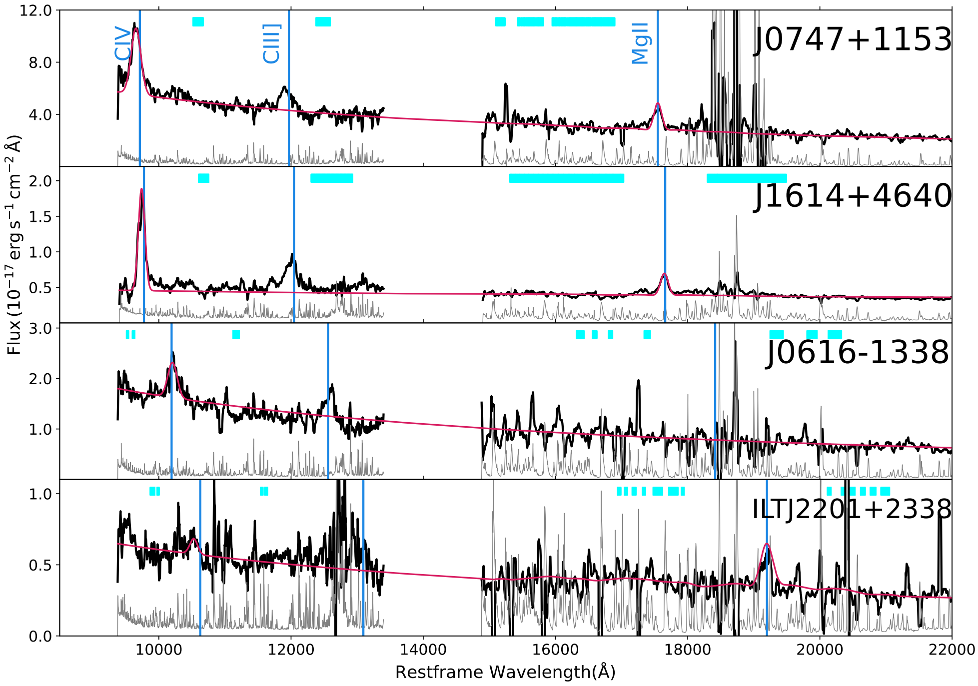

Figure 5.3. Same as Fig. 5.2 for 4 more quasars in the upcoming englarged sample.

presence of companion absorbers that could be quasar-driven outflows (Venemans et al., 2020; Neeleman et al., 2021). Refining its spectrum would enable a more precise identification of absorbers in the rest-frame UV spectrum, supporting the interpretation of these features as absorbers. Furthermore, such an analysis could extend to estimating the occurrence of similar absorbers in other radio-loud quasars in the sample, providing valuable insights into their frequency and role in the evolution of radio-loud quasars.

Furthermore, our spectroscopic data could facilitate the identification of Broad Absorption Line (BAL) quasars, a subclass of objects characterized by fast outflows (reaching velocities of up to $\sim 0.2c$, Bischetti et al. 2022) that intercept the observer's line of sight. Identifying BAL quasars would enable further investigations into quasar outflows, including their location relative to the galactic center (e.g., He et al., 2019) and their occurrence rate within the overall quasar population (e.g., Yang et al., 2021; Bischetti et al., 2023). These analyses could significantly enhance our understanding of quasar feedback mechanisms and their role in galaxy evolution in the early universe.

Additionally, comparing the CIV line with other emission lines can offer estimates of metallicity and iron enrichment, providing valuable information on the evolution of chemical abundances in the quasar's environments(Onoue et al., 2020; Schindler et al., 2020). We will focus on comparing CIV with other prominent lines such as MgII and AlIII, which are widely available in our sample, in order to investigate potential iron enrichment evolution between high-z and low-z quasar populations. This is especially important for examining jetted quasars at high redshifts, a category previously unexamined in earlier studies.

Future research on high-redshift quasars can also benefit from the analysis of additional intermiediate ionization lines of AlIIIλ1857Å, SiIIIλ1892Å, and CIII]λ1909Å emission lines, complementing the existing measurements of CIV and MgII lines. These intermediate ionization lines offer several advantages for probing the physical conditions and properties of quasars in the early universe. The AlIII, SiIII], and CIII] lines offer unique insights into the dynamics and structure of the BLR in high-z quasars. These lines are less affected by strong outflows compared to CIV, making them more reliable indicators of the BLR's virial motions (Marziani et al., 2017; Martínez-Aldama et al., 2018). Buendia-Rios et al. 2023 observed that AlIII λ1860 shows median line shifts of ∼-250 km/s, compared to CIV at ∼-600 km/s. This stability makes these lines valuable for studying the BLR's kinematics and ionization structure across different quasar populations, for instance, between quasars that have and those that do not have significant outflows, specifically influencing the CIV line. In the same work, they show that these three lines exhibit consistent width and shape with the profile of Hβ lines, making them a potential virial estimator for black hole properties as well. Comparing these lines to our results estimated from CIV and MgII can help us gain more insights into the differences among these broad emission lines.

Moreover, the relative flux of AlIII, SiIII], and CIII] lines can provide crucial information about the chemical composition and metallicity of high-z quasars. These measurements are essential for understanding the early chemical evolution of galaxies and the interstellar medium in the young universe. For example, the emission-line ratio of CIII]/CIV can be used to study the BLR chemical enrichment and track its evolution with redshift. Future studies could expand on the work of De Rosa et al. 2014, who used metal lines to trace chemical enrichment in high-redshift quasars and study its evolution.

Data, Code and Software

The research included in this thesis is based on observations made with ESO VLT at the Paranal Observatory under the Program ID of 106.20WQ.

The National Radio Astronomy Observatory is a facility of the National Science Foundation operated under cooperative agreement by Associated Universities, Inc.

This publication makes use of data products from the Wide-field Infrared Survey Explorer, which is a joint project of the University of California, Los Angeles, and the Jet Propulsion Laboratory/California Institute of Technology, funded by the National Aeronautics and Space Administration.

The Legacy Surveys consist of three individual and complementary projects: the Dark Energy Camera Legacy Survey (DECaLS; Proposal ID #2014B-0404; PIs: David Schlegel and Arjun Dey), the Beijing-Arizona Sky Survey (BASS; NOAO Prop. ID #2015A-0801; PIs: Zhou Xu and Xiaohui Fan), and the Mayall z-band Legacy Survey (MzLS; Prop. ID #2016A–0453; PI: Arjun Dey). DECaLS, BASS and MzLS together include data obtained, respectively, at the Blanco telescope, Cerro Tololo Inter-American Observatory, NSFs NOIRLab; the Bok telescope, Steward Observatory, University of Arizona; and the Mayall telescope, Kitt Peak National Observatory, NOIRLab. Pipeline processing and analyses of the data were supported by NOIRLab and the Lawrence Berkeley National Laboratory (LBNL). The Legacy Surveys project is honored to be permitted to conduct astronomical research on Iolkam Duag (Kitt Peak), a mountain with particular significance to the Tohono Oodham Nation.

NOIRLab is operated by the Association of Universities for Research in Astronomy (AURA) under a cooperative agreement with the National Science Foundation. LBNL is managed by the Regents of the University of California under contract to the U.S. Department of Energy.

This project used data obtained with the Dark Energy Camera (DECam), which was constructed by the Dark Energy Survey (DES) collaboration. Funding for the DES Projects has been provided by the U.S. Department of Energy, the U.S. National Science Foundation, the Ministry of Science and Education of Spain, the Science and Technology Facilities Council of the United Kingdom, the Higher Education Funding Council for England, the National Center for Supercomputing Applications at the University of Illinois at Urbana-Champaign, the Kavli Institute of Cosmological Physics at the University of Chicago, Center for Cosmology and Astro-Particle Physics at the Ohio State University, the Mitchell Institute for Fundamental Physics and Astronomy at Texas A&M University, Financiadora de Estudos e Projetos, Fundacao Carlos Chagas Filho de Amparo, Financiadora de Estudos e Projetos, Fundacao Carlos Chagas Filho de Amparo a Pesquisa do Estado do Rio de Janeiro, Conselho Nacional de Desenvolvimento Cientifico e Tecnologico and the Ministerio da Ciencia, Tecnologia e Inovacao, the Deutsche Forschungsgemeinschaft and the Collaborating Institutions in the Dark Energy Survey. The Collaborating Institutions are Argonne National Laboratory, the University of California at Santa Cruz, the University of Cambridge, Centro de Investigaciones Energeticas, Medioambientales y Tecnologicas-Madrid, the University of Chicago, University College London, the DES-Brazil Consortium, the University of Edinburgh, the Eidgenossische Technische Hochschule (ETH) Zurich, Fermi National Accelerator Laboratory, the University of Illinois at Urbana-Champaign, the Institut de Ciencies de lEspai (IEEC/CSIC), the Institut de Fisica dAltes Energies, Lawrence Berkeley National Laboratory, the Ludwig Maximilians Universitat Munchen and the associated Excellence Cluster Universe, the University of Michigan, NSFs NOIRLab, the University of Nottingham, the Ohio State University, the University of Pennsylvania, the University of Portsmouth, SLAC National Accelerator Laboratory, Stanford University, the University of Sussex, and Texas A&M University.

BASS is a key project of the Telescope Access Program (TAP), which has been funded by the National Astronomical Observatories of China, the Chinese Academy of Sciences (the Strategic Priority Research Program The Emergence of Cosmological Structures Grant # XDB09000000), and the Special Fund for Astronomy from the Ministry of Finance. The BASS is also supported by the External Cooperation Program of Chinese Academy of Sciences (Grant No. 114A11KYSB20160057), and Chinese National Natural Science Foundation (Grant No. 12120101003, No. 11433005).

The Legacy Survey team makes use of data products from the Near-Earth Object Wide-field Infrared Survey Explorer (NEOWISE), which is a project of the Jet Propulsion Laboratory/California Institute of Technology. NEOWISE is funded by the National Aeronautics and Space Administration.

The Legacy Surveys imaging of the DESI footprint is supported by the Director, Office of Science, Office of High Energy Physics of the U.S. Department of Energy under Contract No. DE-AC02-05CH1123, by the National Energy Research Scientific Computing Center, a DOE Office of Science User Facility under the same contract; and by the U.S. National Science Foundation, Division of Astronomical Sciences under Contract No. AST-0950945 to NOAO.

The Pan-STARRS1 Surveys (PS1) and the PS1 public science archive have been made possible through contributions by the Institute for Astronomy, the University of Hawaii, the Pan-STARRS Project Office, the Max-Planck Society and its participating institutes, the Max Planck Institute for Astronomy, Heidelberg and the Max Planck Institute for Extraterrestrial Physics, Garching, The Johns Hopkins University, Durham University, the University of Edinburgh, the Queen's University Belfast, the Harvard-Smithsonian Center for Astrophysics, the Las Cumbres Observatory Global Telescope Network Incorporated, the National Central University of Taiwan, the Space Telescope Science Institute, the National Aeronautics and Space Administration under Grant No. NNX08AR22G issued through the Planetary Science Division of the NASA Science Mission Directorate, the National Science Foundation Grant No. AST1238877, the University of Maryland, Eotvos Lorand University (ELTE), the Los Alamos National Laboratory, and the Gordon and Betty Moore Foundation.

This thesis has made use of data from the MOJAVE database that is maintained by the MOJAVE team (Lister et al., 2018). This thesis has made use of the SIMBAD database, operated at CDS, Strasbourg, France (Wenger et al., 2000). This thesis has made use of NASA's Astrophysics Data System.

The following softwares and packages has have been used throughout the thesis: Python (Van Rossum & Drake, 2009), APLpy (Robitaille & Bressert, 2012), AstroPy (Astropy Collaboration et al., 2013, 2018, 2022), Astroquery (Ginsburg et al., 2019), Matplotlib (Hunter, 2007), NumPy (van der Walt et al., 2011; Harris et al., 2020), Pandas (McKinney, 2010; Reback et al., 2022), SAOImage DS9 (Joye & Mandel, 2003), SciPy (Virtanen et al., 2020), Jupyter (Perez & Granger, 2007; Kluyver et al., 2016), SeaBorn (Waskom, 2021) and TOPCAT (Taylor, 2005), speclite (Kirkby et al., 2024) and SpectRes (Carnall, 2017). ChatGPT, a variant language model based on GPT-3 (Brown et al., 2020) is employed to correct grammatical errors and impove readability within the text of this thesis.

Bibliography

Abbott, R., Abbott, T. D., Abraham, S., et al. 2020, PhRvL, 125, 101102, doi: 10.1103/PhysRevLett.125.101102

Abdo, A. A., Ackermann, M., Agudo, I., et al. 2010, ApJ, 716, 30, doi: 10.1088/0004-637X/716/1/30

Abdo, A. A., Ackermann, M., Ajello, M., et al. 2015, ApJ, 799, 143, doi: 10.1088/0004-637X/799/2/143

Abdollahi, S., Acero, F., Baldini, L., et al. 2022a, ApJS, 260, 53, doi: 10.3847/1538-4365/ac6751

—. 2022b, ApJS, 260, 53, doi: 10.3847/1538-4365/ac6751

Abel, T., Bryan, G. L., & Norman, M. L. 2002, Science, 295, 93, doi: 10.1126/science.295.5552.93

Afonso, J., Casanellas, J., Prandoni, I., et al. 2015, in Advancing Astrophysics with the Square Kilometre Array (AASKA14), 71, doi: 10.22323/1.215.0071

Ajello, M., Angioni, R., Axelsson, M., et al. 2020, ApJ, 892, 105, doi: 10.3847/1538-4357/ab791e

Antonucci, R. R. J., Hickson, P., Olszewski, E. W., & Miller, J. S. 1986, AJ, 92, 1, doi: 10.1086/114128

Appenzeller, I., Fricke, K., Fürtig, W., et al. 1998, The Messenger, 94, 1

Arsioli, B., & Chang, Y. L. 2018, A&A, 616, A63, doi: 10.1051/0004-6361/201833005

Astropy Collaboration, Robitaille, T. P., Tollerud, E. J., et al. 2013, A&A, 558, A33, doi: 10.1051/0004-6361/201322068

Astropy Collaboration, Price-Whelan, A. M., Sipőcz, B. M., et al. 2018, AJ, 156, 123, doi: 10.3847/1538-3881/aabc4f

Astropy Collaboration, Price-Whelan, A. M., Lim, P. L., et al. 2022, ApJ, 935, 167, doi: 10.3847/1538-4357/ac7c74

Attridge, J. M., Roberts, D. H., & Wardle, J. F. C. 1999, ApJL, 518, L87, doi: 10.1086/312078

Atwood, W. B., Abdo, A. A., Ackermann, M., et al. 2009, ApJ, 697, 1071, doi: 10.1088/0004-637X/697/2/1071

Bañados, E., Carilli, C., Walter, F., et al. 2018a, ApJL, 861, L14, doi: 10.3847/2041-8213/aac511

Bañados, E., Venemans, B. P., Morganson, E., et al. 2014, AJ, 148, 14, doi: 10.1088/0004-6256/148/1/14

—. 2015, ApJ, 804, 118, doi: 10.1088/0004-637X/804/2/118

Bañados, E., Venemans, B. P., Decarli, R., et al. 2016, ApJS, 227, 11, doi: 10.3847/0067-0049/227/1/11

Bañados, E., Venemans, B. P., Mazzucchelli, C., et al. 2018b, Nature, 553, 473, doi: 10.1038/nature25180

Bañados, E., Mazzucchelli, C., Momjian, E., et al. 2021, ApJ, 909, 80, doi: 10.3847/1538-4357/abe239

Bañados, E., Schindler, J.-T., Venemans, B. P., et al. 2023, ApJS, 265, 29, doi: 10.3847/1538-4365/acb3c7

Babić, A., Miller, L., Jarvis, M. J., et al. 2007, A&A, 474, 755, doi: 10.1051/0004-6361:20078286

Banados, E., Khusanova, Y., Decarli, R., et al. 2024a, arXiv e-prints, arXiv:2408.12299, doi: 10.48550/arXiv.2408.12299

Banados, E., Momjian, E., Connor, T., et al. 2024b, arXiv e-prints, arXiv:2407.07236, doi: 10.48550/arXiv.2407.07236

Bauer, F. E., Condon, J. J., Thuan, T. X., & Broderick, J. J. 2000, ApJS, 129, 547, doi: 10.1086/313425

Becker, R. H., White, R. L., & Helfand, D. J. 1994, in Astronomical Society of the Pacific Conference Series, Vol. 61, Astronomical Data Analysis Software and Systems III, ed. D. R. Crabtree, R. J. Hanisch, & J. Barnes, 165

Becker, R. H., White, R. L., & Helfand, D. J. 1995, ApJ, 450, 559, doi: 10.1086/176166

Best, P. N., & Heckman, T. M. 2012, MNRAS, 421, 1569, doi: 10.1111/j.1365-2966.2012.20414.x

Bischetti, M., Feruglio, C., D'Odorico, V., et al. 2022, Nature, 605, 244, doi: 10.1038/s41586-022-04608-1

Bischetti, M., Fiore, F., Feruglio, C., et al. 2023, ApJ, 952, 44, doi: 10.3847/1538-4357/accea4

Blandford, R., Meier, D., & Readhead, A. 2019, ARA&A, 57, 467, doi: 10.1146/annurev-astro-081817-051948

Blandford, R. D., & Königl, A. 1979, ApJ, 232, 34, doi: 10.1086/157262

Bochanski, J. J., Hawley, S. L., Covey, K. R., et al. 2010, AJ, 139, 2679, doi: 10.1088/0004-6256/139/6/2679

Bromm, V., & Larson, R. B. 2004, ARA&A, 42, 79, doi: 10.1146/annurev.astro.42.053102.134034

Bromm, V., & Loeb, A. 2003, Nature, 425, 812, doi: 10.1038/nature02071

Brown, T. B., Mann, B., Ryder, N., et al. 2020, arXiv e-prints, arXiv:2005.14165, doi: 10.48550/arXiv.2005.14165

Buendia-Rios, T. M., Negrete, C. A., Marziani, P., & Dultzin, D. 2023, A&A, 669, A135, doi: 10.1051/0004-6361/202244177

Burningham, B., Hardcastle, M., Nichols, J. D., et al. 2016, MNRAS, 463, 2202, doi: 10.1093/mnras/stw2065

Buschkamp, P., Seifert, W., Polsterer, K., et al. 2012, in Society of Photo-Optical Instrumentation Engineers (SPIE) Conference Series, Vol. 8446, Ground-based and Airborne Instrumentation for Astronomy IV, ed. I. S. McLean, S. K. Ramsay, & H. Takami, 84465L, doi: 10.1117/12.926989

Capetti, A., Balmaverde, B., Tadhunter, C., et al. 2022, A&A, 657, A114, doi: 10.1051/0004-6361/202141965

Carilli, C. L., Gnedin, N. Y., & Owen, F. 2002, ApJ, 577, 22, doi: 10.1086/342179

Carnall, A. C. 2017, arXiv e-prints, arXiv:1705.05165, doi: 10.48550/arXiv.1705.05165

Casali, M., Adamson, A., Alves de Oliveira, C., et al. 2007, A&A, 467, 777, doi: 10.1051/0004-6361:20066514

Cavallotti, F., Wolter, A., Stocke, J. T., & Rector, T. 2004, A&A, 419, 459, doi: 10.1051/0004-6361:20034320

Chon, S., Hosokawa, T., & Yoshida, N. 2018, MNRAS, 475, 4104, doi: 10.1093/mnras/sty086

Ciardi, B., Inoue, S., Mack, K., Xu, Y., & Bernardi, G. 2015, in Advancing Astrophysics with the Square Kilometre Array (AASKA14), 6, doi: 10.22323/1.215.0006

Ciardi, B., Labropoulos, P., Maselli, A., et al. 2013, MNRAS, 428, 1755, doi: 10.1093/mnras/sts156

Coatman, L., Hewett, P. C., Banerji, M., et al. 2017, MNRAS, 465, 2120, doi: 10.1093/mnras/stw2797

Condon, J. J., Cotton, W. D., Greisen, E. W., et al. 1998, AJ, 115, 1693, doi: 10.1086/300337

Couchman, H. M. P., & Rees, M. J. 1986, MNRAS, 221, 53, doi: 10.1093/mnras/221.1.53

Curtis, H. D. 1918, Publications of Lick Observatory, 13, 9

D'Abrusco, R., Massaro, F., Ajello, M., et al. 2012, ApJ, 748, 68, doi: 10.1088/0004-637X/748/1/68

D'Abrusco, R., Massaro, F., Paggi, A., et al. 2014, ApJS, 215, 14, doi: 10.1088/0067-0049/215/1/14

D'Abrusco, R., Álvarez Crespo, N., Massaro, F., et al. 2019, ApJS, 242, 4, doi: 10.3847/1538-4365/ab16f4

Dalla Bontà, E., Peterson, B. M., Bentz, M. C., et al. 2020, ApJ, 903, 112, doi: 10.3847/1538-4357/abbc1c

de Menezes, R., Peña-Herazo, H. A., Marchesini, E. J., et al. 2019, A&A, 630, A55, doi: 10.1051/0004-6361/201936195

De Rosa, G., Venemans, B. P., Decarli, R., et al. 2014, ApJ, 790, 145, doi: 10.1088/0004-637X/790/2/145

Decarli, R., Walter, F., Venemans, B. P., et al. 2018, ApJ, 854, 97, doi: 10.3847/1538-4357/aaa5aa

Dewdney, P. E., Hall, P. J., Schilizzi, R. T., & Lazio, T. J. L. W. 2009, IEEE Proceedings, 97, 1482, doi: 10.1109/JPROC.2009.2021005

Dhillon, V. S., Marsh, T. R., Stevenson, M. J., et al. 2007, MNRAS, 378, 825, doi: 10.1111/j.1365-2966.2007.11881.x

Duncan, K. J., Windhorst, R. A., Koekemoer, A. M., et al. 2023, MNRAS, 522, 4548, doi: 10.1093/mnras/stad1267

Duras, F., Bongiorno, A., Ricci, F., et al. 2020, A&A, 636, A73, doi: 10.1051/0004-6361/201936817

Eddington, A. S. 1926, The Internal Constitution of the Stars

Edge, A., Sutherland, W., Kuijken, K., et al. 2013, The Messenger, 154, 32

Elias, J. H., Vukobratovich, D., Andrew, J. R., et al. 1998, in Society of Photo-Optical Instrumentation Engineers (SPIE) Conference Series, Vol. 3354, Infrared Astronomical Instrumentation, ed. A. M. Fowler, 555–565, doi: 10.1117/12.317281

Euclid Collaboration, Barnett, R., Warren, S. J., et al. 2019, A&A, 631, A85, doi: 10.1051/0004-6361/201936427

Euclid Collaboration, Scaramella, R., Amiaux, J., et al. 2022, A&A, 662, A112, doi: 10.1051/0004-6361/202141938

Euclid Collaboration, Mellier, Y., Abdurro'uf, et al. 2024, arXiv e-prints, arXiv:2405.13491, doi: 10.48550/arXiv.2405.13491

Event Horizon Telescope Collaboration, Akiyama, K., Alberdi, A., et al. 2019, ApJL, 875, L1, doi: 10.3847/2041-8213/ab0ec7

Event Horizon Telescope Collaboration, Akiyama, K., Algaba, J. C., et al. 2021, ApJL, 910, L13, doi: 10.3847/2041-8213/abe4de

Ewall-Wice, A., Dillon, J. S., Mesinger, A., & Hewitt, J. 2014, MNRAS, 441, 2476, doi: 10.1093/mnras/stu666

Fabian, A. C. 2012, ARA&A, 50, 455, doi: 10.1146/annurev-astro-081811-125521

Fan, X., Bañados, E., & Simcoe, R. A. 2023, ARA&A, 61, 373, doi: 10.1146/annurev-astro-052920-102455

Fan, X., Strauss, M. A., Becker, R. H., et al. 2006, AJ, 132, 117, doi: 10.1086/504836

Flesch, E. W. 2021, arXiv e-prints, arXiv:2105.12985, doi: 10.48550/arXiv.2105.12985

Furlanetto, S. R., & Loeb, A. 2002, ApJ, 579, 1, doi: 10.1086/342757

Furlanetto, S. R., Oh, S. P., & Briggs, F. H. 2006, PhR, 433, 181, doi: 10.1016/j.physrep.2006.08.002

Gammie, C. F., McKinney, J. C., & Tóth, G. 2003, ApJ, 589, 444, doi: 10.1086/374594

Gaspari, M., Ruszkowski, M., & Oh, S. P. 2013, MNRAS, 432, 3401, doi: 10.1093/mnras/stt692

Giersz, M., Leigh, N., Hypki, A., Lützgendorf, N., & Askar, A. 2015, MNRAS, 454, 3150, doi: 10.1093/mnras/stv2162

Ginsburg, A., Sipőcz, B. M., Brasseur, C. E., et al. 2019, AJ, 157, 98, doi: 10.3847/1538-3881/aafc33

Ginzburg, V. L., & Syrovatskii, S. I. 1969, ARA&A, 7, 375, doi: 10.1146/annurev.aa.07.090169.002111

Gloudemans, A. J., Duncan, K. J., Röttgering, H. J. A., et al. 2021, A&A, 656, A137, doi: 10.1051/0004-6361/202141722

Gordon, Y. A., Boyce, M. M., O'Dea, C. P., et al. 2021, arXiv e-prints, arXiv:2102.11753. https://arxiv.org/abs/2102.11753

Gordon, Y. A., Rudnick, L., Andernach, H., et al. 2023, ApJS, 267, 37, doi: 10.3847/1538-4365/acda30

Graham, A. W., & Driver, S. P. 2007, ApJ, 655, 77, doi: 10.1086/509758

Greene, J. E., & Ho, L. C. 2005, ApJ, 630, 122, doi: 10.1086/431897

Gürkan, G., Hardcastle, M. J., Best, P. N., et al. 2019, A&A, 622, A11, doi: 10.1051/0004-6361/201833892

Häberle, M., Neumayer, N., Seth, A., et al. 2024, Nature, 631, 285, doi: 10.1038/s41586-024-07511-z

Habouzit, M., Volonteri, M., Latif, M., Dubois, Y., & Peirani, S. 2016, MNRAS, 463, 529, doi: 10.1093/mnras/stw1924

Habouzit, M., Onoue, M., Bañados, E., et al. 2022, MNRAS, 511, 3751, doi: 10.1093/mnras/stac225

Hale, C. L., McConnell, D., Thomson, A. J. M., et al. 2021, PASA, 38, e058, doi: 10.1017/pasa.2021.47

Häring, N., & Rix, H.-W. 2004, ApJL, 604, L89, doi: 10.1086/383567

Harris, C. R., Millman, K. J., van der Walt, S. J., et al. 2020, Nature, 585, 357, doi: 10.1038/s41586-020-2649-2

Harrison, C. M., Costa, T., Tadhunter, C. N., et al. 2018, Nature Astronomy, 2, 198, doi: 10.1038/s41550-018-0403-6

Hartman, R. C., Bertsch, D. L., Bloom, S. D., et al. 1999, ApJS, 123, 79, doi: 10.1086/313231

He, Z., Wang, T., Liu, G., et al. 2019, Nature Astronomy, 3, 265, doi: 10.1038/s41550-018-0669-8

Hirano, S., Hosokawa, T., Yoshida, N., et al. 2014, ApJ, 781, 60, doi: 10.1088/0004-637X/781/2/60

Ho, L. C. 2002, ApJ, 564, 120, doi: 10.1086/324399

—. 2008, ARA&A, 46, 475, doi: 10.1146/annurev.astro.45.051806.110546

Hovatta, T., Valtaoja, E., Tornikoski, M., & Lähteenmäki, A. 2009, A&A, 494, 527, doi: 10.1051/0004-6361:200811150

Hunter, J. D. 2007, Computing in Science and Engineering, 9, 90, doi: 10.1109/MCSE.2007.55

Ighina, L., Belladitta, S., Caccianiga, A., et al. 2021, A&A, 647, L11, doi: 10.1051/0004-6361/202140362

Ighina, L., Caccianiga, A., Moretti, A., et al. 2024, arXiv e-prints, arXiv:2407.04094, doi: 10.48550/arXiv.2407.04094

Inayoshi, K., Visbal, E., & Haiman, Z. 2020, ARA&A, 58, 27, doi: 10.1146/annurev-astro-120419-014455

Intema, H. T., Jagannathan, P., Mooley, K. P., & Frail, D. A. 2017, A&A, 598, A78, doi: 10.1051/0004-6361/201628536

Ivezić, Ž., Menou, K., Knapp, G. R., et al. 2002, AJ, 124, 2364, doi: 10.1086/344069

Jarvis, M., Seymour, N., Afonso, J., et al. 2015, in Advancing Astrophysics with the Square Kilometre Array (AASKA14), 68, doi: 10.22323/1.215.0068

Jiang, Y.-F., Stone, J. M., & Davis, S. W. 2019, ApJ, 880, 67, doi: 10.3847/1538-4357/ab29ff

Jolley, E. J. D., & Kuncic, Z. 2008, MNRAS, 386, 989, doi: 10.1111/j.1365-2966.2008.13082.x

Jones, T. W., O'Dell, S. L., & Stein, W. A. 1974, ApJ, 188, 353, doi: 10.1086/152724

Joye, W. A., & Mandel, E. 2003, in Astronomical Society of the Pacific Conference Series, Vol. 295, Astronomical Data Analysis Software and Systems XII, ed. H. E. Payne, R. I. Jedrzejewski, & R. N. Hook, 489

Kadota, K., Sekiguchi, T., & Tashiro, H. 2021, PhRvD, 103, 023521, doi: 10.1103/PhysRevD.103.023521

Kaspi, S., Brandt, W. N., Maoz, D., et al. 2007, ApJ, 659, 997, doi: 10.1086/512094

Kaspi, S., Smith, P. S., Netzer, H., et al. 2000, ApJ, 533, 631, doi: 10.1086/308704

Keller, P. M., Thyagarajan, N., Kumar, A., Kanekar, N., & Bernardi, G. 2024, MNRAS, 528, 5692, doi: 10.1093/mnras/stae418

Kellermann, K. I., Sramek, R., Schmidt, M., Shaffer, D. B., & Green, R. 1989, AJ, 98, 1195, doi: 10.1086/115207

Kharb, P., Lister, M. L., & Cooper, N. J. 2010, ApJ, 710, 764, doi: 10.1088/0004-637X/710/1/764

Kirkby, D., Robitaille, T., Weaver, B. A., et al. 2024, desihub/speclite: Bug fix release: General clean-up prior to refactoring package infrastructure, v0.20, Zenodo, doi: 10.5281/zenodo.13225530

Kluyver, T., Ragan-Kelley, B., Pérez, F., et al. 2016, in Positioning and Power in Academic Publishing: Players, Agents and Agendas, ed. F. Loizides & B. Schmidt, IOS Press, 87 – 90

Kollgaard, R. I., Wardle, J. F. C., Roberts, D. H., & Gabuzda, D. C. 1992, AJ, 104, 1687, doi: 10.1086/116352

Kollmeier, J. A., Onken, C. A., Kochanek, C. S., et al. 2006, ApJ, 648, 128, doi: 10.1086/505646

Koopmans, L., Pritchard, J., Mellema, G., et al. 2015, in Advancing Astrophysics with the Square Kilometre Array (AASKA14), 1, doi: 10.22323/1.215.0001

Kormendy, J., & Ho, L. C. 2013, ARA&A, 51, 511, doi: 10.1146/annurev-astro-082708-101811

Kovalev, Y. Y., Lister, M. L., Homan, D. C., & Kellermann, K. I. 2007, ApJL, 668, L27, doi: 10.1086/522603

Kuncic, Z., & Bicknell, G. V. 2004, ApJ, 616, 669, doi: 10.1086/425032

—. 2007a, Ap&SS, 311, 127, doi: 10.1007/s10509-007-9522-8

—. 2007b, Modern Physics Letters A, 22, 1685, doi: 10.1142/S0217732307024243

Lacy, M., Baum, S. A., Chandler, C. J., et al. 2020, PASP, 132, 035001, doi: 10.1088/1538-3873/ab63eb

Lacy, M., Myers, S. T., Chandler, C., et al. 2022, VLASS Project Memo 13: Pilot and Quick Look Data Release (v2). https://library.nrao.edu/public/memos/vla/vlass/VLASS_017.pdf

Laor, A. 2000, ApJL, 543, L111, doi: 10.1086/317280

Latif, M. A., Schleicher, D. R. G., Schmidt, W., & Niemeyer, J. 2013, MNRAS, 433, 1607, doi: 10.1093/mnras/stt834

Li, J., Wang, R., Pensabene, A., et al. 2024, ApJ, 962, 119, doi: 10.3847/1538-4357/ad1754

Lister, M. L., Aller, M. F., Aller, H. D., et al. 2018, ApJS, 234, 12, doi: 10.3847/1538-4365/aa9c44

Lister, M. L., Homan, D. C., Kellermann, K. I., et al. 2021, ApJ, 923, 30, doi: 10.3847/1538-4357/ac230f

Lister, M. L., Homan, D. C., Hovatta, T., et al. 2019, ApJ, 874, 43, doi: 10.3847/1538-4357/ab08ee

Lupi, A., Colpi, M., Devecchi, B., Galanti, G., & Volonteri, M. 2014, MNRAS, 442, 3616, doi: 10.1093/mnras/stu1120

Mack, K. J., & Wyithe, J. S. B. 2012, MNRAS, 425, 2988, doi: 10.1111/j.1365-2966.2012.21561.x

Madau, P., Meiksin, A., & Rees, M. J. 1997, ApJ, 475, 429, doi: 10.1086/303549

Madau, P., & Rees, M. J. 2001, ApJL, 551, L27, doi: 10.1086/319848

Magorrian, J., Tremaine, S., Richstone, D., et al. 1998, AJ, 115, 2285, doi: 10.1086/300353

Mapelli, M. 2016, MNRAS, 459, 3432, doi: 10.1093/mnras/stw869

Maraschi, L., Ghisellini, G., & Celotti, A. 1992, ApJL, 397, L5, doi: 10.1086/186531

Martínez-Aldama, M. L., del Olmo, A., Marziani, P., et al. 2018, A&A, 618, A179, doi: 10.1051/0004-6361/201833541

Marziani, P., del Olmo, A., Martínez-Aldama, M. L., et al. 2017, Atoms, 5, 33, doi: 10.3390/atoms5030033

Massaro, E., Giommi, P., Leto, C., et al. 2009, A&A, 495, 691, doi: 10.1051/0004-6361:200810161

Massaro, E., Maselli, A., Leto, C., et al. 2015, Ap&SS, 357, 75, doi: 10.1007/s10509-015-2254-2

Mattox, J. R., Wagner, S. J., Malkan, M., et al. 1997, ApJ, 476, 692, doi: 10.1086/303639

Mauch, T., Murphy, T., Buttery, H. J., et al. 2003, MNRAS, 342, 1117, doi: 10.1046/j.1365-8711.2003.06605.x

—. 2008, VizieR Online Data Catalog, VIII/81A

Mazzucchelli, C., Bischetti, M., D'Odorico, V., et al. 2023, A&A, 676, A71, doi: 10.1051/0004-6361/202346317

McKinney, J. C. 2006, MNRAS, 368, 1561, doi: 10.1111/j.1365-2966.2006.10256.x

McKinney, W. 2010, in Proceedings of the 9th Python in Science Conference, ed. Stéfan van der Walt & Jarrod Millman, 56 – 61, doi: 10.25080/Majora-92bf1922-00a

McLure, R. J., & Jarvis, M. J. 2004, MNRAS, 353, L45, doi: 10.1111/j.1365-2966.2004.08305.x

McMullin, J. P., Waters, B., Schiebel, D., Young, W., & Golap, K. 2007, in Astronomical Society of the Pacific Conference Series, Vol. 376, Astronomical Data Analysis Software and Systems XVI, ed. R. A. Shaw, F. Hill, & D. J. Bell, 127

Momjian, E., Carilli, C. L., Bañados, E., Walter, F., & Venemans, B. P. 2018, ApJ, 861, 86, doi: 10.3847/1538-4357/aac76f

Momjian, E., Carilli, C. L., & McGreer, I. D. 2008, AJ, 136, 344, doi: 10.1088/0004-6256/136/1/344

Morabito, L. K., Jackson, N. J., Mooney, S., et al. 2022, A&A, 658, A1, doi: 10.1051/0004-6361/202140649

Morganson, E., De Rosa, G., Decarli, R., et al. 2012, AJ, 143, 142, doi: 10.1088/0004-6256/143/6/142

Motch, C., Guillout, P., Haberl, F., et al. 1998, A&AS, 132, 341, doi: 10.1051/aas:1998299

Murphy, T., Sadler, E. M., Ekers, R. D., et al. 2010, MNRAS, 402, 2403, doi: 10.1111/j.1365-2966.2009.15961.x

Neeleman, M., Novak, M., Venemans, B. P., et al. 2021, ApJ, 911, 141, doi: 10.3847/1538-4357/abe70f

Nyland, K., Harwood, J. J., Mukherjee, D., et al. 2018, ApJ, 859, 23, doi: 10.3847/1538-4357/aab3d1

Oei, M. S. S. L., van Weeren, R. J., Hardcastle, M. J., et al. 2022, A&A, 660, A2, doi: 10.1051/0004-6361/202142778

Omukai, K., & Palla, F. 2001, ApJL, 561, L55, doi: 10.1086/324410

Onoue, M., Bañados, E., Mazzucchelli, C., et al. 2020, ApJ, 898, 105, doi: 10.3847/1538-4357/aba193

Pacucci, F., Volonteri, M., & Ferrara, A. 2015, MNRAS, 452, 1922, doi: 10.1093/mnras/stv1465

Padovani, P. 1993, MNRAS, 263, 461, doi: 10.1093/mnras/263.2.461

Park, J., & Algaba, J. C. 2022, Galaxies, 10, 102, doi: 10.3390/galaxies10050102

Perez, F., & Granger, B. E. 2007, Computing in Science and Engineering, 9, 21, doi: 10.1109/MCSE.2007.53

Peterson, B. M. 2014, SSRv, 183, 253, doi: 10.1007/s11214-013-9987-4

Peterson, B. M., Ferrarese, L., Gilbert, K. M., et al. 2004, ApJ, 613, 682, doi: 10.1086/423269

Pezzulli, E., Valiante, R., & Schneider, R. 2016, MNRAS, 458, 3047, doi: 10.1093/mnras/stw505

Piner, B. G., Pant, N., & Edwards, P. G. 2010, ApJ, 723, 1150, doi: 10.1088/0004-637X/723/2/1150

Piranomonte, S., Perri, M., Giommi, P., Landt, H., & Padovani, P. 2007, A&A, 470, 787, doi: 10.1051/0004-6361:20077086

Portegies Zwart, S. F., Baumgardt, H., Hut, P., Makino, J., & McMillan, S. L. W. 2004, Nature, 428, 724, doi: 10.1038/nature02448

Potter, W. J., & Cotter, G. 2012, MNRAS, 423, 756, doi: 10.1111/j.1365-2966.2012.20918.x

Prochaska, J., Hennawi, J., Westfall, K., et al. 2020, The Journal of Open Source Software, 5, 2308, doi: 10.21105/joss.02308

Pushkarev, A. B., Kovalev, Y. Y., Lister, M. L., et al. 2017, Galaxies, 5, 93, doi: 10.3390/galaxies5040093

Raiteri, C. M., Villata, M., Larionov, V. M., et al. 2021, MNRAS, 504, 5629, doi: 10.1093/mnras/stab1268

Reback, J., jbrockmendel, McKinney, W., et al. 2022, pandas-dev/pandas: Pandas 1.4.2, v1.4.2, Zenodo, Zenodo, doi: 10.5281/zenodo.3509134

Regan, J. A., Wise, J. H., Woods, T. E., et al. 2020, The Open Journal of Astrophysics, 3, 15, doi: 10.21105/astro.2008.08090

Richards, G. T., Lacy, M., Storrie-Lombardi, L. J., et al. 2006, ApJS, 166, 470, doi: 10.1086/506525

Robitaille, T., & Bressert, E. 2012, APLpy: Astronomical Plotting Library in Python, Astrophysics Source Code Library, record ascl:1208.017. http://ascl.net/1208.017

Rojas-Ruiz, S., Bañados, E., Neeleman, M., et al. 2021, ApJ, 920, 150, doi: 10.3847/1538-4357/ac1a13

Ross, N. P., & Cross, N. J. G. 2020, MNRAS, 494, 789, doi: 10.1093/mnras/staa544

Runnoe, J. C., Brotherton, M. S., & Shang, Z. 2012, MNRAS, 422, 478, doi: 10.1111/j.1365-2966.2012.20620.x

Rupke, D. S. N., & Veilleux, S. 2011, ApJL, 729, L27, doi: 10.1088/2041-8205/729/2/L27

Rybicki, G. B., & Lightman, A. P. 1979, Radiative processes in astrophysics (Wiley)

Sadowski, A., & Narayan, R. 2016, MNRAS, 456, 3929, doi: 10.1093/mnras/stv2941

Saikia, P., Körding, E., & Falcke, H. 2016, MNRAS, 461, 297, doi: 10.1093/mnras/stw1321

Salviander, S., & Shields, G. A. 2013, ApJ, 764, 80, doi: 10.1088/0004-637X/764/1/80

Sambruna, R. M., Maraschi, L., & Urry, C. M. 1996, ApJ, 463, 444, doi: 10.1086/177260

Savolainen, T., Homan, D. C., Hovatta, T., et al. 2010, A&A, 512, A24, doi: 10.1051/0004-6361/200913740

Sbarrato, T., Ghisellini, G., Giovannini, G., & Giroletti, M. 2021, A&A, 655, A95, doi: 10.1051/0004-6361/202141827

Schindler, J.-T. 2022, Sculptor: Interactive modeling of astronomical spectra. http://ascl.net/2202.018

Schindler, J.-T., Farina, E. P., Bañados, E., et al. 2020, ApJ, 905, 51, doi: 10.3847/1538-4357/abc2d7

Semelin, B. 2016, MNRAS, 455, 962, doi: 10.1093/mnras/stv2312

Shankar, F., Weinberg, D. H., & Miralda-Escudé, J. 2009, ApJ, 690, 20, doi: 10.1088/0004-637X/690/1/20

Shaw, M. S., Romani, R. W., Cotter, G., et al. 2012, ApJ, 748, 49, doi: 10.1088/0004-637X/748/1/49

Shen, Y., & Liu, X. 2012, ApJ, 753, 125, doi: 10.1088/0004-637X/753/2/125

Shen, Y., Richards, G. T., Strauss, M. A., et al. 2011, ApJS, 194, 45, doi: 10.1088/0067-0049/194/2/45

Shen, Y., Greene, J. E., Ho, L. C., et al. 2015, ApJ, 805, 96, doi: 10.1088/0004-637X/805/2/96

Shi, Y., Kremer, K., & Hopkins, P. F. 2024, ApJL, 969, L31, doi: 10.3847/2041-8213/ad5a95

Shimabukuro, H., Ichiki, K., Inoue, S., & Yokoyama, S. 2014, PhRvD, 90, 083003, doi: 10.1103/PhysRevD.90.083003

Shimwell, T. W., Hardcastle, M. J., Tasse, C., et al. 2022, A&A, 659, A1, doi: 10.1051/0004-6361/202142484

Sikora, M., Begelman, M. C., & Rees, M. J. 1994, ApJ, 421, 153, doi: 10.1086/173633

Sikora, M., Stawarz, Λ., $\&Lasota, J. - P. 2007, ApJ, 658, 815, doi:$

Simcoe, R. A., Burgasser, A. J., Schechter, P. L., et al. 2013, PASP, 125, 270, 10.1086/670241

Stickel, M., Padovani, P., Urry, C. M., Fried, J. W., & Kuehr, H. 1991, ApJ, 374, 431, 10.1086/170133

Sutherland, W., Emerson, J., Dalton, G., et al. 2015, A&A, 575, A25, 10.1051/0004-6361/201424973

Takeo, E., Inayoshi, K., & Mineshige, S. 2020, MNRAS, 497, 302, 10.1093/mnras/staa1906

Tavecchio, F., Maraschi, L., Sambruna, R. M., & Urry, C. M. 2000, ApJL, 544, L23, 10.1086/317292

Taylor, M. B. 2005, in Astronomical Society of the Pacific Conference Series, Vol. 347, Astronomical Data Analysis Software and Systems XIV, ed. P. Shopbell, M. Britton, & R. Ebert, 29

Tchekhovskoy, A., Narayan, R., & McKinney, J. C. 2010, ApJ, 711, 50, 10.1088/0004-637X/711/1/50

Tody, D. 1986, in Society of Photo-Optical Instrumentation Engineers (SPIE) Conference Series, Vol. 627, Instrumentation in astronomy VI, ed. D. L. Crawford, 733, 10.1117/12.968154

Tsuzuki, Y., Kawara, K., Yoshii, Y., et al. 2006, ApJ, 650, 57, 10.1086/506376

Urry, C. M., & Padovani, P. 1995, PASP, 107, 803, 10.1086/133630

van der Walt, S., Colbert, S. C., & Varoquaux, G. 2011, Computing in Science and Engineering, 13, 22, 10.1109/MCSE.2011.37

Van Rossum, G., & Drake, F. L. 2009, Python 3 Reference Manual (Scotts Valley, CA: CreateSpace)

Venemans, B. P., Walter, F., Zschaechner, L., et al. 2016, ApJ, 816, 37, 10.3847/0004-637X/816/1/37

Venemans, B. P., Walter, F., Neeleman, M., et al. 2020, ApJ, 904, 130, 10.3847/1538-4357/abc563

Vernet, J., Dekker, H., D'Odorico, S., et al. 2011, A&A, 536, A105, 10.1051/0004-6361/201117752

Vestergaard, M., & Peterson, B. M. 2006, ApJ, 641, 689, 10.1086/500572

Vestergaard, M., & Wilkes, B. J. 2001, ApJS, 134, 1, 10.1086/320357

Virtanen, P., Gommers, R., Oliphant, T. E., et al. 2020, Nature Methods, 17, 261, 10.1038/s41592-019-0686-2

Volonteri, M., & Bellovary, J. 2012, Reports on Progress in Physics, 75, 124901, 10.1088/0034-4885/75/12/124901

Volonteri, M., Silk, J., & Dubus, G. 2015, ApJ, 804, 148, 10.1088/0004-637X/804/2/148

Wagenveld, J. D., Saxena, A., Duncan, K. J., Röttgering, H. J. A., & Zhang, M. 2022, A&A, 660, A22, 10.1051/0004-6361/202142445

Wagner, S. J., Witzel, A., Heidt, J., et al. 1996, AJ, 111, 2187, 10.1086/117954

Waskom, M. L. 2021, Journal of Open Source Software, 6, 3021, 10.21105/joss.03021

Wenger, M., Ochsenbein, F., Egret, D., et al. 2000, A&AS, 143, 9, 10.1051/aas:2000332

Wilkinson, P. N., Readhead, A. C. S., Purcell, G. H., & Anderson, B. 1977, Nature, 269, 764, 10.1038/269764a0

Wilson, A. S., & Colbert, E. J. M. 1995, ApJ, 438, 62, 10.1086/175054

Wilson, J. C., Henderson, C. P., Herter, T. L., et al. 2004, in Society of Photo-Optical Instrumentation Engineers (SPIE) Conference Series, Vol. 5492, Ground-based Instrumentation for Astronomy, ed. A. F. M. Moorwood & M. Iye, 1295–1305, 10.1117/12.550925

Woods, T. E., Agarwal, B., Bromm, V., et al. 2019, PASA, 36, e027, 10.1017/pasa.2019.14

Worrall, D. M. 2009, A&A Rv, 17, 1, 10.1007/s00159-008-0016-7

Wright, E. L., Eisenhardt, P. R. M., Mainzer, A. K., et al. 2010, AJ, 140, 1868, 10.1088/0004-6256/140/6/1868

Wu, Q., & Shen, Y. 2022, ApJS, 263, 42, 10.3847/1538-4365/ac9ead

Wu, X.-B., Wang, F., Fan, X., et al. 2015, Nature, 518, 512, 10.1038/nature14241

Xie, Z.-L., Bañados, E., Belladitta, S., et al. 2024, ApJ, 964, 98, 10.3847/1538-4357/ad20d3

Xu, Y., Yue, B., & Chen, X. 2021, ApJ, 923, 98, 10.3847/1538-4357/ac30da

Yang, H. Y. K., Ruszkowski, M., & Zweibel, E. G. 2022, Nature Astronomy, 6, 584, 10.1038/s41550-022-01618-x

Yang, J., Wang, F., Fan, X., et al. 2020, ApJL, 897, L14, 10.3847/2041-8213/ab9c26

—. 2021, ApJ, 923, 262, 10.3847/1538-4357/ac2b32

Yang, J., Fan, X., Gupta, A., et al. 2023, ApJS, 269, 27, 10.3847/1538-4365/acf99b

Yu, Q., & Tremaine, S. 2002, MNRAS, 335, 965, 10.1046/j.1365-8711.2002.05532.x